Understanding Interactions with Human Intestinal Tissue for Capsule Endoscopy

Xuan Wang

A thesis submitted in partial fulfilment of the requirements for the degree of

Doctor of Philosophy

The University of Sheffield

Faculty of Engineering

Department of mechanical engineering

Submission Date

Winter 2024

Acknowledgements

First and foremost, I would like to express my deepest gratitude to my supervisor, Prof. Matt Carré, for his invaluable guidance, mentorship, and encouragement throughout my doctoral journey. His unwavering support, insightful advice, and patience have been instrumental in shaping my research and enabling me to grow as a scholar. I feel privileged to have had him as my first supervisor, and I am profoundly thankful for the time and effort he dedicated to helping me succeed. I would also like to thank my second supervisor, Prof. Roger Lewis, for his support and constructive feedback during my PhD. His expertise and thoughtful input have greatly contributed to the progress of my research.

I would also like to extend my sincere thanks to all the members of the Sheffield and Leeds TrEnT teams, the Human and Interactions Group, and the Tribology Group. Your selfless sharing of suggestions and academic insights has been of great help to me.

To my parents, Mr. Dezhong Wang and Mrs. Chunlan Zhang, I extend my heartfelt appreciation for their unconditional love and support. Their belief in me has been my foundation, and their encouragement has sustained me through every challenge.

I am also grateful to my friends for their constant encouragement and companionship throughout this journey. Their presence made the experience of my doctoral studies enjoyable and memorable. The great times we shared will always hold a special place in my heart.

Finally, I would like to thank everyone who has contributed, in ways big or small, to this journey of mine. It has been an incredible experience, and I am deeply thankful for all the support I have received.

Abstract

This thesis investigates the mechanical and tribological interactions between capsule endoscopy devices and small intestinal tissues, aiming to inform the future design of capsules in order to address persistent challenges such as capsule retention, slippage, and uncontrolled movement. While capsule endoscopy provides a minimally invasive diagnostic alternative to traditional methods, its effectiveness is often hindered by unpredictable frictional behaviour and poor mobility within the gastrointestinal tract. To address these limitations, this study formulates the central research question: Can a novel experimental methodology that simulates the interaction between capsule endoscopy devices and the intestine provide new insights into the tribological behaviour of a sliding capsule, and the effect of different capsule design factors on friction, in order to inform future medical device development?

A multiphase experimental approach was employed, beginning with the mechanical characterization of porcine small intestine tissue under various strain rates. These results informed the development of an ex vivo friction testing platform that simulates capsule–tissue interactions under hydrated conditions. Friction experiments were performed using various lubricants, capsule orientations, loads, speeds, and surface designs.

The experimental studies revealed that (1) porcine tissue exhibits viscoelastic behaviour with rate-dependent stiffness; (2) mucus and PBS both reduce friction, but mucus does not outperform PBS under current conditions; (3) increased normal load reduces the coefficient of friction, likely due to interstitial fluid dynamics; (4) sliding speed correlates positively with friction and (5) ridge design significantly alters friction, with a 2:1 height-to-width ratio yielding the most stable resistance due to enhanced interlocking. These insights provide a foundational framework for future

advancements in capsule endoscopy by clarifying the mechanics of frictional interaction within the small intestine.

Contents

List of Figures

List of Tables

Declaration

I, the author, confirm that the Thesis is my own work. I am aware of the University's Guidance on the Use of Unfair Means (www.sheffield.ac.uk/ssid/unfair-means). This work has not previously been presented for an award at this, or any other, university.

Chapter 1

Introduction

1.1 Framework and motivation

Gastrointestinal (GI) diseases have become increasingly prevalent, posing a significant burden on patients worldwide [1]. While traditional endoscopy remains a reliable diagnostic tool, it is often invasive and uncomfortable. Capsule endoscopy offers a minimally invasive alternative, enabling a comprehensive examination of the GI tract through a small, self-contained device that is simply swallowed.

Capsule endoscopy (CE) has transformed gastrointestinal diagnostics by enabling non-invasive visualization of the small intestine without the need for sedation or complex instrumentation [2]. However, the unpredictable mechanical interactions between the capsule and intestinal tissues impact on navigation, frictional behaviour, and image stability. A major complication of CE is capsule retention, which can lead to small bowel obstruction and severe consequences [3, 4].

The retention rate of CE in healthy individuals is approximately 1.5% [5], but this risk increases in patients with conditions such as inflammatory bowel disease and Crohn's disease. A meta-analysis of 25 studies by Rezapour et al. reported an overall retention rate of 2.1% in patients undergoing CE for suspected small-bowel bleeding, rising to 3.6% in suspected IBD cases and 8.2% in confirmed IBD cases. Small-bowel strictures were the leading cause of retention, accounting for 54% of cases, with approximately 57% of retained capsules requiring surgical intervention [6]. Similarly, a review by Pasha et al. found a retention rate of 3.32% among patients with Crohn's disease [7]. In many instances, capsule retention is asymptomatic and requires additional imaging or surgical removal [5, 8, 9].

On the other hand, self-propelled capsule endoscopes are also in development that function as intelligent microsystems, capable of imaging, sampling, and even delivering medication to targeted regions within the gastrointestinal tract [10]. For optimal functionality, these devices require precise movement control and sufficient traction. Efficient propulsion must be achieved while minimizing slippage and preventing capsule retention. Additionally, the design of the capsule body plays a key role in overcoming frictional resistance while ensuring controlled movement, as excessive speed could compromise the quality of diagnostic data transmission and the inspection details and completeness.

Therefore, a comprehensive understanding of these interactions is crucial for optimizing capsule mobility, reducing retention risk, and improving both diagnostic accuracy and patient safety. The primary mechanical challenges stem from the complex and dynamic environment of the small intestine. The intestinal walls are composed of soft, viscoelastic tissues that deform under contact, leading to variable frictional resistance. Additionally, the presence of mucus, a key lubricating agent, alters the tribological properties of the system. The structural design of the capsule itself, including size, shape, and surface texture, further influences its motion through the intestine. These factors necessitate a systematic study of the frictional interactions between capsule robots and intestinal tissues to enhance performance and control.

1.2 Research problem and scope

Despite extensive research in capsule endoscopy, a comprehensive understanding of the tribological interactions between the capsule and the intestinal lumen remains elusive. Existing friction evaluation methodologies often rely on simplified models that fail to fully capture the biomechanical complexity of the intestinal environment, particularly the role of mucus and the soft tissues in the contact region. This study is committed to bridge these gaps by developing an ex vivo experimental platform and methodology to systematically investigate frictional behaviour under controlled conditions.

The central research question of this thesis is: Can a novel experimental methodology that simulates the interaction between capsule endoscopy devices and the intestine provide new insights into the tribological behaviour of a sliding capsule, and the

effect of different capsule design factors on friction, in order to inform future medical device development? To address this question, this study focuses on:

- Characterizing the mechanical properties of small intestine tissue under ex vivo conditions.
- Developing a robust experimental setup to simulate realistic interactions between capsules and tissues.
- Investigating the effects of mucus lubrication on frictional behaviour.
- Evaluating the impact of capsule design parameters (e.g., size, surface texture, and ridge structures) on frictional resistance.

1.3 Exclusions and limitations

This research is conducted using an ex-vivo approach, meaning that experiments are performed on excised animal tissue rather than in live subjects. While this allows for controlled and repeatable testing, it does not fully replicate the peristaltic motion and continuous mucus secretion present in vivo. Furthermore, the study does not include investigations on human intestinal tissues due to ethical and practical constraints. Instead, results from tests on ex-vivo porcine samples serve as a basis for future in vivo validation. Moreover, the relationship between the frictional results and their impact on diagnostic efficiency is not extensively explored in this study.

1.4 Selection of the tribo-system

The tribo-system selected for this research consists of a capsule robot interacting with intestinal tissue under lubricated conditions. A tribometer-based setup is used to measure frictional forces while mimicking physiological conditions as closely as possible. The choice of this system is justified based on the need for precise control over experimental variables, enabling systematic evaluation of how different parameters influence friction.

A schematic representation of the tribo-system is provided in Figure 1.1, illustrating the key components, including the capsule and its shell texture, intestinal tissue and its circular folds and mucus layer. This setup enables the controlled replication of frictional interactions encountered in the gastrointestinal tract.

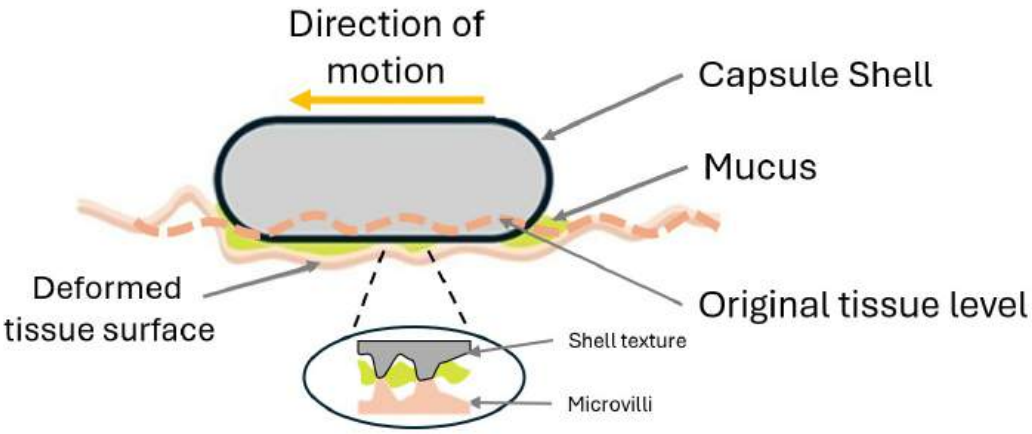

Figure 1.1: Schematic representation of the tribo-system used in this study.

1.5 Aim and objectives

The aim of this project is to simulate the interaction between capsule endoscopy devices and the intestinal environment, investigate the tribological behaviour of a sliding capsule, and the effect of different capsule design factors on friction, in order to inform future medical device development.

The objectives are as follows:

- Conduct a comprehensive literature review to trace the development of capsule endoscopy, identify factors influencing friction, analyse prototype designs, explore intestine-capsule interactions, and pinpoint research gaps.
- Conduct mechanical property tests to precisely characterize the viscoelastic and deformation properties of intestinal tissues, facilitating the selection of a comparable substrate for friction experiments.
- Develop and validate a synthetic intestinal testbed that closely replicates the mechanical properties and lubrication environment of the small intestine for friction interaction testing.
- Establish experimental methodologies using the synthetic testbed and carry out experiments to better understand the effects of intestinal mucus properties.
- Investigate capsule design and loading parameters (size, orientation, sliding speed, normal load, ridge designs and surface roughness) on frictional behaviour to inform future medical device development.

Chapter 2

Literature review

2.1 Background

2.1.1 Fundamentals of friction in soft solids

Friction is a fundamental mechanical phenomenon that resists the relative motion between two contacting surfaces. It plays a pivotal role in various applications, ranging from industrial machinery to biomedical devices. The classical framework of friction is based on Amontons' and Coulomb's laws, where the friction force is considered proportional to the normal load and independent of contact area or sliding velocity [11]. However, such simplifications are insufficient when dealing with soft solids, materials that undergo substantial elastic or viscoelastic deformation during contact.

2.1.1.1 Friction in soft solids

Soft solids such as elastomers, biological tissues, and hydrogels present a more complex frictional response due to their inherent compliance, surface adhesion, and time-dependent mechanical properties. Unlike rigid bodies, soft materials such as human skin, deform significantly at the interface, thereby altering the real contact area and modifying frictional forces [12]. In biological and synthetic soft interfaces, surface roughness, interfacial lubrication, adhesion, and bulk viscoelasticity all contribute simultaneously to the overall frictional behaviour [13].

Notably, the friction of soft materials is not constant; it depends on multiple parameters such as sliding velocity, temperature, normal pressure, and the presence of interfacial fluids. For instance, in biological systems, mucus and other fluid films act as lubricants, profoundly impacting frictional performance [14]. These effects are

often visualized using the Stribeck curve, which reveals how friction evolves across different lubrication regimes.

2.1.1.2 The Stribeck Curve

The classic Stribeck curve model characterizes the dynamic friction between two impermeable rigid surfaces with Newtonian lubricants, describing the transition among three lubrication regimes: boundary, mixed, and hydrodynamic, by plotting the coefficient of friction against a dimensionless parameter typically given by $\eta v/W$, where η is fluid viscosity, v is sliding speed, and W is normal load as shown in Figure 2.1 [15]. The curve typically exhibits three regimes:

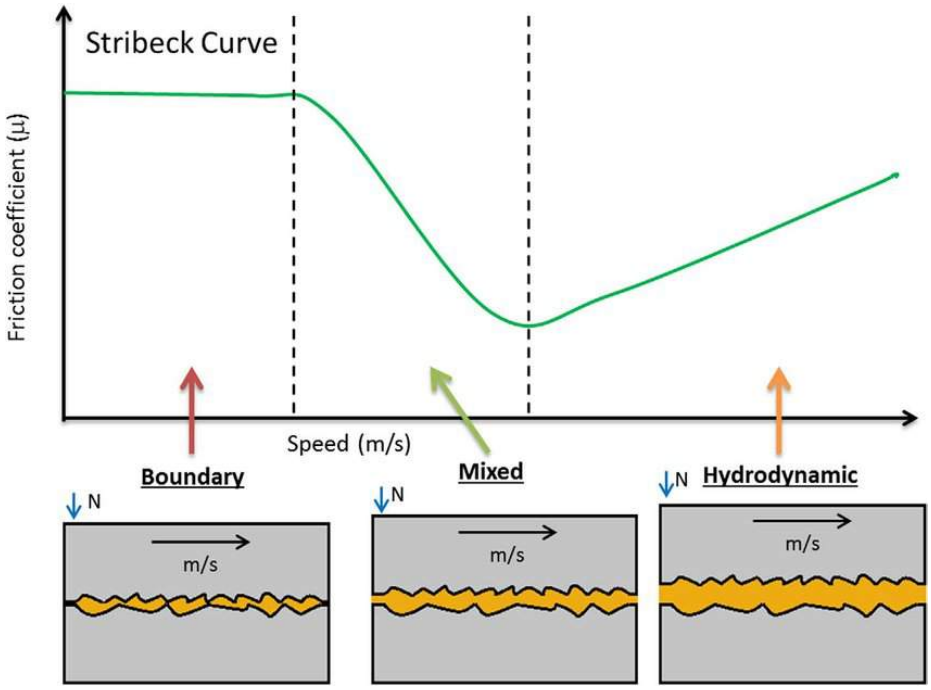

Figure 2.1: Depiction of the Stribeck curve showing the three lubrication regimes. From [16].

- **Boundary lubrication**: Surface asperities are in direct contact, leading to high friction. Adhesive and shear forces dominate this regime.
- **Mixed lubrication**: Partial fluid films separate some regions of the surface while others remain in contact, reducing friction significantly.
- **Hydrodynamic lubrication**: A continuous fluid film separates the two surfaces completely, resulting in minimal friction.

In soft material applications such as biomedical implants and robotic skin, the Stribeck curve provides crucial insights into how design and environmental factors influence sliding behaviour.

2.1.1.3 Friction models for soft materials

Various models have been proposed to capture the complex frictional behaviour of soft solids. These models range from adaptations of classical mechanics to fully viscoelastic or adhesion-based frameworks.

- **Adhesive Contact Models**: The Johnson-Kendall-Roberts (JKR) model applies to highly adhesive, compliant materials, where surface energy significantly enlarges the contact area under load [17]. In contrast, the Derjaguin-Muller-Toporov (DMT) model suits low-adhesion, stiffer contacts with smaller deformations [18]. Both models link friction to interfacial bonding and elastic deformation, providing a foundation for understanding how adhesion and contact mechanics govern soft-material friction.

- **Viscoelastic Hysteresis Models**: These models attribute friction primarily to energy dissipation within the bulk material rather than surface interactions. By treating the soft solid as a viscoelastic medium, they relate friction to the loss modulus and strain-rate effects. The Persson model, for instance, integrates surface roughness spectra with frequency-dependent material properties, predicting velocity-dependent friction due to cyclic deformation of asperities [19]. This approach is powerful for polymers and gels but requires detailed rheological and topographical data.

- **Soft Elasto-Hydrodynamic Lubrication (EHL)**: EHL theory describes lubricated soft contacts where elastic deformation and fluid dynamics interact. It predicts friction by coupling Reynolds' lubrication equation with elastic deformation equations, accounting for fluid pressure and film thickness [20]. This model is essential for biological systems and engineered hydrogels, where friction transitions from boundary to hydrodynamic regimes with increasing speed.

- **Modified Amontons–Coulomb Models**: These empirical models incorporate dependencies on velocity, contact area, and lubrication. For example, Van Kuilenburg et al. used modified friction models in skin-tissue studies [12]. Empirical corrections are introduced to adapt the traditional constant coefficient of

friction to velocity-sensitive cases, making them useful for preliminary analysis but limited in capturing time-dependent effects like viscoelasticity.

2.1.2 Application background

A global study revealed that over 40% of individuals experience functional gastrointestinal disorders, making them a widespread condition that significantly impacts patients' quality of life and places a considerable burden on healthcare systems [1]. If not controlled in the early stages, GI tract diseases such as bleeding, inflammation, or tumours can lead to cancer or other fatal diseases [21]. The invention of invasive wired endoscopy established the possibility of viewing the GI tract directly and effectively for diagnosis [22]. Nevertheless, this conventional push-type endoscope also has limitations, such as being a rigid (relatively high stiffness) instrument which could cause pain and discomfort to the patients, increasing the risk of causing perforation and cross-contamination [23]. Moreover, it could only detect part of the GI tract (the deepest reachable duodenum) but not the entire small intestine. Overcoming these issues led to the development of capsule endoscopy.

Table 2.1: Specifications of commercial capsule endoscope robots.

Capsule Type	Company	Size (mm)	Weight (g)	Locomotion	Frames per Second	No. of Cameras	Angle of View (°)	Drug Delivery	Battery Life (h)
PillCam SB	Medtronic	Ø11×26.0	NA	Passive	2	1	140	No	8
PillCam SB2	Medtronic	Ø11×26.0	NA	Passive	2	1	156	No	9
PillCam SB3	Medtronic	Ø11.4×26.2	3	Passive	2–6	2	156	No	11–12
PillCam Colon2	Medtronic	Ø11.6×32.3	2.9	Passive	4–35	2	344	No	10
PillCam UGI	Medtronic	Ø11.6×32.3	2.9	Passive	18–38	2	344	No	10
EndoCapsule 10	Olympus	Ø11×26	3.3	Passive	2	2	160	No	1.5
NaviCam	Ankon	Ø11.6×26.8	4.8	Active	2	1	151	No	12
OMOM-HD	Jinshan	Ø11×25.4	3	Passive	2–10	1	172	No	8
OMOM-RC22	Jinshan	Ø11.5×30	5	Active	2–10	1	172	No	12
CapsoCam Plus	CapsoVision	Ø11×31	4	Passive	12–20	4	360	No	15
MiroCam Navi	IntroMedic	10.8×24.5	4.2	Active	6	1	170	No	12
SMCE	JIFU Medical	Ø11×27	2.7	Active	4	1	136	No	8
IntelliCap	Medimetrics	Ø11×26.7	2.8	Active	NA	NA	NA	Yes	10
Enterion Capsule	Phillips	Ø11×32	2.8	Passive	NA	NA	NA	Yes	48

NA = Not Available

The concept of CE was first introduced by Israeli scientist Gavriel Iddan in the mid-1990s [21]. The invention of CE proved the possibility of wireless transmission of photos and observation for clinical use of the digestive tract. After that, various studies have been conducted for considering different locomotive methods, undertaking more medical tasks and other developments. Nowadays, CE robots such as PillCAM are available to examine the health condition of the oesophagus, stomach, small bowel

and colon and have become the first choice for the evaluation of the small bowel in children [24, 25]. Previous papers and official product websites regarding commercial CE systems were reviewed, with their specifications presented in Table 2.1. A meta-analysis was conducted by G. Blanco-Velasco et al. using data from 10 articles to evaluate diagnostic performance across various products [26]. However, due to limited evidence, the analysis concluded that no single CE system demonstrated clear superiority. The optimal choice should therefore be based on factors such as operator experience, cost, and availability. In addition to the advantages of non-invasive, painless, no cross-infection risk and without the need for sedation [2, 23], the diagnostic results were proved reliable compared with the conventional endoscopy for the upper GI tract. The diagnostic accuracy, sensitivity and specificity of CE for detecting the region part exceed 90% [27].

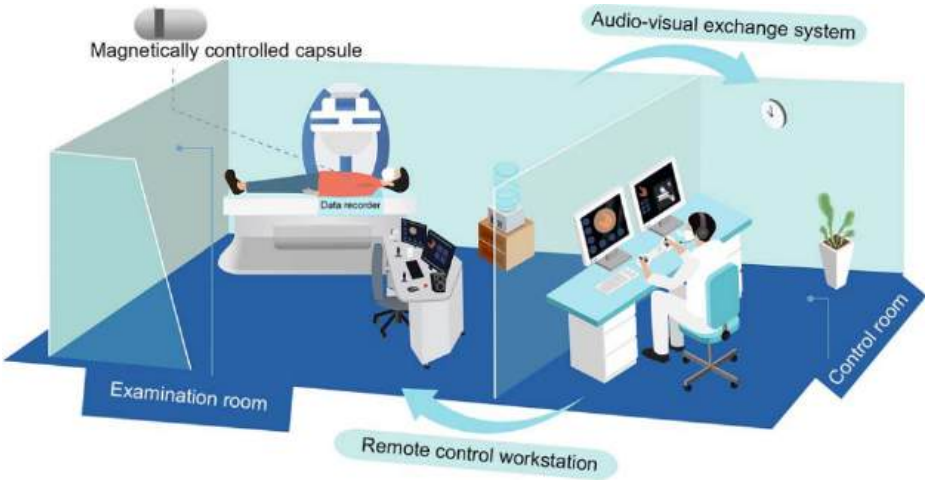

Figure 2.2: The non-contact magnetically actuated capsule endoscopy system. From [28].

A typical commercial capsule endoscopy system consists of four primary components: a magnetic actuation mechanism, a capsule endoscope, an audiovisual communication system, and a remote-control workstation, as shown in Figure 2.2. This configuration enables remote navigation of the capsule within the body, real-time data transmission, and external control without direct physical contact. Magnetic actuation in these systems is commonly achieved using either movable external magnets or electromagnetic coil systems [5]. The CE robot's driving mechanism operates by generating an external magnetic field, which interacts with the internal permanent magnet or electromagnet within the capsule, producing forces and torques to control its movement and facilitate medical tasks [29, 30]. These magnetic forces and torques

can either act independently or in combination to control the movement of the capsule robot precisely.

The following paragraph will outline several areas of capsule endoscopy that warrant further improvement. As mentioned in the Chapter Introduction, the most severe complication is capsule retention, which can lead to small intestine obstruction and potentially severe consequences. Additionally, there is an increased recognition in the importance of interactions within the intestines contributing to the inefficiencies or inadequacies in capsule robot systems [23, 31]. In some capsule endoscopy systems, the movement of the capsule robot is not controlled and relies entirely on peristalsis at the lower GI tract, which can result in unpredictable travel paths and limitations in the precision and completeness of disease detection [32–34]. If the obtained images are unclear or missing of a certain region for some reason, there is no second chance to retake the images. Future advancements in capsule endoscopy robots aim to expand their capabilities, enabling them to perform therapeutic delivery, tissue biopsy, lesion marking and other medical tasks [22, 35].

2.2 Literature survey

2.2.1 Tribology of capsule endoscopy

2.2.1.1 Friction resistance measurements and modelling

Although several driving systems are available to be applied in capsule robots, the technical difficulties have not been fully solved or understood clearly. For example, the six primary functional modules are subject to different weakening degrees due to size constraints as shown in Figure 2.3. At this point, it is vital to understand friction behaviour inside the body, which provides essential information for the design of robot model shape, propulsion force, power capacity and other design parameters. Therefore, the friction models of some papers are reviewed for a better understanding of the current research state.

In 2004, N. K. Baek et al. investigated the effect caused by the change of capsule geometry on the frictional resistance inside the intestine [36]. One set of Aluminium and plastic specimens was different in terms of geometry of contact. Another set was concerned with providing different values of length or diameters for one similar capsule shape, as shown in Figure 2.4. The experiments were conducted using a

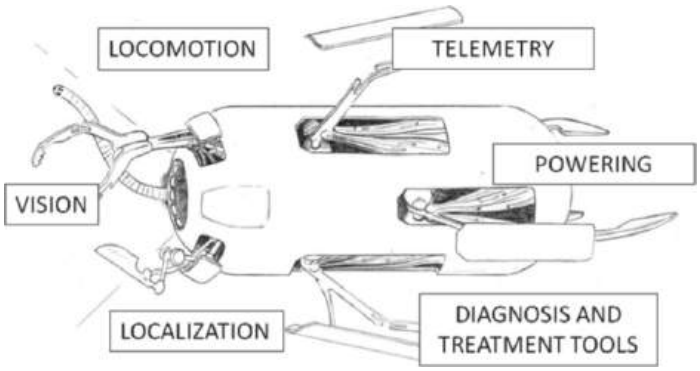

Figure 2.3: Six basic modules of a capsule robot (courtesy of Virgilio Mattoli) [3].

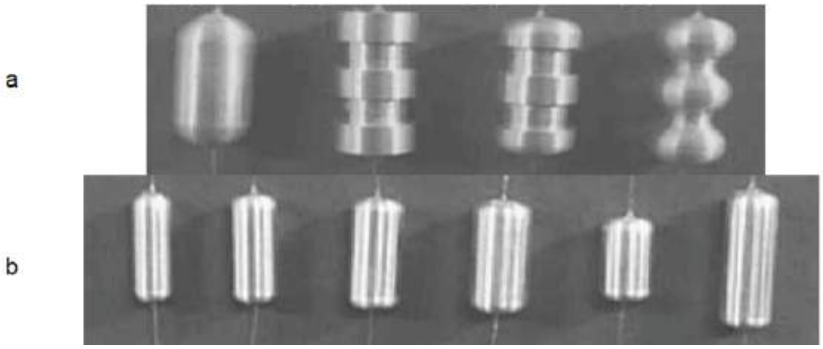

Figure 2.4: Photos of different designs of capsule robots: (a) First set of capsules with different geometries; (b) Second set of similar shapes of capsules in different dimensions. All designed by N. K. Baek et al. [36].

self-designed test rig equipped with various gauges and sensors to pull the specimens inside porcine small intestines. The authors found that the larger contact areas and sharper capsule corners would raise the friction forces from the experimental results. Also, the change in diameters had a much greater impact on friction than changing the length, despite the surface area changing more significantly with length. Experimental results revealed that while a 5 mm increase in length and a 1 mm increase in diameter corresponded to surface area changes of approximately 140 mm^2 and 80 mm^2, respectively, the resulting increase in frictional force was similar in both cases. The explanation was if the intestine expanded radially, the hoop stress along its circumference increased, leading to a rise in the normal load on the capsule. Consequently, an increase in capsule diameter can amplify the frictional force, as friction was directly proportional to the normal load.

X. Wang et al. also conducted similar experiments to measure motion resistance for a range of capsules passing through the porcine small intestine [37]. As shown

in Figure 2.5, 15 ABS plastic capsules of different parameters were tested inside the pig intestine. The same conclusion of the effect of capsule dimension on friction was reached compared with that of N.K. Baek [36]. The influence of capsule weight and the moving speed of the capsule was also studied. Results indicated that the friction force increased with the increasing moving speed increased. At the same time, the weight had a relatively much smaller effect that could be neglected in terms of the actual weight of the capsule as a consequence of the viscosity of the intestine. Alternatively, this result can also be verified in the study of J.S. Kim et al., who used different cuboid blocks to slide on the porcine tissue [38]. In addition, Kim developed a viscoelasticity model that can be used to analyse the stress relaxation of the small intestine which was widely adopted in later research.

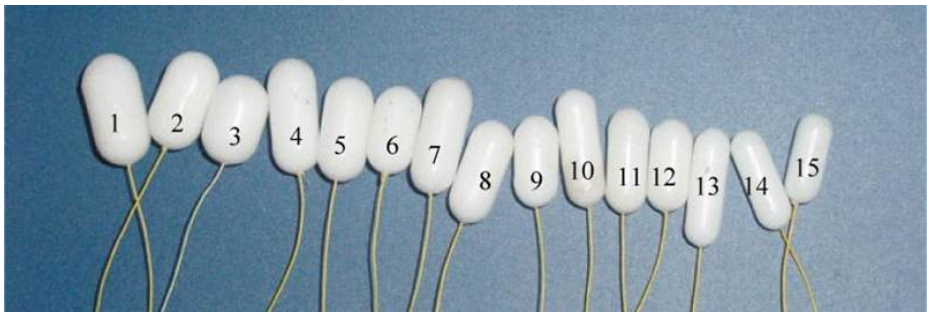

Figure 2.5: Picture of 15 capsules of different dimensions designed by Wang et al. [37].

Apart from the research on the experimental results on capsule shape, various mathematical modelling of the friction resistance was also carried out by different researchers.

S.H. Woo et al. developed a small intestine model to analyse the moving speed, friction, and contraction force of an electric stimulus capsule robot [39]. The electrodes on the capsule could stimulate the intestine at a particular frequency and voltage, producing a contraction force that squeezes the capsule to move. During the locomotion, the capsule was also hindered by the friction influenced by the capsule geometry and drag force influenced by the capsule velocity and intestine elasticity. Thus, the force diagram related to these parameters was applied to calculate the acceleration and speed. The simulated velocity results were very close to the experimental results within a 5% deviation that proved the accuracy of the model calculation. The team also found out that the streamlined geometry would acquire a more significant

contraction force than that of the cylindrical shape because of the influence of contact angle on the horizontal component. However, the model cannot be designed in extreme shape, and it was also restricted by the volume requirement for the internal devices.

Meanwhile, B. Guo et al. structured a similar mathematical modelling method that used nearly the same theoretical analysis on the hoop stress onto the deformed intestinal wall for a Vibro-impact capsule [33]. The difference was that Guo et al. used a 3-element Maxwell model that fitted with their stress-relaxation test to express the stress-strain relationship of the viscoelasticity property, and no contraction force and drag force was considered in their model [40]. Four possible situations: open, open with circular folds, covered and expansive state of the tissue were tested, and the FEA, numerical and experimental results also revealed the friction force was sensitive to the change of the capsule diameter as shown in Figure 2.6.

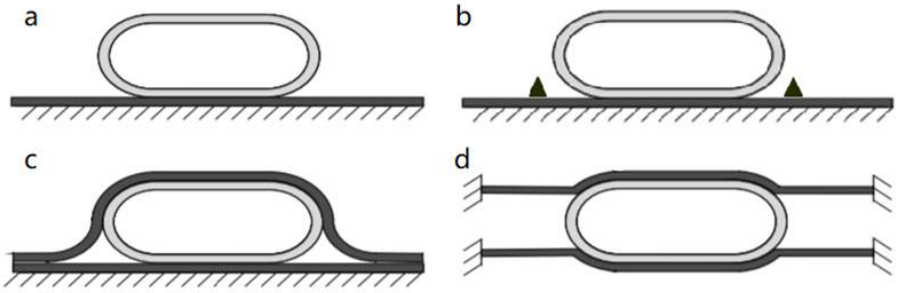

Figure 2.6: Four states of contact conditions: (a) Open; (b) Open with folds; (c) Covered; (d) Expansive. Adapted from [33].

Z. Wang et al. established a 5-element viscoelastic model for a passive capsule robot that the natural peristaltic force of the small intestine was considered as the propulsion power [41]. The model was built based on the stress relaxation theory composed by Kim et al. [38], and the peristalsis of the intestine was simplified as a sine wave as shown in Figure 2.7. Therefore, the displacement change was known and could be substituted in the model to determine the stress. Then, the force applied onto the capsule was calculated using the surface integral, and the overall frictional resistance force was calculated using MATLAB software. The team analysed the increment of different parameters to figure out the more significant effect factor for the value of friction force. Besides, the conclusions about the capsule diameter, velocity and contact angle were similar to other works. Moreover, the team also found that

the amplitude of the peristaltic wave is influenced greater than the wavelength, which means the small intestine contraction plays a significant role in frictional resistance.

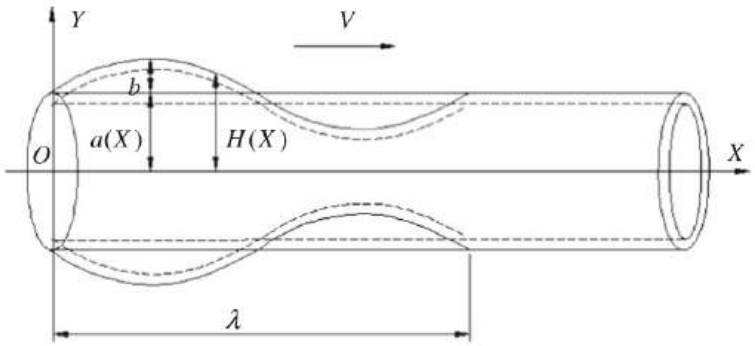

Figure 2.7: Schematic drawing of the simplified 'sin' wave of the peristalsis. From [41].

Most of the studies were investigated assuming static conditions or constant sliding motion, but the frictional behaviour in the starting process with appropriate control is rarely noticed. C. Zhang et al. carried out research that aimed to determine the variation of the initial friction resistance [42]. The tests were conducted by pulling a resin capsule within the porcine intestine in the process of uniform acceleration, uniform velocity, and uniform deceleration with different sets of velocity and acceleration as shown in Figure 2.8. Thus, friction force can be calculated as the resultant force of the pulling force and the force acting on the capsule. According to the data fitting of these experiments, an approximately linear relationship between the friction force and time at the initial stage was shown. Also, the mean value of the frictional force of the capsule under constant velocity was only affected by speed and not by acceleration. Furthermore, a quantitative analysis of the frictional resistance effect caused by acceleration and velocity was carried out.

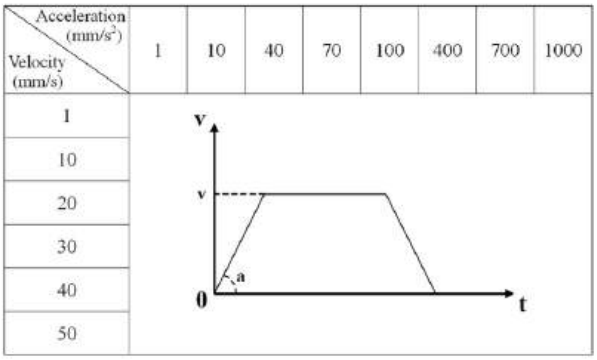

Figure 2.8: Velocity versus time graph of different processes of uniform acceleration, uniform velocity, and uniform deceleration. From [42].

The frictional behaviour of the capsule under constant velocity was also studied by C. Zhang's group [43]. The results showed that the friction force fluctuated irregularly like waves at a constant velocity. The authors established a quantitative model to analyse the material property of the intestine. The intestinal wall was regarded as a hyper-elastic material, and the interactive model was further simplified as a slider (capsule) sliding on a reciprocal car (intestine) as shown in Figure 2.9. The simulation result indicated a regular fluctuation with similar average amplitude and wavelength compared with the actual values. Besides, the limitation of the equivalent physical model was discussed in neglecting the boundary conditions of the intestine while the validity was needed further proof [44].

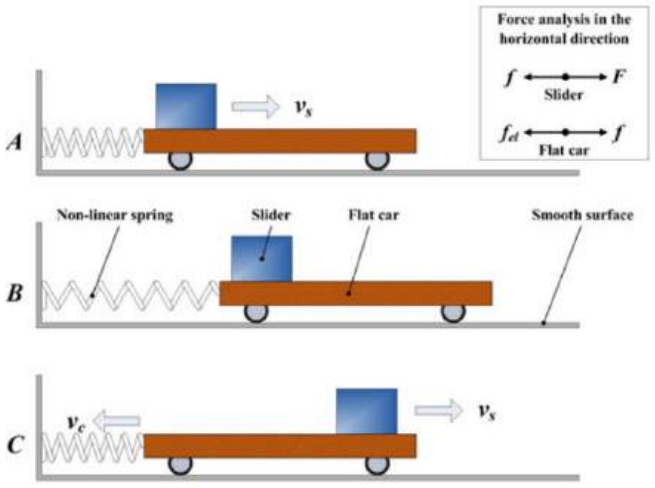

Figure 2.9: Equivalent physical model of the capsule (slider) and the intestine (car). From [42].

L.J. Sliker et al. analysed a situation of a cylindrical capsule with an external permanent magnetic (EPM) actuation system that only partially contacted the GI wall at a constant velocity [45]. Unlike the above research, the hoop stress was not applicable under this condition. In addition, the shape function of tissue fold caused by the compression of the capsule and the 5-element Double Maxwell-arm Wiechert (DMW) for the viscoelastic intestinal wall were generated. This 5-element DMW model, designed by X. Wang et al., was verified as the performance of model fit was improved by 35% than the standard linear solid viscoelastic model [46]. Thus, the known deformation and stress-strain relationships could express the total frictional resistance of different parameters of a capsule. The model was validated with an overall normalized root-mean-square error of 8.81% by comparing the outcomes with experimental results. The simulation results implied that the most influential impact factor was the radius of the edge of the capsule rather than velocity. The effect of length, diameter and weight were tiny compared with the above two significant factors.

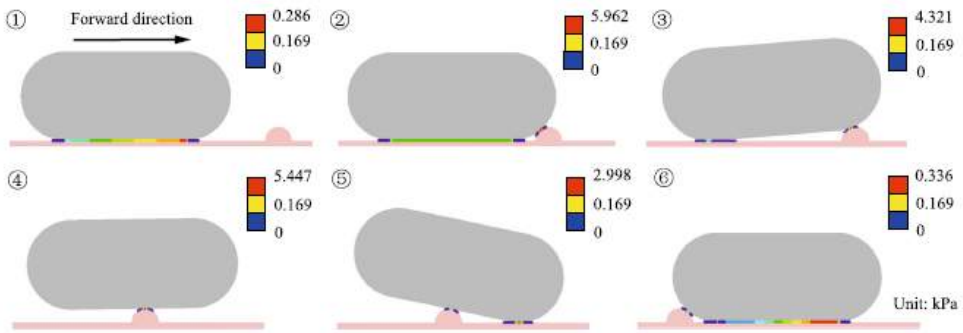

Figure 2.10: FE diagrams illustrating the intestinal contact pressure at six different stages as the capsule traverses the circular fold. From [48].

Differing from the static resistance model created by Sliker, Y. Yan et al. developed and analysed a vibro-impact self-propelled capsule specifically designed to navigate dynamic movement of overcoming obstacles like circular folds [47]. Their work incorporates a mathematical model that simulates the capsule's dynamic interactions with circular folds, factoring in variables such as capsule mass, stiffness, damping, and external driving forces. The model also considers the mechanical properties and geometry of circular folds, as they represent a primary source of resistance in the intestine. Their findings indicate that increased capsule mass and fold height delay traversal, requiring stronger forces to overcome resistance. These factors are critical for optimizing capsule performance and guiding design considerations. In another

study by Y. Yan et al., a 2-dimensional finite element (FE) model was used to simulate capsule-tissue interactions due to the computational demands of 3-dimensional simulations [48]. This FE model provided a realistic approximation of tissue deformation and force dynamics, particularly during key stages of fold interaction as shown in Figure 2.10. When results were compared with experimental data, the study found that maximum resistance occurs at the initial contact between the capsule head and the fold. Notably, the rotational stages were shown to play a crucial role in enabling the capsule to move over the fold. By complementing the analytical model with a more realistic, step-by-step FE simulation, this approach offered critical insights for designing endoscopic capsules capable of navigating intestinal obstacles effectively.

C.X. Lin et al. performed experiments by sliding a stainless steel ball (15 mm diameter) onto the prepared oesophageal wall using a UMT machine as shown in Figure 2.11 [49]. The coefficient of friction (COF) decreased from approximately 0.4 to around 0.2 as the normal load increased from 0.2 N to 1 N because the liquid stored in wrinkles or grooves (villi and microvilli structure) within the tissue would be squeezed out to decrease the friction coefficient via lubrication. Many other researchers neglected the effect caused by the mucus or mixture of intestinal juice and chyme, which should be considered in future studies.

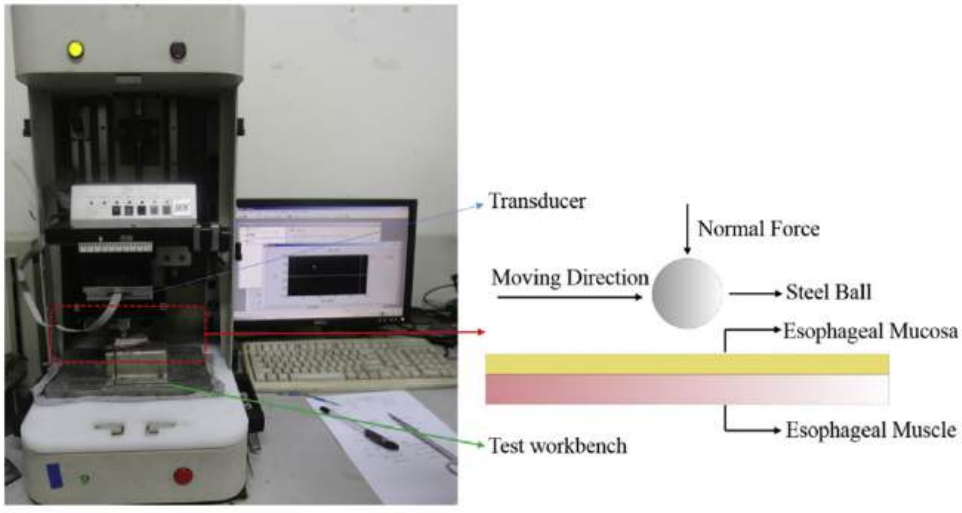

Figure 2.11: Use UMT to conduct friction experiments for esophageal tissue and its relative schematic diagram. From [49].

2.2.1.2 Capsule robot prototype developments and locomotive systems

During the development of CE, various prototypes and locomotive mechanisms were designed to overcome the battery and actuator limitations, volume size, weight, and other constraints. The locomotive systems can be divided into two categories, active and passive propelling systems. Several designs of active capsule robots are introduced to understand these systems related to tribology.

In the early 2000s, CE robots were always designed to equip active self-propelling systems with many electronic components. However, due to the limited scientific and technological conditions at that time, CE robots at that time could not be manufactured in capsule size. More precisely, they can be regarded as macroscale prototypes. Despite that, many designs still play an essential reference role in follow-up research.

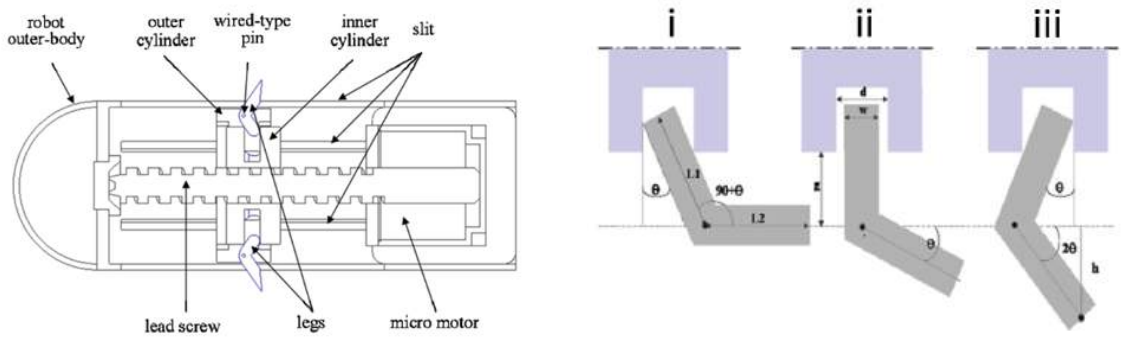

(a) (b)

Figure 2.12: A single-direction propelling capsule robot designed by H. Park et al.: (a) Concept structural diagram of the capsule robot; (b) Three states of leg in rotation: (i) Folded, (ii) Normal, and (iii) Protruded position; From [50].

In 2007, H. Park et al. proposed a single-direction propelling capsule robot equipped with six legs [50]. The locomotive mechanism was inspired by the human actions of arms when performing the paddling of a canoe as shown in Figure 2.12a. Specifically, the clearance between the legs and the groove enabled the rotation of legs within a specific angle range to complete the condition of protrusion for interlocking and folding inside the cylinder for movement as shown in Figure 2.12b. Also, the authors researched the effects of friction influenced by the parameters design of the legs by experiments. The results verified that longer and thinner legs could increase the locomotion of the microrobot as the deformation of the intestine was aggregated with smaller contact areas. The authors made two in-vitro tests where the robot

was placed inside the cut pig intestine and travelled in specific paths (a straight and half-circle on-board path and several 3-dimensional bridged paths with different slope angles). The experimental velocity was lower than the expected value because of the negative effect of the gravity and the slope. One in-vivo test inserted the robot into the pig big intestine through the anal orifice, and an X-ray was used to monitor the motion.

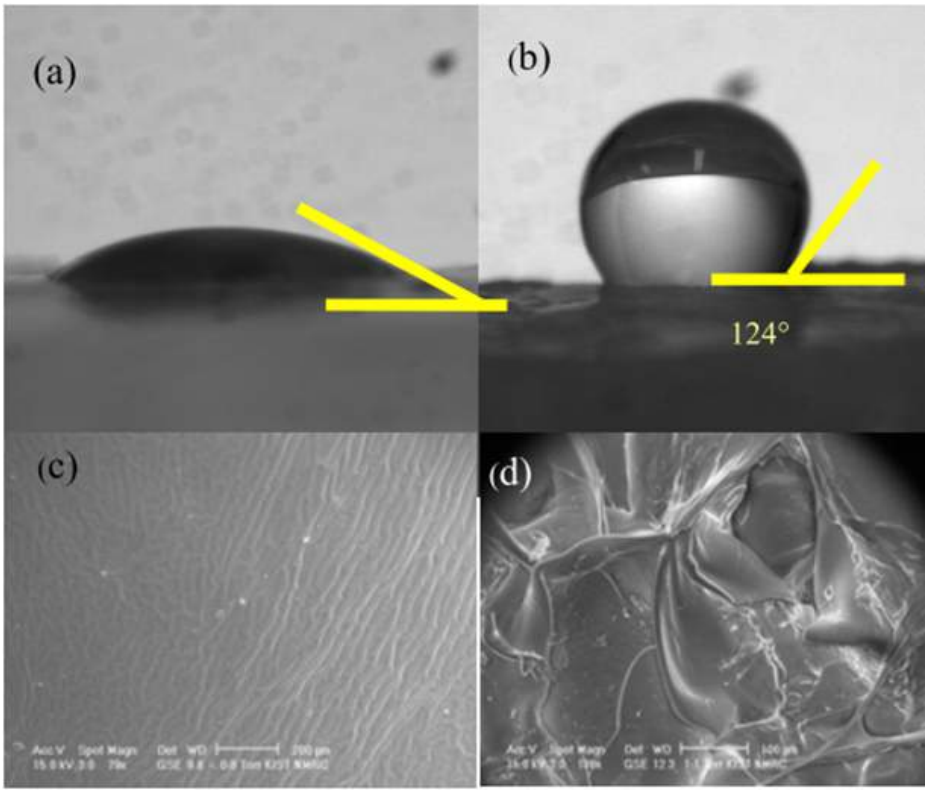

Figure 2.13: Comparison of contact angle after 4 minutes heating of PNIPAAm: (a) Initial state; (b) 4 mins heating. Environmental scanning electron microscope photo of the surface texture (c) hydrophilic; (d) hydrophobic. From [51].

Two years later, B. Kim et al. brought a new concept of using the poly N-isopropylacrylamide (PNTPAAm) hydrogel (non-toxic) to build clampers for the capsule robot [51]. Heating PNTPAAm would transfer this material from a soft hydrophilic hydrogel into a hard hydrophobic condition. This transformation in roughness would also influence the friction, as shown in Figure 2.13. Moreover, improvements of synthesized Alginate with PNTPAAm were made to increase the strength property and minimize the time for heating. In-vitro tests on the pig intestine demonstrated the feasibility of this combination. The overall time consumption for heating

and cooling might be a problem, but it was not mentioned in detail in the paper.

J. Kwon et al. designed an earthworm-imitated locomotive mechanism for their capsule robot, and the 'critical stroke' of it was evaluated [52]. Coincidentally, J. Gao et al. implemented an inchworm-like capsule robot which adopted a similar locomotion system [53, 54]. The structure of the robot was simple, two segments would be locked onto the intestinal wall separately to complete the elongation and retraction processes and move forward as shown in Figure 2.14a. It is significant to note that the authors ignored the effect caused by the mucus but considered the existence of the mesentery. The critical stroke was the minimum length of the stroke-related to the mesentery's elastic modulus. This definition was set to ensure the mobility of the robot and that the real stroke must be larger than the relative slipping length. Thus, the numerical modelling of the friction force between the wall and the robot was conducted under several ideal assumptions as shown in Figure 2.14b. The conclusion was that the critical stroke and the elastic modulus were in inverse proportion. In other words, the stroke should be designed shorter if the elastic modulus is high. For verification of the frictional model, the in-vitro test results were similar to the simulated results.

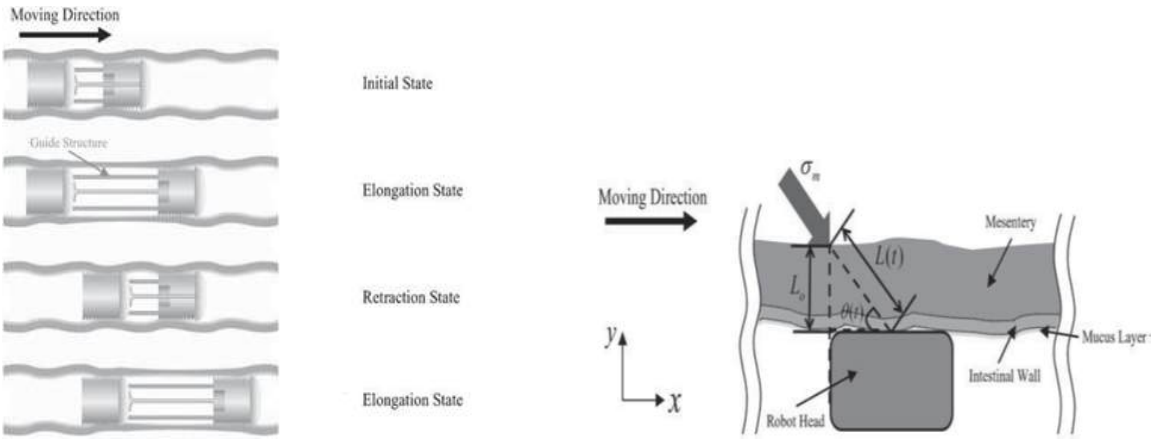

(a) (b)

Figure 2.14: An inchworm-like capsule robot designed by J. Gao et al.: (a) Four states of earthworm-like locomotive mechanism; (b) Stress analysis diagram of the robot contact head; From [52].

Similarly, the design of a stretchable robot advanced by Y. T. Kim et al. that used similar core components to the prototype of J. Kwon is shown in Figure 2.15 [55]. The difference is that the robot was covered with a rubber shell with many tentacles to

increase the friction. The tentacle was a barb-like wedge structure cut at a 45 angle, and the hollow part was filled with epoxy to increase its strength. In this way, the tentacle would experience low friction in moving forward but large friction in moving backwards that perfectly met the requirement. The test results in the pig intestine showed a velocity of 27mm per minute which was suitable for actual operation. The authors also proposed a novel propelling mechanism which the propulsion force was generated by the spiral motion of a cylindrical body powered by a motor [55]. The intestinal wall would twist with the rotational body to gain friction to move forward, so optimization of the dimensions (diameter, length) and the geometry (height, angle, and the number of the ridge) was completed by experiments. One thing that should be mentioned is whether the relative spin of the intestine will cause structural damage to the intestine was not explained in the paper.

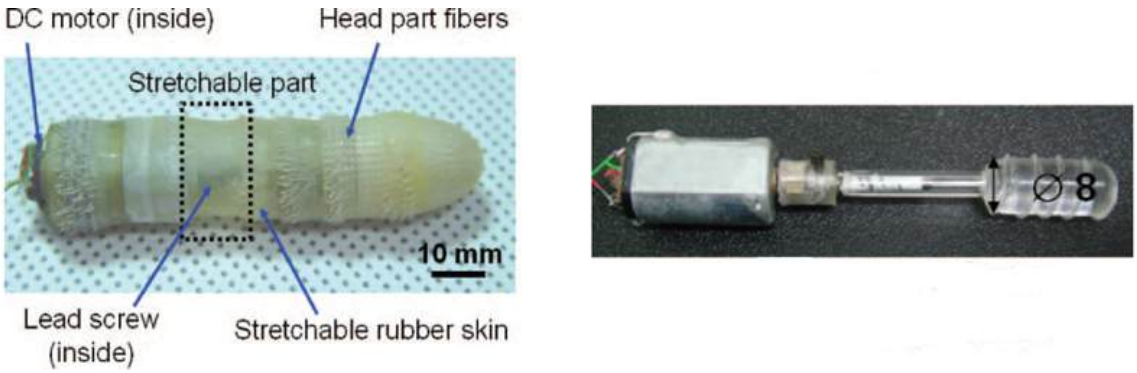

Figure 2.15: Photograph of the fabricated stretchable-body robot (left) and the spiral-body robot (right). From [55].

With the development of the technology, many powerful microelectronic components are improved, making it possible to invent the real swallow-able capsule robot as shown in Figure 2.16. Compared with the previous designs, although the designs are different in force-power transmission, contact end designs and other connection methods of internal parts, the overall locomotive systems are still the fundamental combination of anchoring and stretching [56–59]. The working principles of movement are similar to those described above.

K. Ota et al. designed a new driving system for the CE robot to produce self-propulsion [60]. The Self-Propelled Capsule Endoscope is connected to a silicon resin fin, 19 mm in length, which is embedded a micro-magnet. When placed in an alternating magnetic field, the micro-magnet vibrates, transmitting the motion to the fin,

which generates propulsive force in water. This enables controlled movement of the SPCE within the body, particularly in the stomach. By adjusting the magnetic field, three-dimensional control of the SPCE can be achieved. The system is operated using a dedicated controller, and real-time monitoring is facilitated through the RAPID Access system from Given Imaging Ltd., allowing precise navigation of the capsule during medical procedures.

Other active or passive locomotive mechanism designs such as the vibro-impact and magnetic-driven systems were only different inside the capsule body. The outer casing shows a high similarity to the capsule shape, and no constitutions of contact end are needed. The resistance models of these are introduced above, so no more repetitive details are described here.

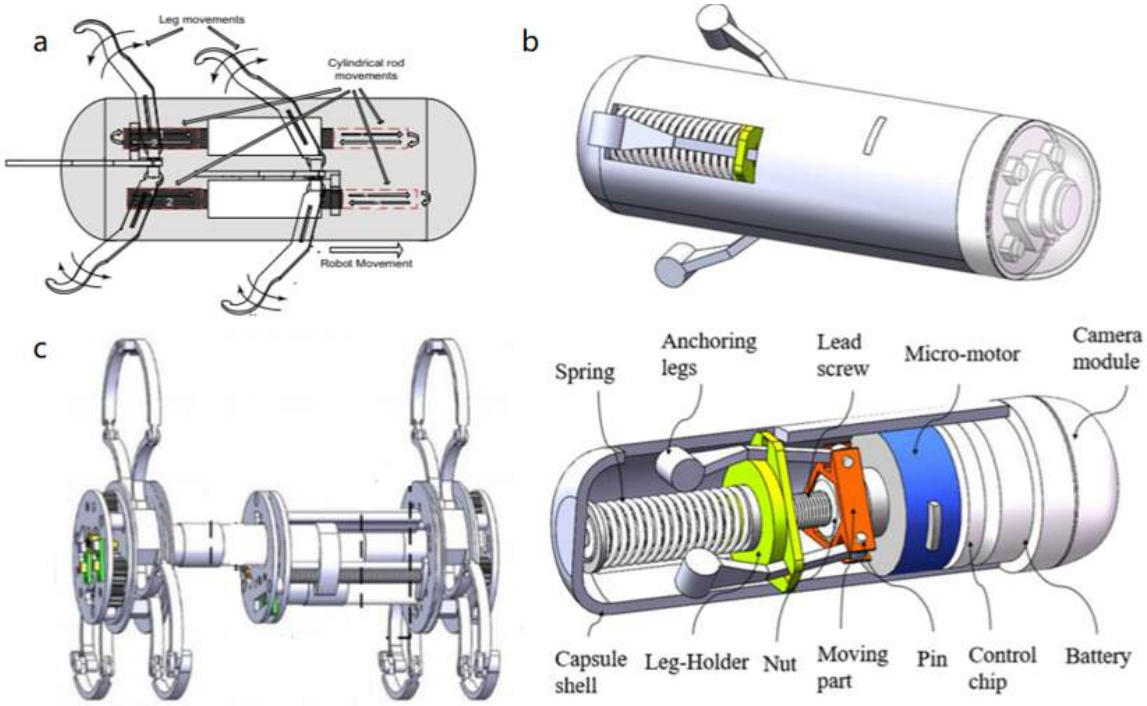

Figure 2.16: Three designs of the mechanical structure of the capsule robot (a) Design of M. N. Huda et al. [56]; (b) Design of F. Zhang et al. [57]; (c) Design of W. Wang et al. [59].

2.2.1.3 Contact condition

The moving 'limbs' of the capsule robot play a vital role as it provides mobility with sufficient stability. Consequently, the contact ends of the limbs are often designed

to be relatively sharp to ensure that sufficient friction can be provided for meeting the work requirement and completing the locomotion within the human body [61]. However, these tapered legs could also cause damage to the intestine. Therefore, in order to address the point of safety, several studies were organized, as shown below.

In 2008, P. Glass et al. attempted to apply the soft elastomer micropillar matrix onto the legs of the capsule robot for anchoring stably [62]. The micropattern elastomer adhesives were made by biocompatible polymer polydimethylsiloxane (PDMS) that were bio-inspired by the feet of geckos and insects as they could increase the contact areas so as the friction force as shown in Figure 2.17. Mathematical models were built based on the momentum equilibrium of a single leg and the static equilibrium of the whole capsule body with the peristatic force of the intestine. The simulation results were compared with the experimental results to figure out the friction force generated by this design separated from the edge effects of other parts. It turned out that the friction force was two times larger than before approximately. Also, the authors tested the effect of the silicone oil layer added onto the pillars further expanding the friction force to about four times the original.

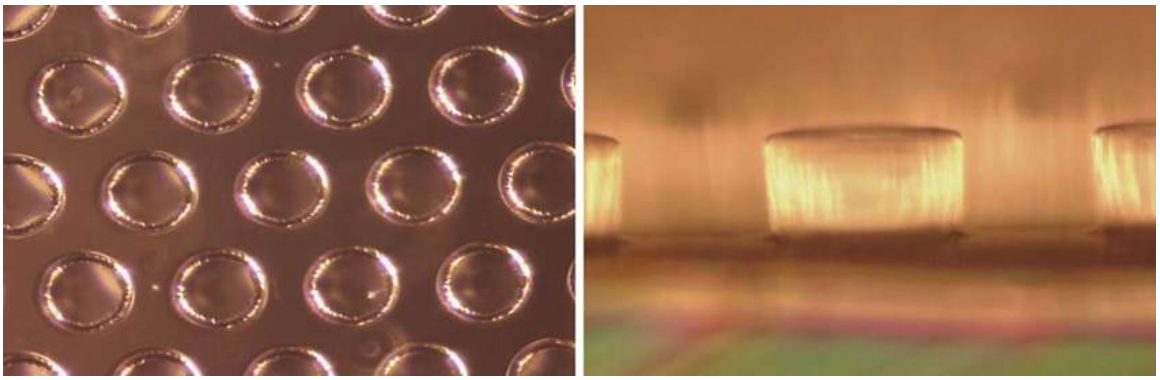

Figure 2.17: The top view of the elastomer micropillar matrix (Left). The side view of a single low ratio pillar (Right). From [62].

E. Buselli et al. shared a similar idea of applying soft polymer micro-patterns onto the legs to enhance friction [63]. Perfluoropolyether was used as an alternative material, and the micropillar pattern was fabricated by the soft lithography technique as shown in Figure 2.18b. The low ratio hollow pillar allowed to absorb the mucous, so the lubrication effect is weakening.

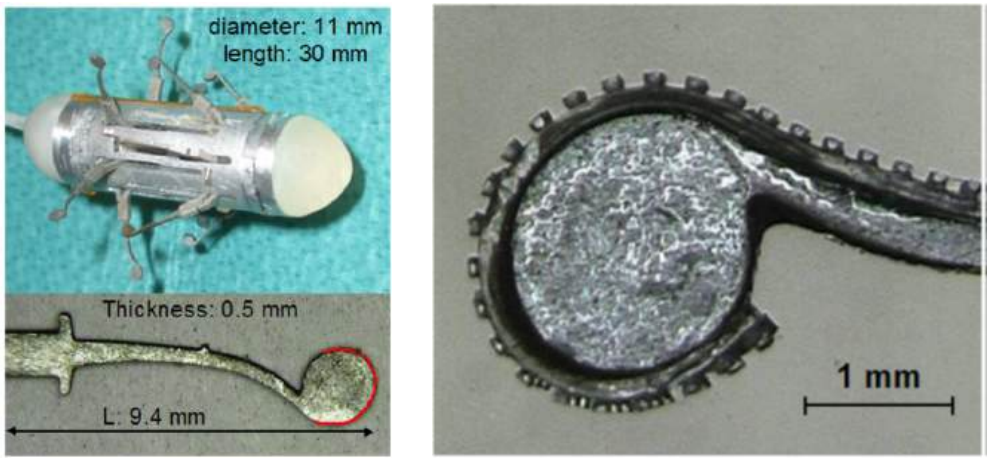

(a) (b)

Figure 2.18: Design of E. Buselli et al.: (a)Photo of the capsule robot;(b)Photo of a capsule leg embedded with micro-pattern pillars; From [63].

Instead of proceeding from the materials and coating layer, Y-T Kim et al. focused on the interlocking effect on the friction caused by the contact geometry [64]. The group designed the alternative steel ball, polymeric tube, and acrylic rod tip of robotic arms inspired by the starfish's biological structure as shown in Figure 2.19. Different tip designs including flat flexible tubes, and rigid tip rods with and without ball tips were tested on sliding reciprocally on the open pig intestine for researching the frictional behaviours in terms of flexibility and cross-sections. Moreover, a four-tube tip, a hard-hollow tube, and several multiple tube tips were performed to determine the influence of tube numbers and contact conformity. Results reflected that the multiple flat tips had the best performance on obtaining friction. The reason is that the tube was flexible enough to bend at a certain angle during sliding with a more considerable interlocking effect. Also, the tissue would penetrate inside the hollow tube, increasing the degree of interlocking than the rigid rod. However, the authors did not obtain the best bending angle, and the best number and distribution of legs were not provided which needs further study.

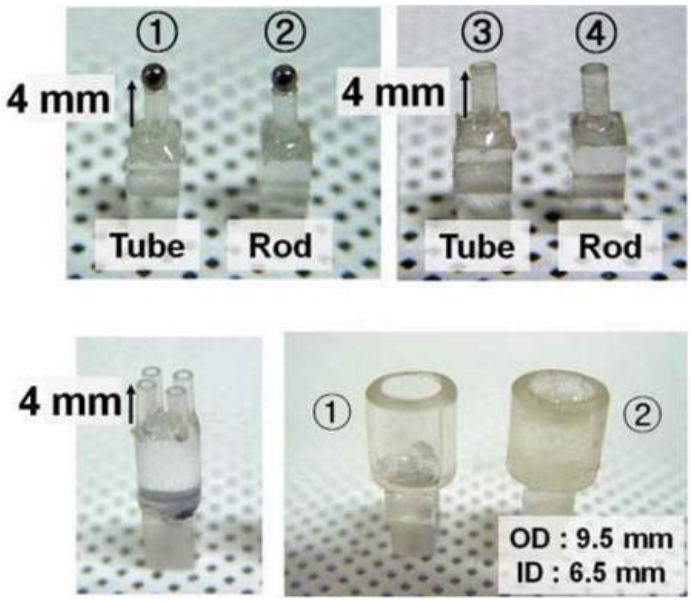

Figure 2.19: Design of steel ball, polymeric tube, and acrylic rod tip of robotic arms. From [64].

2.2.1.4 Discussion

This part of the review provides an overview of the mechanical and tribological aspects of CE, focusing on recent developments in propulsion systems, resistance models, and experimental validations. The section is structured into the summary of propulsion mechanisms and resistance models, critical reflections on the literature, and recommendations for future research.

CE propulsion systems can be categorized into passive and active types. Passive capsules rely on intestinal peristalsis for movement. Despite being a significant advancement over traditional wired endoscopes and having commercial products like PillCAM, their performance often remains suboptimal in clinical settings [65]. The slow peristaltic motion extends examination time, and the lack of manoeuvrability compromises lesion localization and image quality [66, 67]. For the area of active capsule robots, research is still in the development stage. Active capsule robots are divided into internally and externally powered types. Internally powered capsules integrate batteries and actuators within the capsule shell to facilitate self-propulsion via mechanisms like paddling or earthworm-like motion. However, internal systems are bulky due to component requirements, leading to higher friction and reduced flexibility. Externally powered systems use magnetic fields to guide the capsule, offering better swallow-ability and faster transit. Yet, precise control remains challenging,

limiting their diagnostic and therapeutic capabilities, including tasks like biopsy and drug delivery [52,55]. Addressing these limitations necessitates a deep understanding of tribological interactions within the GI tract. High friction aids propulsion, while low friction minimizes tissue damage, suggesting a need for switchable friction modes.

To model intestinal resistance, several parameters such as capsule shape, size, and speed are analysed. Simplified assumptions are typically made: uniform tissue deformation around the capsule and straight, symmetrical intestinal geometries. Viscoelasticity of the tissue is modelled using 3- or 5-element Maxwell models, with strain linked to capsule geometry. Capsule diameter significantly impacts resistance due to hoop stress, and streamlined shapes are preferred. Notably, soft tissue friction does not follow classical laws; it increases with speed due to viscoelastic effects. Friction is further examined through static (start-up) friction, crucial for locomotion systems using legs or paddles. Excessive slip can damage tissue, necessitating careful design.

Stick-slip behaviour, caused by cyclic deformation and release, results in fluctuating friction forces. Resistance models thus help refine design parameters. To enhance traction, researchers have experimented with different materials and surface textures on contact tips of CE robots [61–63]. Results indicate significant friction increases, but further exploration of pattern shapes and arrangements is needed. Bio-inspired designs and hydrodynamic optimization could offer further improvements.

In-vitro tests are used to validate resistance models, often involving porcine intestines due to their similarity to human tissue [68, 69]. Capsules are either pulled through intestines or dragged across intestinal tissue that has been cut open with efforts made to preserve tissue integrity for 5-7 hours post-extraction [70]. Nonetheless, significant differences from live tissue persist due to the lack of physiological responses [71]. Preservation methods and biological realism during testing require improvement. Most experimental platforms are custom-built and vary in design, complicating reproducibility. Common issues include deviation from intended paths due to uneven surfaces and challenges in simulating realistic loading conditions. While some studies use soft substrates, true mechanical fidelity remains questionable [33, 43–45]. Given the small intestine's soft, coiled nature, the surrounding environment also contributes to the frictional response. Improved base materials and fixation methods are needed to replicate physiological conditions. Additionally, the realistic hydrated

conditions of the intestine are often neglected.

Future research should prioritize developing more accurate experimental and computational models that incorporate lubrication effects. Enhanced contact geometries to increase traction, as well as models simulating curved and asymmetric intestinal paths, should be explored. Sidewall stress at bends may hinder movement or cause retention. Safety evaluation is also underrepresented, most studies do not assess tissue condition pre- and post-experiment. While minor damage may be tolerable in healthy individuals, it could be harmful in diseased tissue. Hence, reliable monitoring and evaluation techniques are essential. In summary, understanding and optimizing the frictional behaviour of capsule endoscopy devices requires interdisciplinary research combining tribology and soft tissue mechanics. Advancements in these areas will support the development of safer and more effective capsule robots.

2.2.2 Anatomy of the small intestine

The small intestine, a crucial organ in the abdominal cavity, links the stomach's pylorus at its upper end to the large intestine at its lower end through the appendix gate [72]. It plays a central role in digestion and nutrient absorption. Coiled within the abdominal cavity, the small intestine spans approximately 4 to 6 meters in length and has an average diameter of 3 to 4 centimetres [72].

2.2.2.1 Structure

The small intestine has three functional subdivisions: duodenum, jejunum, and ileum, as shown in Figure 2.20. The diameter of the small intestine gradually tapers down from the duodenum (around 3 cm), and the terminal ileum lumen is only 1.8 cm [74]. The duodenum is located in the posterior upper part of the abdominal cavity, with a total length of about 25 cm. The jejunum connects the duodenum, accounting for two-fifths of the total length of the small intestine and is located in the upper left part of the abdominal cavity. The ileum is located in the right lower abdomen, accounting for the rest of the total length of the small intestine. There is no clear dividing line between jejunum and ileum. Compared with the jejunum, the ileum has a thicker tube wall, a more developed blood vessel wall and more mucosal folds.

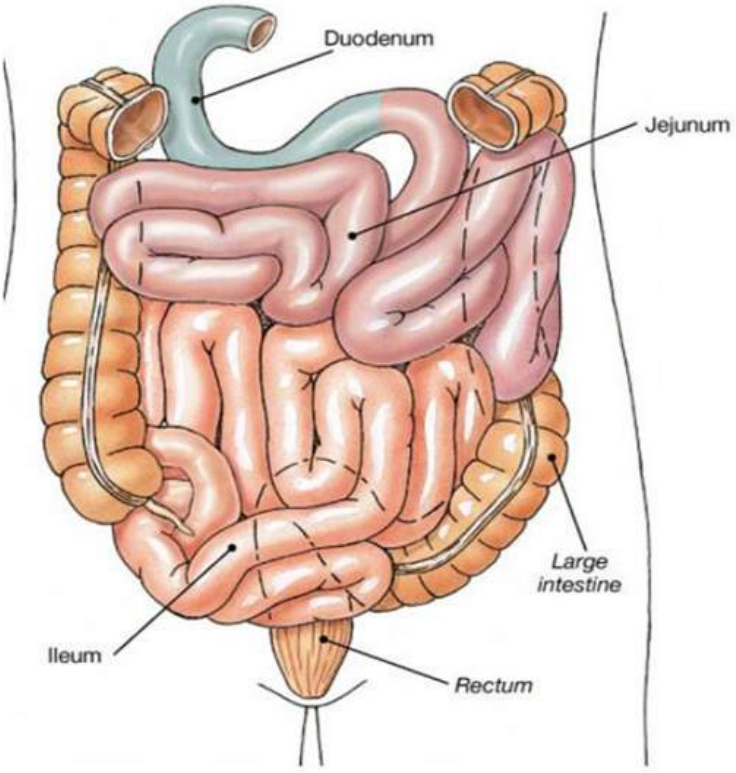

Figure 2.20: Physiological structure of the small intestine. From [73].

2.2.2.2 Histology

Many hemispherical folds on the luminal surface increase the area for absorption of the small intestine as shown in Figure 2.21. The positions that contain most of the circular plicae are the middle jejunum and the proximal ileum, around the proximal two-thirds of the small intestine. There are many small finger-like protuberances on the surface of the annular fold, called villi. The number of villi is about 20 to 40 per mm^2, and the length of the villi is about 0.5 to 1.5 mm [75]. The existence of circular folds and villi expands the surface area of the small intestinal cavity, which is conducive to the digestion and absorption of the small intestine.

The small intestine has the function of secretion of small intestinal fluid. Ordinary people secrete around 2 litres of small intestinal fluid continuously every day [75]. Under different conditions, the properties of small intestinal fluid also change considerably, sometimes it is a thinner liquid, and sometimes it is very viscous because it contains a large amount of mucin [76]. Intestinal fluid is often mixed with exfoliated intestinal epithelial cells, leukocytes and immunoglobulins secreted by intestinal ep-

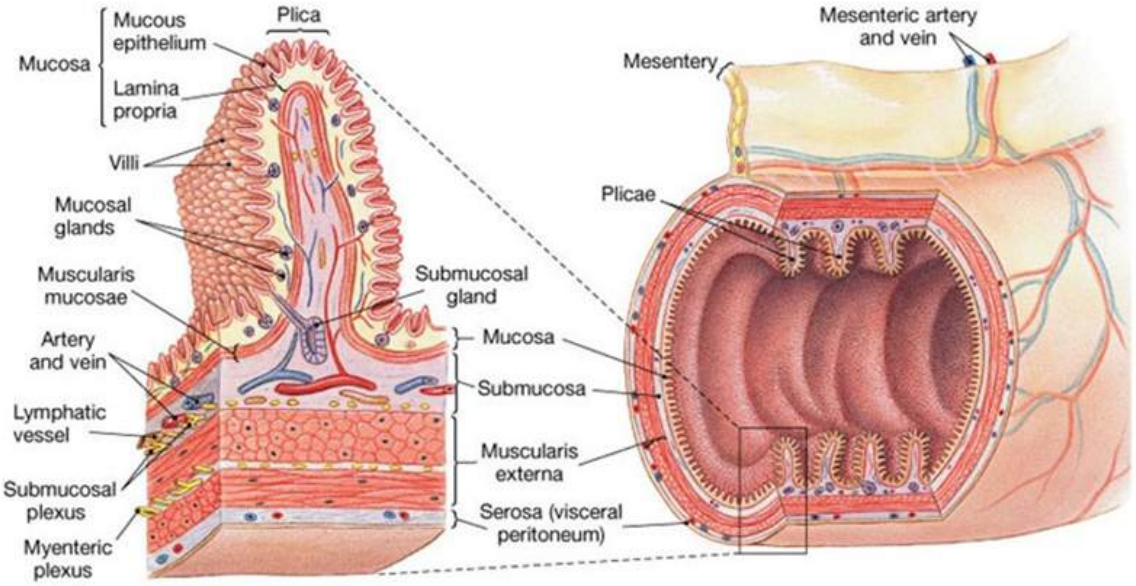

Figure 2.21: Structure of the small intestinal wall. From [73].

ithelial cells.

2.2.2.3 Motility mode

The motility of the small intestine includes three patterns: tonic contraction, segmental movement and peristalsis [77].

a) Tonic contraction
Tonic contraction of the small intestine is the basis for other forms of movement to be carried out effectively. When the tone of the small intestine decreases, the intestinal lumen is easy to expand, and the mixing and transport of intestinal contents are slowed down; on the contrary, when the tone of the small intestine increases, the mixing and running process of chyme in the small intestine accelerates.

b) Rhythmic segmentation
The rhythmic contraction and relaxation exercise with circular muscles is the mainstay of dividing chyme. In the section of the intestine where the chyme is located, the circular muscles contract at many points at the same time, dividing the chyme into many segments; then, the original contraction is relaxed, and the original diastolic contraction, so that the original segment is divided into two halves. The two adjacent halves are brought together to form a new segment,

repeated in this way, and the chyme can be continuously separated and mixed, as shown in Figure 2.22. The propelling effect of the segmented movement is minimal. Its function is to make the chyme, and the digestive juice is thoroughly mixed to facilitate chemical digestion. It also causes the chyme and the intestinal wall to be in close contact, creating good conditions for absorption.

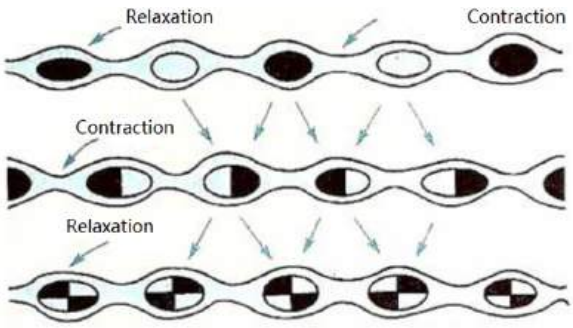

Figure 2.22: Contraction and relaxation diagram of the segmentation. Adapted from [78].

c) Peristalsis

The peristalsis is the natural driven force for the food mass (which could also be applied to the passive CE robot) to travel through the small intestine as shown in Figure 2.23. The peristalsis of the small intestine can occur in any part of the small intestine, and its speed is about 0.5 to 2.0 cm/s [79]. The peristalsis of the proximal small intestine is faster than that of the distal end. The peristaltic waves of the small intestine are very weak and usually disappear after only a short distance (approximately a few centimetres). The significance of peristalsis is to push the chyme that has undergone segmental movement forward, reach a new intestinal segment, and then begin segmental movement. The actual advancing speed of chyme in the small intestine is only 1 cm/min, and it takes about 3 to 5 hours for chyme to move from the pylorus to the ileocecal valve [79]. This time length is also suitable for anticipating the time length for a passive capsule to travel through the entire small intestine.

2.2.2.4 Mucus layer

The mucus of the small intestine only has one layer, and the Mucin 2 (MUC2, a protein transcribed by the MUC2 gene and expressed in goblet cells of the intestine [81, 82]) is the most important and primary component [83]. This gel-forming type of mucus is loose, unattached and prone to sliding [76]. The viscosity of healthy gastric mucus

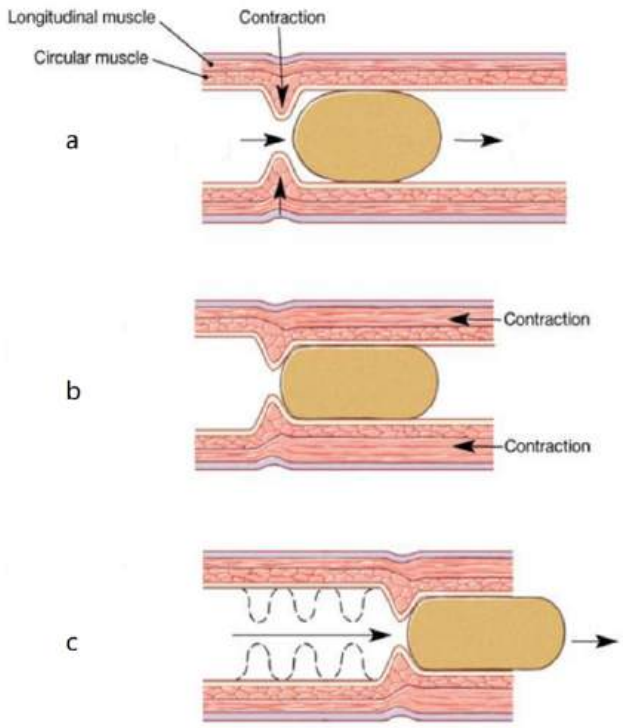

Figure 2.23: Schematic representation of intestinal peristalsis: (a) Circular muscle contraction occurring behind the bolus; (b) Longitudinal muscle contraction taking place ahead of the food mass; (c) Circular muscle contraction propelling the food mass forward. From [80].

tested at a shear rate of 1.15 s^{-1} was reported to be only around 0.085 Pa·s [84]. Nevertheless, if the physiological condition of the intestine is affected, such as through duodenal ulceration, the viscosity might increase significantly. Experiments were carried out to determine the thickness of the mucus gel layer in vivo by C. Atuma et al. [83]. A micropipette was pushed into the mucus gel at a known angle to the cell surface. The distance was measured using a 'digimatic indicator', then the thickness could be obtained by the simple trigonometric function. The mucus gel was removed by suction and recovered repeatedly for the next rounds of testing. The results from this study are shown in Figure 2.24.

2.2.2.5 Tissue preservation

As mentioned earlier, once excised, the small intestine tissue exhibits significant differences in tissue viability and mechanical response compared to active, in vivo tissues. To achieve more accurate and reliable data, this part of the review also consulted

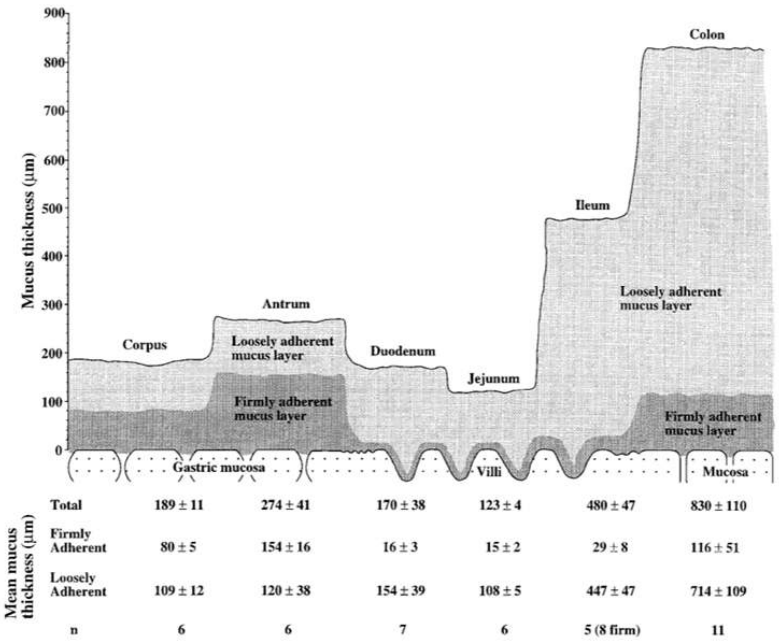

Mean mucus thickness (µm)							
	Total	189 ± 11	274 ± 41	170 ± 38	123 ± 4	480 ± 47	830 ± 110
	Firmly Adherent	80 ± 5	154 ± 16	16 ± 3	15 ± 2	29 ± 8	116 ± 51
	Loosely Adherent	109 ± 12	120 ± 38	154 ± 39	108 ± 5	447 ± 47	714 ± 109
	n	6	6	7	6	5 (8 firm)	11

Figure 2.24: Thickness of mucus layers of different regions in the small intestine. From [85].

previous research on preservation solutions used for small intestine tissues, aiming to enhance the preservation quality of ex vivo porcine small intestine samples.

A. Roskott et al. published a review addressing the challenges of small bowel preservation in transplantation, highlighting the sensitivity of the intestine to ischemia and the need for specialized preservation solutions [86]. The University of Wisconsin (UW) solution (standard in kidney and liver transplants) is suboptimal for the intestine. Instead, newer extracellular solutions and tailored luminal preservation strategies are recommended. Effective intestinal preservation requires solutions that prevent edema and maintain pH balance while protecting the mucosal barrier from ischemic injury.

Y. Chen et al. provided a general review of the development of preservation solutions (e.g. Collins Solution, UW, Histidin-Tryptophan-Ketoglutarat Solution) for kidney transplantation and cold storage techniques [87]. Low-temperature solutions are essential for tissue transplantation as they slow down cellular metabolism, which reduces the need for oxygen and nutrients, extending tissue viability. Cooling also slows enzymatic processes, minimizing tissue degradation, while inhibiting microbial growth and reducing oxidative stress. Together, these factors protect the tissue from

damage and prolong its functionality, making it viable for a longer period during storage and transport. This can also provide valuable insights for the preservation of small intestine tissues.

A. Petrenko et al. discussed advancements in organ preservation, emphasizing dynamic intervention methods, especially the use of organ perfusion [88]. Key topics include cellular and molecular events related to ischemia and reperfusion injury, enhanced preservation solutions, and protocols for machine perfusion, which mitigate ischemic damage and improve graft quality. The study identifies specific biochemical approaches that reduce organ injury during cold storage and note innovations like gas mediators (e.g., H_2S, CO, NO) for protecting organ vasculature.

2.2.2.6 Discussion

This section discusses how the structure and dynamic environment of the small intestine influence capsule robot locomotion. The folded architecture of the intestinal wall, comprising circular folds, villi, and microvilli, offers a complex, non-uniform surface that complicates passive capsule transport. While these structures enhance digestion and absorption, they also induce unpredictable capsule trajectories, such as uncontrolled spiralling. The unintended movement can negatively impact image acquisition, potentially compromising the quality and completeness of gastrointestinal diagnostics. Therefore, analysing and mitigating such undesired movement is essential.

Peristalsis is the primary driving force for passive capsule robots. However, due to the lumen's variable diameter, especially the proximal section where it often exceeds capsule size, non-constrictive flow may occur, reducing mechanical coupling and altering expected movement patterns. Furthermore, contact conditions between the capsule and tissue (e.g., open or enveloped) are critical and remain underexplored. Figure 2.6 illustrates these interaction scenarios. In the distal ileum, where the lumen narrows to approximately 1.8 cm which might increases the capsule retention risk [74], especially in patients with motility disorders. Understanding and controlling frictional behaviour is thus crucial for safety and patient outcomes.

While previous studies have characterized the mechanical properties of healthy small intestinal tissue, they offer limited insight into pathological conditions. Tissue

abnormalities, such as altered mucus secretion, mucosal damage, or lesion-induced deformation, can significantly alter tribological interactions. Additionally, most experimental models exclude the presence of mucus, which plays a non-negligible role in modulating friction. This gap underlines the need for more realistic test environments that incorporate physiological fluids and disease-mimicking tissue conditions.

2.2.3 Biomechanics of soft tissue

The mechanical behaviour of soft tissues, particularly connective tissues such as intestinal tissue, has been a focal point in biomechanical research due to their complex structural and material properties. Soft tissues exhibit anisotropic behaviour, stemming from the orientation of collagen fibers, which exhibit preferred directions [89]. These fibers not only dictate the material strength but also contribute to the nonlinear and strain-rate-dependent characteristics observed in soft tissues.

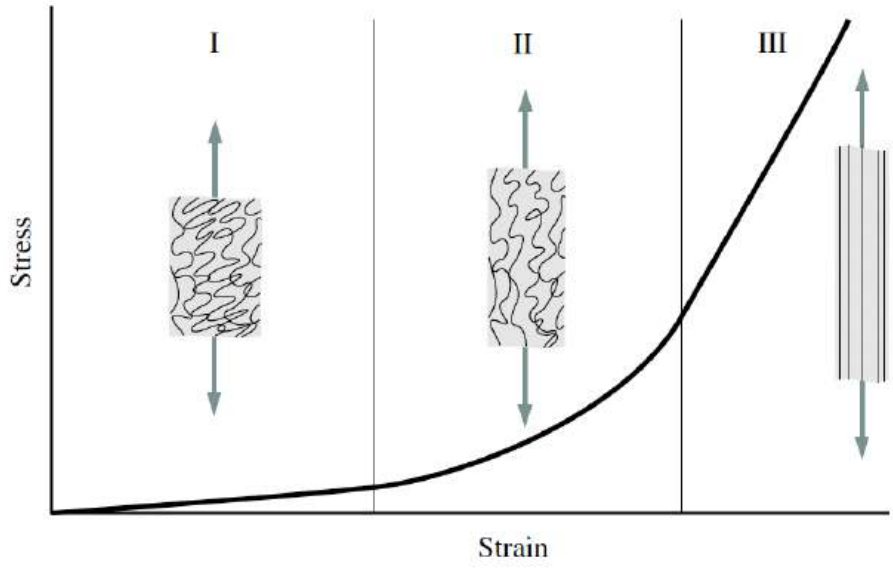

Figure 2.25: A schematic illustration of a representative stress-strain curve for soft tissue, depicting the corresponding morphology of collagen fibers. From [90].

The stress-strain response of soft tissues differs significantly from that of hard tissues, exhibiting distinct phases of deformation that provide insights into their functional adaptations, as shown in Figure 2.25. In the first phase, the initial deformation phase, collagen fibres appear wavy and crimped, allowing the tissue to behave isotropically. This aligns with observations that soft tissues can undergo large deformations

without immediate fibre elongation. The low stress required for initial deformation results in a soft, rubber-like behaviour, primarily driven by elastin fibres [90]. As loading increases, a transition occurs where collagen fibres begin to elongate, demonstrating a gradual uncrimping that enhances the tissue's load-bearing capacity [91]. This behaviour underscores the viscoelastic nature of soft tissues, where the interaction between collagen and the surrounding proteoglycan matrix is crucial for stress distribution and energy absorption. In the third phase, at high tensile stresses, collagen fibres straighten and align with the direction of the load, leading to increased stiffness. The stress-strain relationship becomes linear again, indicating a change in mechanical behaviour as the ultimate tensile strength is approached, resulting in fibre rupture [90].

It is important to note that the mechanical properties of soft tissues are influenced by various factors, including topography, age, species, and environmental conditions (temperature, osmotic pressure, pH). This variability complicates the determination of specific material properties, as experimental data derived from in vivo or in vitro testing can yield differing results [90].

2.2.3.1 Characterization of mechanical and tribological properties of soft tissues

There is not a very accurate method to measure the mechanical properties of the small intestine ex-vivo because the tissue has already degraded to some degree. In addition, due to the high viscoelasticity of this soft tissue, the values of stress or strain would vary in an extensive range in different conditions and from different individuals. Consequently, only a limited number of studies focus on this aspect. The following are some findings from the literature.

A. B. Lyle et al. performed tests to determine the COF of different regions of the porcine small intestine [92]. The intestinal tissue was placed in a designed environmental chamber to control the temperature and humidity to approximate the in vivo conditions. Besides, the edge effect and the unnecessary strain applied onto the tissue are minimized in every effort to achieve a normalized result of COF that obeys the first law of friction. The results reveal that the COF varied from 0.0004 (stainless steel) to 0.018 (micro-patterned polydimethylsiloxane). The report also concludes that the material, contact area and the physical quantities of the tissue

(temperature, humidity) can affect friction, compared with the previous study [93].

Y. Kim et al. used a confocal laser scanning microscope to measure the surface roughness of the porcine small intestine [64]. The small intestinal tissue was fixed by a chemical and coated with platinum, and the final result of the experiment is that the average surface roughness is 150 μm.

Tensile tests were conducted to determine the maximum stress and failure strain of the small intestine by V. I. Egorov et al. [94]. The intestine was cut in longitudinal and transversal directions. The measured results of maximum stress and failure strain for the small bowel in the transversal direction are about 0.9 MPa and 1.4, respectively, and in the axial direction are about 2.5 MPa and 1.5, as shown in Figure 2.26. The reason for the inflexion points in the curve was also explained in the report by observing the tissue slices. At point 1, all four layers of the small intestine are still engaged, but the irregularities of the serosa and internal muscular layers were able to be observed. The serosa and both the longitudinal and circular muscle layers were ruptured at point 2. Submucosa and mucosa were ruptured at points 4 and 5.

Tensile tests on different layers of the oesophagus were carried out by C.X. Lin [49]. Even though the oesophagus and the small intestine characteristics are not exactly the same, they are highly similar, which means the results have reference values. The results showed that the tensile strength of the mucosa was always more substantial than the muscle layer and the tensile properties in different locations are different. Although there is no ISO standard for testing soft tissues, M. Scholze et al. developed a cutting plate designed to easily shape tissues into a dog-bone configuration, offering valuable insights for handling intestinal tissue samples [95]. To avoid being affected by the implemented procedure, B. Innocenti et al. generated a non-contact automatic protocol to determine the uniaxial tensile tests of soft tissues [96]. The method involves drawing markers onto the specimen and using a camera to record the displacement changes which was verified as a high repeatability, independent by the operator and accuracy. B. Johnson et al. conducted uniaxial tensile tests on human and porcine intestines at various loading rates and found no significant strain rate dependency in the human specimens, noting only a slight stiffness increase between 50%/s and 500%/s. In contrast, the porcine intestine demonstrated a substantial strain rate effect, with stiffness more than doubling from 25%/s to 500%/s, indicat-

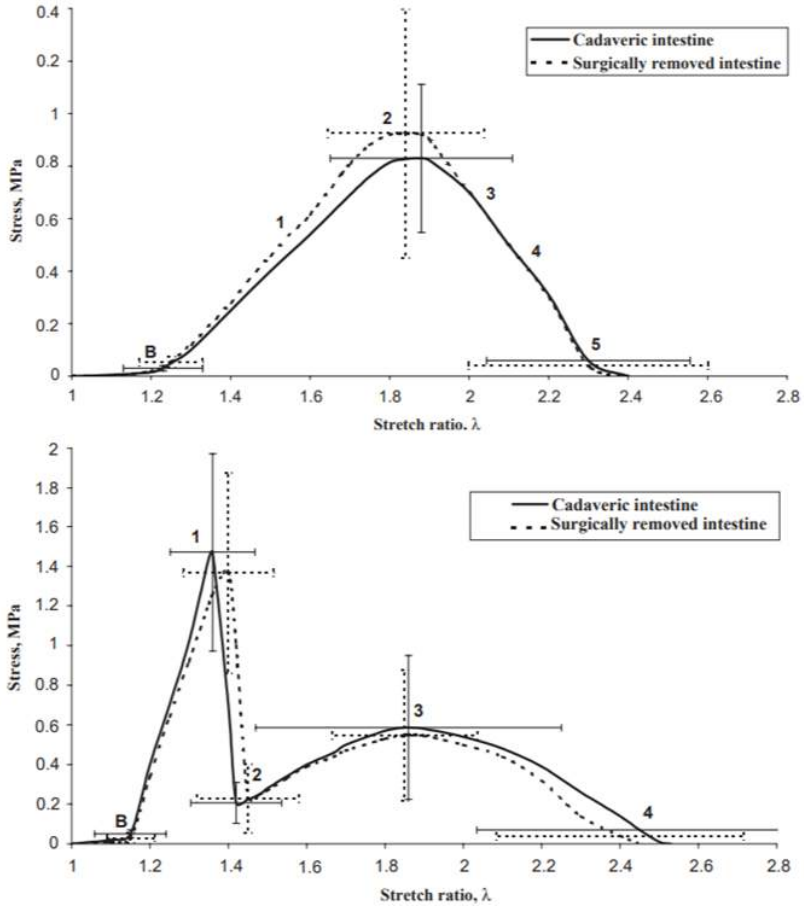

Figure 2.26: Tensile tests of small bowel in the transverse (up) and axial direction (low). From [94].

ing that higher strain rates result in a response of increased stress [97].

M. Griffin et al. developed a protocol to simplify the evaluation of human soft tissue mechanical properties, enabling non-destructive comparisons between native and synthetic tissues [98]. Their approach utilized a mechanical testing machine programmed to perform compression and tensile tests, with the testing methods described in detail. In a related study, Zahra's thesis focused on characterizing the mechanical properties of the large intestine [99]. Using a custom-designed indentation machine, this work explored the effects of preconditioning, strain rate, and stress relaxation, offering valuable insights into the testing of small intestinal tissues.

2.2.3.2 Modelling of intestinal tissue

Modelling tissue behaviour through mathematical expressions to predict elastic and viscoelastic properties is crucial and complements the experimental data derived from soft tissues. A mechanical test of the material is required to obtain experimental data for fitting the chosen viscoelastic model [46]. Several methods can be employed to achieve this such as compression, tension or shear tests. The relaxation modulus of constitutive equations for viscoelastic materials can be expressed using a Prony series [100], as outlined below:

$$E(t) = E_0 + \sum_{i=1}^{n} E_i e^{-\frac{t \cdot E_i}{\eta_i}} \tag{2.1}$$

where E_0, E_i and η_i represents the stiffness of the isolated spring, the elastic modulus of the spring, and the viscous coefficient of the dashpot in each Maxwell spring-dashpot arm. This equation captures the relaxation characteristics of the generalized Maxwell-Wiechert model, which consists of springs and dashpots operating under creep conditions. From the results of previous literature, the five-element, Double Maxwell-arm Wiechert model was always chosen to represent the viscoelastic model of small intestinal tissue for its high accuracy as shown in Figure 2.27 [38, 41, 45, 101]. Thus, the model is established as:

$$E(t) = E_0 + E_1 e^{-\frac{t \cdot E_1}{\eta_1}} + E_2 e^{-\frac{t \cdot E_2}{\eta_2}} \tag{2.2}$$

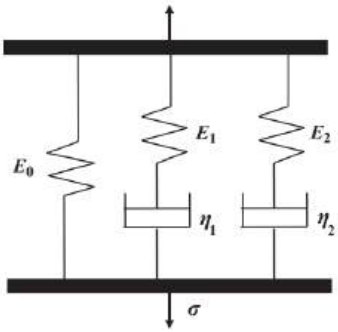

Figure 2.27: The five-element DMW viscoelastic model. Adapted from [46].

Also, during the relaxation tests, the strain ε_0 remains unchanged, so that the stress-time relationship of intestinal tissue can be expressed as:

$$\sigma(t) = \varepsilon_0 \left[E_0 + E_1 \exp\left(-\frac{t \cdot E_1}{\eta_1} \right) + E_2 \exp\left(-\frac{t \cdot E_2}{\eta_2} \right) \right] \tag{2.3}$$

2.2.3.3 Preconditioning effect

For soft tissue, the purpose of preconditioning is to establish a consistent and reproducible mechanical response, facilitating the measurement of material properties that closely reflect in vivo conditions. Generally, preconditioning through cyclic loading and unloading procedures is performed before the main tests to minimize experimental variability and to release the residual stress [102].

In Ebrahimi et al.'s study, strain level, cycle count, and the number of preconditioning repetitions were identified as poorly understood factors affecting the repeatability of tensile stress-relaxation tests in knee ligaments [103]. Their findings suggest that if a repeatable peak-to-equilibrium stress ratio is desired, applying higher strain levels and more preconditioning repetitions is recommended.

Using a Dynamic Mechanical Analyzer (DMA) for preconditioning tests at a specified rate and peak load [104], Liu et al. observed that stress relaxation response was consistent at lower strains (5% and 10%). However, at 15% strain, the swine skin exhibited rapid relaxation initially, with the decay rate subsequently slowing and stabilizing to levels observed at the lower strains.

Preconditioning strain levels can significantly influence measured tissue properties, as shown in research by S. Cheng et al. on spinal cord tissues [105]. Their results indicate that specimens preconditioned at lower strain levels exhibited a significantly stiffer stress-strain response, prompting a recommendation to use the highest strain level intended for the study to ensure reliable outcomes.

G. Bianco et al. developed a systematic approach to comparing two widely used preconditioning protocols [106]. In their study, tree shrew scleras underwent preconditioning through either 20 continuous loading-unloading cycles without rest or 5 cycles with a 15-minute rest between each. Their findings revealed notable differences in tissue response depending on the protocol used. Continuous cycling yielded more data points and minimized uncertainty in repeatability, whereas protocols with rest intervals reduced the required cycle count but increased the time needed to reach a preconditioned state.

Despite these insights, there is limited information on the effect of preconditioning on the mechanical properties of the small intestine, such as the number of cycles required to reach a stable response. Thus, further investigation is needed to understand how preconditioning influences the viscoelastic properties of small intestinal tissue.

2.2.3.4 Discussion

The mechanical properties of soft tissues, especially connective structures like intestinal tissue, are governed by a complex interplay of collagen fibres, the proteoglycan matrix, and other molecular components. Research consistently demonstrates that the anisotropic and viscoelastic behaviour of these tissues primarily results from the orientation and mechanical response of collagen fibres under load. Study by Holzapfel et al. underscores that this fibre alignment critically influences mechanical strength, adaptability, and failure behaviour during strain, as reflected in distinctive stress-strain curves from tensile testing [90].

In addition to intrinsic tissue structure, external conditions significantly affect mechanical measurements. For example, friction coefficient studies by Lyle et al. reveal that factors like humidity and temperature can markedly alter test results [92]. This variability highlights the necessity of rigorously controlled experimental environments, particularly in ex vivo tests, to obtain data that more closely represent in vivo behaviour.

To interpret these mechanical responses, viscoelastic models such as the Double Maxwell-arm Wiechert model have been widely adopted. These frameworks, along with tools like the Prony series to model time-dependent modulus changes, offer predictive insights into tissue relaxation and deformation under sustained loads. However, despite their utility, current models face limitations in replicating the full complexity of in vivo conditions, where multiple interacting factors influence tissue behaviour.

Preconditioning protocols, used to achieve consistent tissue response before primary testing, also vary widely across studies. Evidence from research on other soft tissues, including knee ligaments and spinal cords, shows that outcomes are sensitive to variables such as strain magnitude, cycle number, and loading rate. These findings

suggest that intestinal tissue, with its unique viscoelasticity, requires customized preconditioning protocols. Yet, the literature remains sparse on optimal parameters for the specific intestinal tissue type. Advancing this area could improve experimental reproducibility and support better integration with viscoelastic models.

In summary, while notable progress has been made in the biomechanical characterization of intestinal tissue, further refinement of experimental methods and model validation under diverse physiological conditions is essential. Addressing these challenges will enhance our understanding of tissue mechanics and support the development of more accurate predictive tools for CE applications.

2.3 Conclusions

This review highlights the necessity for multidisciplinary collaboration across biomechanics, tribology and capsule endoscopy to address the identified research gaps. This chapter has summarized the principal unresolved issues emerging from the preceding discussions and proposed strategic directions for future research to overcome these limitations.

- Lack of realistic ex-vivo testing environments: Many existing studies rely on simplified testing platforms that do not fully replicate the biological and mechanical conditions of the human GI tract. While porcine small intestine tissue is commonly used as a substitute, lack of thorough understanding of the viscoelasticity, tissue preservation method, and the absence of physiological responses introduce significant discrepancies from in vivo conditions. Moreover, most experimental setups use rigid or overly simplified substrates that fail to simulate the soft, deformable contact environment encountered in the abdominal cavity.

- Unstandardized preconditioning protocols for tissue testing: Current literature lacks consistency in preconditioning protocols for intestinal tissue, which affects repeatability and comparability of mechanical measurements. Variations in cycle count and strain rate across studies lead to inconsistent viscoelastic responses.

- Inadequate consideration of mucus and lubrication effects: Although mucus plays a crucial role in frictional interaction within the GI tract, it is largely

neglected in experimental protocols and mechanical models. Most tribological assessments focus solely on very low hydrated contact or use saline as a lubricant, which does not adequately reflect the rheological properties of actual intestinal mucus.

- Lack of identification of the underlying causes of capsule retention scenarios and the development of effective strategies to address issues related to excessive capsule speed.

Based on the identified research gaps and the associated tribological challenges, the aim and objectives of this study were formulated and are presented in Chapter 1.

Chapter 3

Mechanical property testing of intestinal tissues

3.1 Introduction

The frictional behaviour of intestinal tissues is primarily governed by their intrinsic mechanical properties, including compliance, viscoelasticity, and surface morphology. Due to their low elastic modulus, soft tissues undergo significant deformation under applied normal loads, resulting in an increased real contact area, elevating the friction resistance relative to stiffer materials. Viscoelasticity further contributes to energy dissipation during sliding. Tissues exhibiting time-dependent deformation characteristics (creep, stress relaxation) resist motion not only through elastic recovery but also via internal friction, which converts mechanical work into heat. The magnitude of this dissipation correlates with tissue stiffness and strain-rate sensitivity. In the context of capsule endoscopy, such viscoelastic losses increase drag during locomotion through the gastrointestinal tract. Surface microstructural features also affect frictional dynamics. Topological elements such as villi, folds, and aligned collagen fibres introduce anisotropic frictional properties, where the COF may vary with sliding direction due to orientation-dependent mechanical impedance. These structural details modulate interfacial mechanics and must be accounted for in tribological modelling.

Mechanical characterization of small intestinal tissue is essential for developing accurate ex vivo models. It enables the analysis of viscoelasticity involves tissue deformation and stress response over time, thereby improving the understanding the scenarios of frictional behaviours and contributing to the investigation of potential causes of capsule retention. Using a rigid support beneath the tissue introduces non-physiological constraints and alters load distribution. Therefore, to simulate in vivo

conditions, a compliant substrate with mechanical properties analogous to intestinal tissue should be employed to obtain more realistic frictional simulation. Quantitative analysis of stress-strain responses, surface profiles, and wall thickness can inform the design of synthetic substrates.

In this study, porcine small intestine, chosen for its anatomical and mechanical similarity to human tissue, was subjected to compression testing using an Imada force-displacement system. Stress-strain data were obtained through cyclic loading protocols to evaluate preconditioning effects, strain-rate dependence, and stress relaxation. Surface profilometry and dimensional metrics (thickness, texture) were also recorded. These datasets support both biomechanical understanding and the development of biomimetic experimental platforms, offering potential alternatives to fresh tissue by enabling synthetic replication of key functional properties.

3.2 Sample preparation

This section describes the procedures for obtaining and subsequently processing small intestine tissue. Since these steps remain the same for each experiment, the process is detailed here separately and will not be repeated in subsequent sections.

3.2.1 Tissue preparation

The small intestine, being the longest and most intricate section of the gastrointestinal tract, is crucial for evaluation during capsule endoscopy. As learned from the previous literature, the small intestine of a pig is chosen as a substitute for the human intestine due to its anatomical and physiological similarities to the human small intestine in terms of size, shape, and surface structures [68, 69]. Porcine intestines, excised from approximately 6 months old pigs, were obtained within 1-2 hours of slaughter directly from a local abattoir (Bramall N & Son, Sheffield). Different preservation solutions were considered, such as Collins solution and The University of Wisconsin (UW) solution which are considered optimal preservation solutions and are used in organ transplantation. However, their high cost was found to be prohibitive for these experiments. Therefore, phosphate buffered saline (PBS) was used which offered good preservation at a lower cost and had the advantage of being much easier to make. Following the cold storage method to minimize the deterioration, intestines were immersed in 4°C PBS solution and were stored in sterile plastic bags immediately after its excision from the slaughtered pigs and transported in an insulated container. This

procedure was used to maintain their hydration and integrity, suppress microbial action and slower the process of degradation.

After getting back to the lab, the intestines were transferred into the tray (Figure 3.1a). Unlike human intestines, which have distinct characteristics for identifying the duodenum, jejunum, and ileum, porcine intestines lack such clear differences. Additionally, the limited understanding of porcine small intestine biology among experimenters further complicates the differentiation of its various sections. Thus, tissue samples were selected from the middle 2-3 meters of every intestinal tract (Figure 3.1b). Another factor influencing the selection of tissue samples was the attachment of the mesentery to certain sections of the intestines. The mesentery is a continuous set of tissues that attaches the intestines to the abdominal wall, helping to hold them in place while also providing a conduit for blood vessels, nerves, and lymphatics that supply the intestines as shown in Figure 3.1c [107]. However, as the research focuses on the small intestine, the presence of mesentery could increase tissue thickness and alter results significantly. Therefore, only samples without mesentery were used in the experiments (Figure 3.1d). Samples were cut using scalpels along the axis of the intestine into rectangular sections (Around 10 cm in length). The samples were subsequently immersed in PBS solution, with their edges gently pinched and agitated to remove surface residues, ensuring that the mucosal layer remained intact (Figure 3.1e). This outer layer is critical for preserving the biological structure, particularly in frictional interactions and mechanical property assessments. It was observed that when intestinal tissue was exposed to unconditioned air, it lost moisture and became dry. To prevent this, tissues were preserved in PBS solution while awaiting experiments (Figure 3.1f). Furthermore, the entire tissue preparation and testing process was completed as quickly as possible, within 5–7 hours of slaughter, in line with recommendations from previous literature.

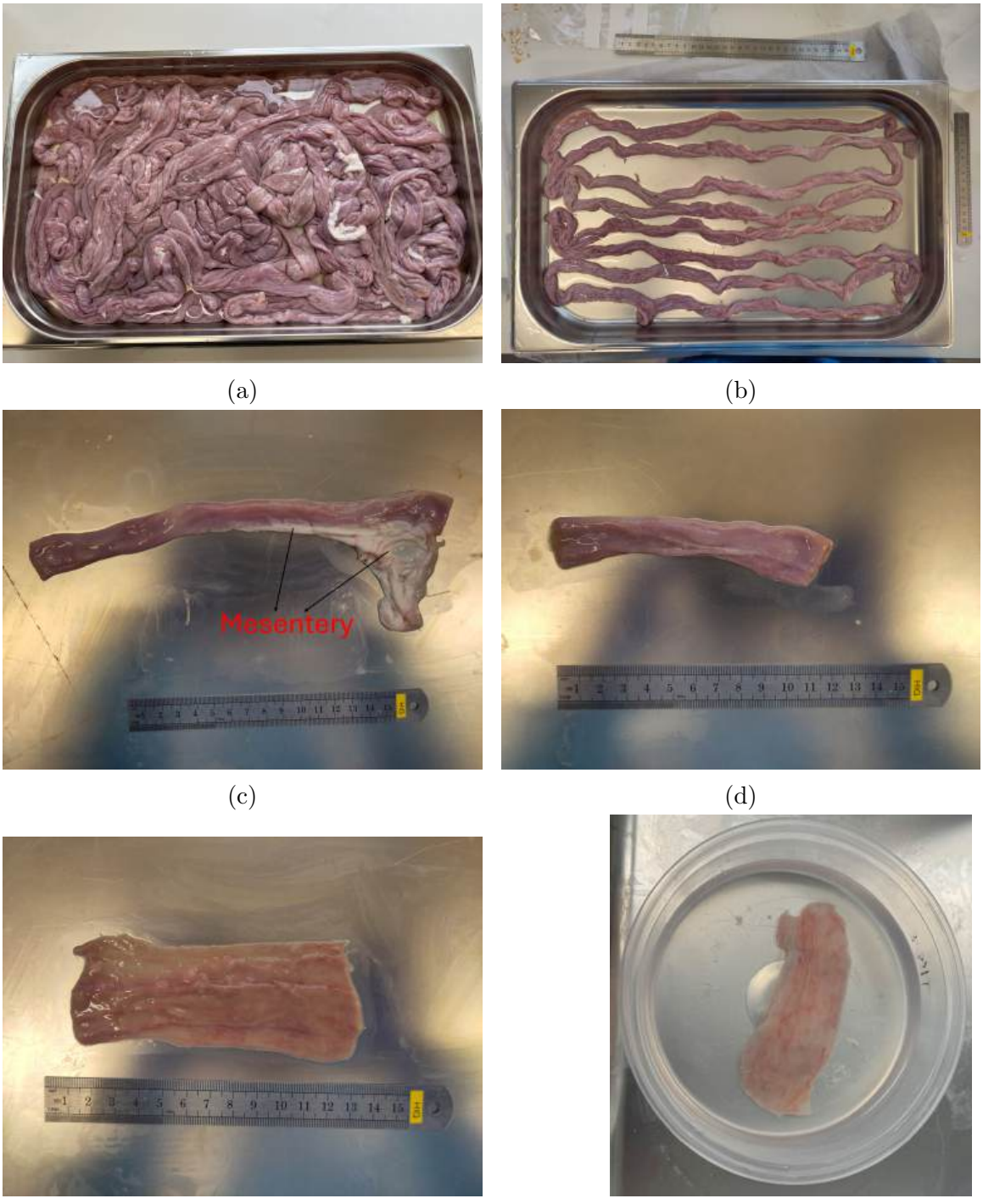

(a) (b)

(c) (d)

(e) (f)

Figure 3.1: Photos of the intestine dissection process include: (a) One entire porcine small intestine; (b) A middle 2-3 meter section of the porcine intestine; (c) A sample with mesentery attached; (d) A selected sample without mesentery; (e) The intestine cut open into a rectangular shape; (f) Tissue preserved in PBS solution to prevent drying

3.2.2 SynDaver synthetic tissue

During the search for appropriate sources of small intestine, a synthetic intestinal model developed by SynDaver was identified, as illustrated in Figure 3.2. According to the manufacturer's description, this synthetic product was developed based on comprehensive physical testing of living tissue and is claimed to replicate key mechanical properties. Given this, it was deemed more practical to first verify the experimental method on the synthetic tissue prior to conducting tests on animal tissue. This approach offered the advantage of eliminating time constraints typically associated with animal testing. Furthermore, a comparative evaluation was conducted to assess whether the mechanical properties of the synthetic bowel model are consistent with those of real intestinal tissue, in order to determine its potential as a viable substitute for animal tissue in experimental settings.

The synthetic intestine was shipped in a sealed container filled with a preservation solution. Upon arrival, it was transferred, along with the preservation solution, into a plastic cup and stored in a refrigerator. When needed for experimentation, it was prepared similarly to the animal tissue by being cut open into a rectangular shape. It can be seen from the cut edges that the synthetic tissue was made of a variety of fibres (though specific materials are not disclosed), along with water, different salts and organic compounds.

Figure 3.2: A 12-inch synthetic double-layer bowel model from SynDaver was used for experimentation.

3.3 Mechanical properties characterization of intestinal tissues

The mechanical and viscoelastic properties of tissues can be characterized by applying a mechanical load and observing the time-dependent stress decay when a constant strain is maintained over short or extended periods [103, 108–111]. Indentation is a widely used technique for probing the mechanical properties of soft material such as biological tissues. Compared to tension or compression tests, indentation is ultra-local and less invasive, with the indenter being pressed into the surface of the sample. Given the volume comparison between capsule robots and intestines, indentation tests were deemed more appropriate for this study. The experiments included measuring the general properties of intestinal tissue, studying the preconditioning effect, and testing the strain rate effect on tissue response. As porcine intestines are the primary focus of this study, the results and discussion will primarily address them, with synthetic tissues used to supplement the data and highlight material property differences.

3.3.1 Instrument

3.3.1.1 Tissue holder

The tissue holder, as shown in Figure 3.3, is a specialized device designed for securely fixing tissue samples during mechanical property testing and also later friction testing. Its structural design consists of three primary components: a frame fabricated via 3D printing using PETG, along with a rigid substrate and a baseplate, both machined from acrylic (compressive modulus: 2.70 - 3.30 GPa [112]). The following features ensure its functionality and precision during testing:

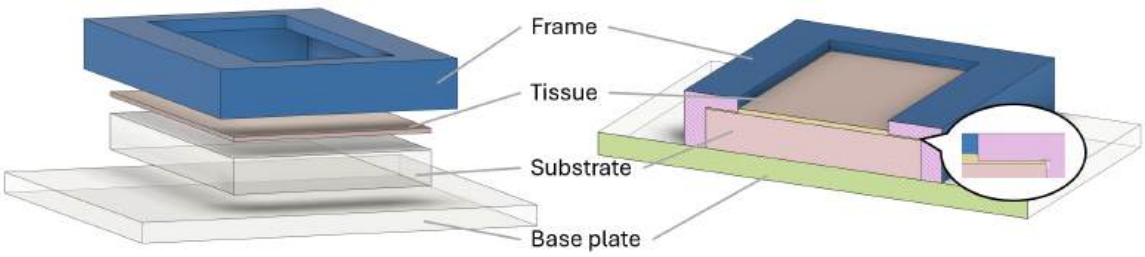

Figure 3.3: Illustration of the tissue holder: Schematic drawing of the tissue holder in an exploded view and a sectional view.

1. **Dual-Layer Construction**
   The lower layer consists of a rigid plastic substrate with a modulus significantly higher than that of the intestinal tissue. Due to the significant difference in compressive modulus between the acrylic substrate and the intestinal tissue, as well as the limited number of indentation cycles applied, and a strain level of 0.5 was clarified as being within the non-destructive range based on visual observation, it can be inferred that the mechanical test results predominantly reflect the intrinsic properties of the intestinal tissue, with minimal influence from the underlying substrate.

2. **Clamping Mechanism**
   The gap between the inner frame and the inner substrate is precisely set at 0.3 mm, slightly smaller than the typical thickness of the intestinal tissue (test results for the thickness of the intestines are addressed later). This deliberate design allows the tissue boundaries to be securely clamped without tearing or slipping. Additionally, the inner area of the frame is dimensionally smaller than the tissue sample to exert uniform clamping pressure along all the boundaries, ensuring stability and preventing unwanted movements during testing.

3. **Liquid Containment Design**
   The upper and lower surfaces of the frame incorporate recessed areas akin to a "bathtub", which enable the holder to retain PBS or other test liquids. As the tissue would have drying problem during the test that could affect the results, this feature is essential for maintaining the tissue's hydration and physiological properties throughout the testing process. The clamped gap effectively seals the liquid inside, preventing leakage and ensuring consistent immersion of the tissue as shown in Figure 3.4a.

This tissue holder, with its clamping and sealing mechanisms, is designed for performing reliable and reproducible mechanical property tests on intestinal tissues, making it a vital tool for biomechanical research. The porcine and synthetic tissues were prepared and set up as illustrated in Figure 3.4. The frame is secured to the baseplate using bolts, and the scale on the frame aids in precisely locating the compression spot.

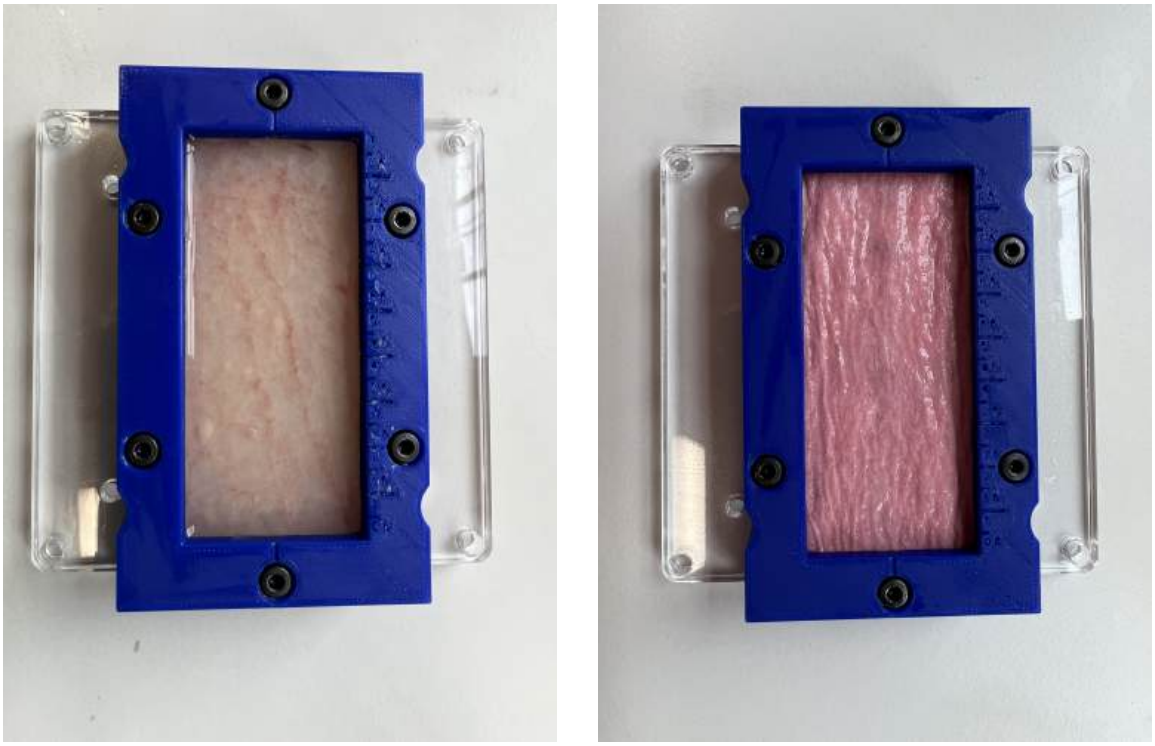

(a) (b)

Figure 3.4: Photos of tissue set in tissue holder with PBS: (a) Porcine tissue; (b) Synthetic tissue.

3.3.1.2 IMADA force-displacement testbed

The ZTA-500N IMADA Force Gauge is a high-functionality digital force gauge designed for precise compression and mechanical property testing (Imada Inc., Japan). It offers high-speed sampling rate (1000 Hz), ensuring accurate and reproducible measurements, with a maximum capacity of 500 N and a resolution of 0.1 N and 0.001 mm. A 15 mm diameter, flat-ended, disk-like tip was used to ensure a consistent contact profile between the tissue and the probe, simplifying theoretical analysis by enabling straightforward calculation of the contact area. Combined with the IMADA FA test stand, the force gauge was mounted on a slideway, allowing controlled vertical movement and the indentation probe was securely attached to the force gauge. The probe was carefully aligned to the wanted position, ensuring it was centered and perpendicular to the tissue to achieve accurate and consistent measurements.

This setup incorporates features such as contact detection, force limit, displacement limit, and cyclic loading, making it highly adaptable to experimental requirements. Additionally, tissue holders and other devices can be seamlessly integrated,

and the straightforward setup and operation allow for easy adjustment of variables such as loading speed. Equipped with an OLED display, the device provides clear, customizable data visualization and the included software allows for real-time data logging, graphing, and analysis, making it ideal for applications such as assessing the mechanical properties of biological tissues. The complete testbed, including the tissue sample and tissue holder, is illustrated in Figure 3.5.

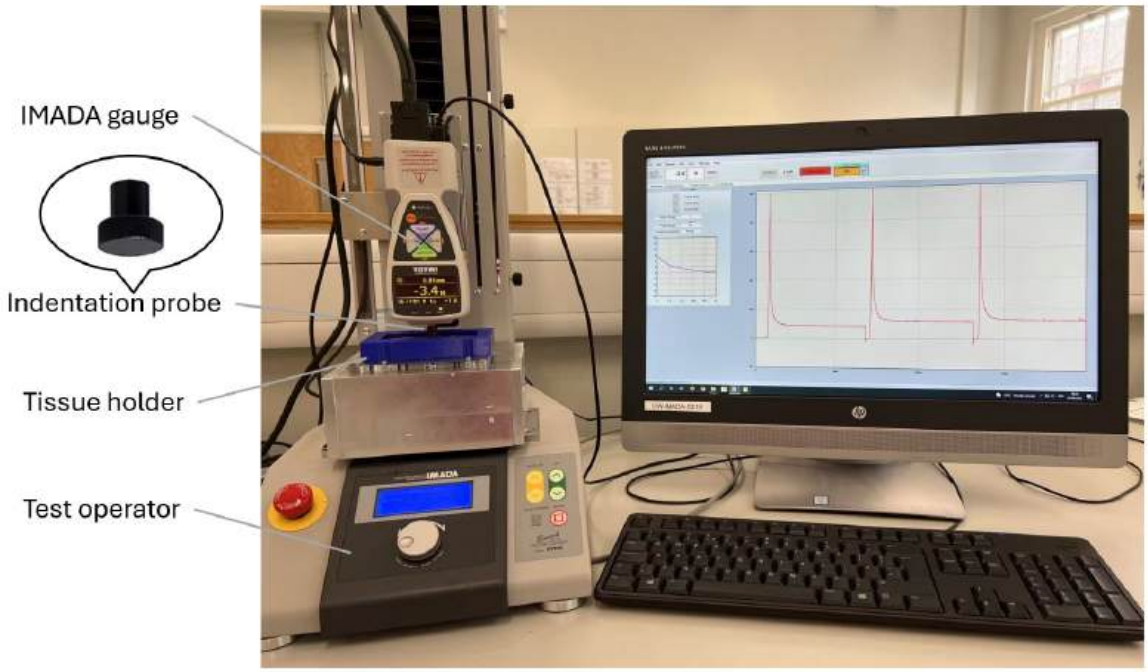

Figure 3.5: Testbed for conducting indentation tests on intestinal tissue.

3.3.2 Thickness measurement

Establishing a reliable procedure for measuring tissue thickness at various sample locations is essential. On the one hand, it provides fundamental data on the thickness of the small intestine. On the other hand, this method is also required for calculating strain changes during the indentation test. Accurate tissue thickness measurement ensures the reliability of the experimental results.

3.3.2.1 Methodology

A digital caliper was initially used to measure the tissue thickness. However, due to the soft and pliable nature of intestinal tissue, this approach proved unsuitable. Relying on hand-eye coordination to determine if the caliper jaws were in contact with the tissue introduced significant uncertainty, making it impossible to accurately measure

the uncompressed thickness. To overcome the limitations of the caliper, a device consists of a displacement gauge mounted on a height-adjustable stand, equipped with a pointed probe for precise contact with the tissue sample was employed as shown in Figure 3.6.

Figure 3.6: Device and setup for measuring tissue thickness.

The pointed tip minimizes the contact area, reducing the risk of uneasily recognized compression and enhancing measurement precision. The intestinal tissue is secured within the tissue holder, which ensures a stable and consistent position during the measurement process.The initial height was calibrated without tissue and set to zero. Subsequently, the height of the gauge was manually adjusted to bring the probe into proximity with the tissue surface. The contact point was determined visually, with the operator ensuring the probe barely made contact with the tissue without applying additional pressure. The displacement gauge reading at this precise moment was recorded as the tissue thickness. Seventy-five thickness measurements were per-

formed for both porcine tissue and synthetic tissue, with five samples measured at fifteen locations each.

3.3.2.2 Results

The results of the thickness of two types of tissue of seventy-five measurements are summarized in Table 3.1 and visualized in Figure 3.7. The descriptive statistics of tissue thickness measurements for porcine and synthetic intestines was analysed and summarized in Table 3.1. The porcine tissue thickness measurements ranged from 0.55 mm to 1.61 mm, with a mean value of 1.045 mm (± 0.2833 mm standard deviation). The synthetic intestine exhibited significantly narrower variability, with thickness values ranging from 1.18 mm to 1.52 mm, yielding a mean of 1.287 mm (± 0.0734 mm standard deviation). The synthetic model demonstrated a range of only 0.34 mm compared to 1.06 mm for the porcine tissue. This indicates a high level of uniformity in the synthetic intestine's structure compared to the natural variability inherent in biological tissues.

Figure 3.7 presents scatter plots for the thickness measurements of both tissue types and the horizontal lines in both scatter plots represent the mean thickness for each sample group. For the porcine intestine (Figure 3.7a), data points are widely dispersed due to its unique biological structure, particularly the presence of circular folds. The height of these folds significantly impacts the reading of the thickness. This disparity is reflected in the plot, where two distinct groups of data points emerge: one above and one below the mean thickness line, with relatively fewer points clustering around the mean. In contrast, the synthetic intestine (Figure 3.7b), exhibits tightly clustered data points, underscoring its structural uniformity.

Table 3.1: Descriptive statistics of tissue thickness measurements for porcine and synthetic intestines.

Tissue Type	**Porcine Intestine**	**Synthetic Intestine**
Number of values	75	75
Minimum (mm)	0.55	1.18
Maximum (mm)	1.61	1.52
Range (mm)	1.06	0.34
Mean (mm)	1.045	1.287
Std. Deviation (mm)	0.2833	0.0734
Std. Error of Mean (mm)	0.0325	0.0084

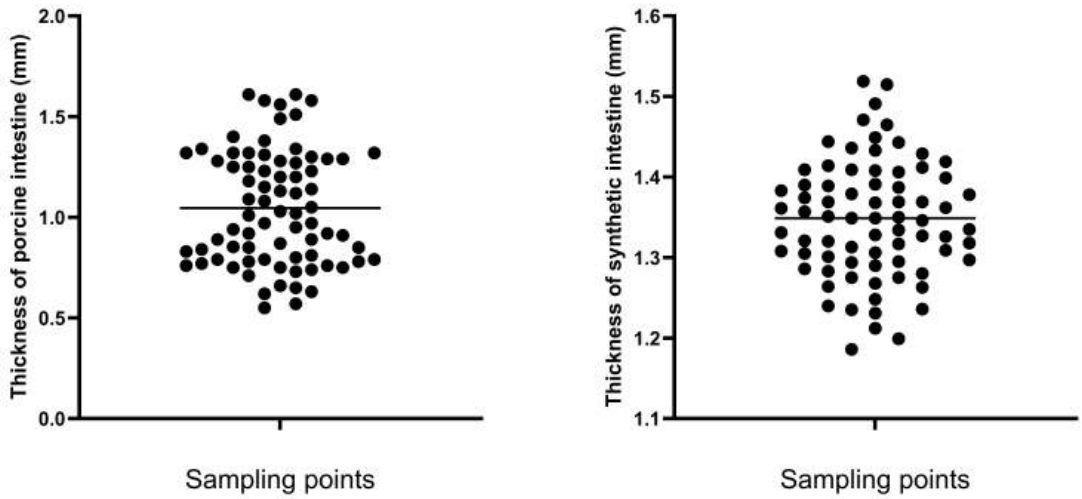

(a) (b)

Figure 3.7: Scatter plot of tissue thickness measurements ($n = 75$): (a) Porcine intestine; (b) SynDaver synthetic intestine. The horizontal line indicates the mean thickness.

3.3.2.3 Discussion

Comparing the results of the two tissue types, the more centralized data points observed in the synthetic intestine demonstrate its consistency, likely linked to its controlled manufacturing process, whereas the biological variability of the animal tissue accounts for the observed differences. Additionally, the mean thickness of the synthetic tissue is slightly thicker than that of the porcine intestine. Further analysis and discussions will be finished to determine whether these thickness differences translate to variations in mechanical behaviour or suitability for specific experimental setups. To enhance its physiological relevance, modifications such as reducing wall thickness, incorporating surface topography to mimic circular folds, and tuning the viscoelastic properties could be considered for future iterations of the synthetic model.

The observed variability in thickness measurements can be attributed to several factors. As discussed before, biological variability of the intestinal tissue is the main reason, including differences in compliance and surface irregularities, especially the presence of circular folds (about this part will be further studied in the surface measurement section), which contributed to measurement disparities across sampling points. Besides, operator dependence played a significant role, as determining the exact contact point between the probe and tissue relied on visual inspection and manual adjustments, introducing subjective bias and potential inconsistencies. Despite the improved precision of the pointed-probe displacement gauge over calipers, slight misalignments such as challenges in ensuring the probe was perfectly perpendicular to the tissue and vibrations could impact readings. These factors collectively underscore the inherent challenges in achieving highly precise tissue thickness measurements.

Overall, The displacement gauge with a pointed probe is a practical alternative to calipers for measuring the thickness of soft tissues like the intestine. However, to minimize the impact of human error and other potential sources of variability, it is recommended to take multiple readings at different locations and average the results. Automated or digital systems, if available, could further enhance reliability and repeatability.

3.3.3 Preconditioning test

Preconditioning is a crucial initial step in the mechanical characterization of intestinal tissue, as it determines the number of cycles required for the tissue to reach a steady state. Biological tissues often exhibit time-dependent mechanical responses that stabilize after repeated loading and unloading cycles. Preconditioning minimizes the influence of initial structural inconsistencies, such as residual stresses or viscoelastic effects, ensuring that the tissue achieves a consistent reference state. This process enhances the reliability and reproducibility of subsequent measurements, allowing for a more accurate characterization of the tissue's inherent properties. Therefore, examining the impact of preconditioning on the viscoelastic behaviour of the small intestine is particularly important.

3.3.3.1 Method

Indentation tests were performed using Imada force-displacement testers to assess the stress-strain relationship and confirm the cyclic loading response of the tissue. The tests were performed on three tissue samples. A continuous cyclic preconditioning method with stress control was adopted, inspired by findings from previous studies. In this approach, fifteen loading and unloading cycles were applied to the tissue, with each cycle reaching the same maximum stress, as shown in Figure 3.8a.

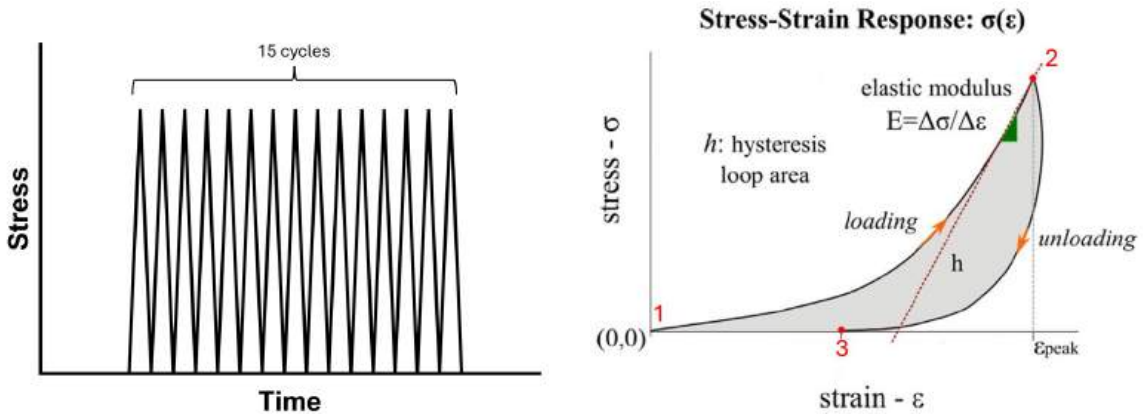

(a) (b)

Figure 3.8: (a) The stress control protocol that is used to examine the tissue responses under cyclic loading. (b) A typical stress-strain response during a loading-unloading cycle for soft biological tissue. From [106].

Each loading-unloading cycle followed the stress-strain response as depicted in Figure 3.8b, with distinct phases outlined below:

1. **Phase 0-1: Contact Detection**
   The probe was calibrated to the tissue surface, positioned approximately 1 cm above it. After activating the device, the probe was moved downward at a speed of 0.2 mm/min. Upon contact with the tissue, a resistance force of 0.1 N was registered, indicating that the probe had firmly engaged with the tissue surface. The probe was then lifted, and once the reading returned to 0, it was marked as the initial position, signalling the start of the cycle.

2. **Phase 1-2: Loading Phase**
   During this phase, the probe kept compressing tissue at a constant speed, increasing the applied strain until the desired stress was reached. The loading speed was set to 3 mm/min or 6 mm/min to replicate the different types of movement observed in the small intestine.

3. **Phase 2-3: Unloading Phase**
   After reaching the target stress, the probe was lifted back to the initial position at the same speed. Due to the viscoelasticity and time-dependent characteristics of the tissue, hysteresis would occur, resulting in a residual strain, which can be seen at point 3 in Figure 3.8b.

4. **Phase 3-1: Cycle Completion**
   The cycle was considered complete when the probe returned to its initial position. The process immediately repeated itself for the next cycle, continuing for a total of 15 cycles to ensure consistency in the data and achieve stabilization of the tissue's response.

The force and displacement data were recorded throughout the loading and unloading phases. These raw data were subsequently converted into engineering stress and strain values using the following equations:

$$\sigma = \frac{F}{A} = \frac{F}{\pi \times r^2} \tag{3.1}$$

where σ is the engineering stress, F is the normal load force, and A is the cross-sectional area of the round probe which can be computed from the radius r of the tip.

$$\varepsilon = \frac{\Delta L}{L_0} = \frac{v \times t}{L_0} \tag{3.2}$$

where ε is the engineering strain, ΔL is the recorded change in length which can be computed from the compression speed v and time t, and L_0 is the original thickness of the tissue.

Subsequently, the stress-strain curve was analysed to identify the linear region, which is typically represented by the red dashed line in Figure 3.8b. An iterative algorithm implemented in MATLAB (MathWorks) was used to computationally identify the linear region [99]. The algorithm evaluated the linearity (coefficient of determination or R^2) between the maximum stress point (point 2 in Figure 3.8b) and progressively adjusted start points until $R^2 > 0.97$. The Polyfit function in MATLAB was utilized for linear regression fitting. The slope of this fitted line was taken as the elastic modulus of the tissue, providing insights into its stiffness under the specified testing conditions.

3.3.3.2 Results

Figure 3.9 illustrates a representative depiction (first six cycles) of the variations observed in stress-strain response during the preconditioning process, subjected to two different loading speeds: 3 mm/min (Figure 3.9a) and 6 mm/min (Figure 3.9b). The entire fifteen cycles response is provided in appendix A. The stress-strain loops show a progressive decrease in the hysteresis loop area and an increase in the stiffness of the material with increasing cycles, signifying cyclic softening. Convergence of the curves is observed after 4 to 6 cycles, indicating the gradual stabilization of the tissue's mechanical response. As preconditioning continues, the strain curves exhibit a shift in the peak strain to higher values, consistent with the accumulation of residual strain observed in similar biological tissues [109, 111]. Additionally, at both strain rates, the tissue shows a J-shaped nonlinear hyperelastic response, with a clear distinction between the low-strain (initial linear) region, the intermediate nonlinear toe region, and the high-strain linear region.

The trends of linear modulus can also reveal the achievement of a steady-state preconditioned response. Table 3.2 presents the summary of linear modulus values at strain rates of 3 mm/min and 6 mm/min across fifteen preconditioning cycles and Figure 3.10 reflect the changes of linear modulus during continuos cyclic loading in a more distinctive way. At 3 mm/min, the linear modulus increases progressively from an initial value of 258.95 kN/m^2 in the first cycle to 541.84 kN/m^2 by the 15th cycle. Similarly, at 6 mm/min, the modulus starts at 431.99 kN/m^2 and increases to 598.12

kN/m^2. The observed trends indicate a stiffening effect due to preconditioning, with rapid changes occurring during the initial cycles, eventually stabilizing after the 6th cycle.

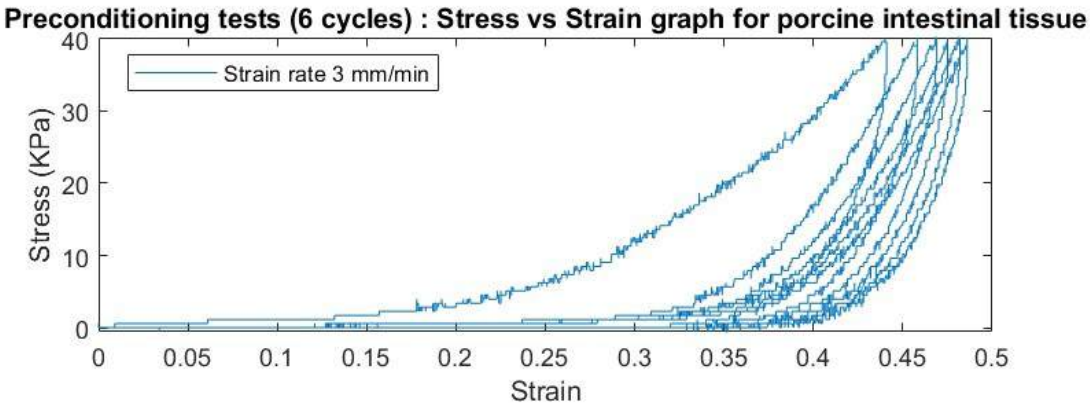

(a)

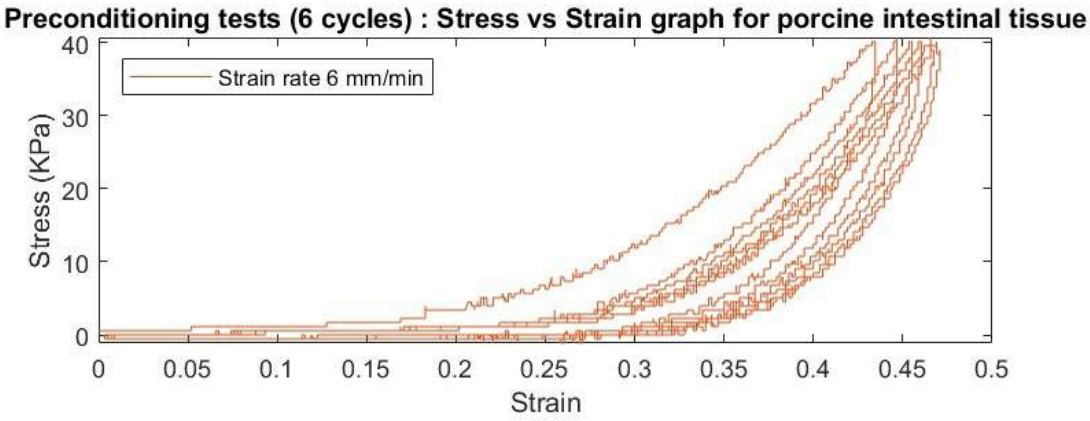

(b)

Figure 3.9: Stress-train response of the first 6 loading cycles of porcine intestinal tissue: (a) Loading speed of 3 mm/min; (b) Loading speed of 6 mm/min.

3.3.3.3 Discussion

The results clearly demonstrate that cyclic preconditioning effectively stabilizes the mechanical response of porcine intestinal tissue. The stress-strain behaviour converges after the 4-6th cycle, marking a steady-state response. This finding supports the efficacy of the preconditioning protocol in achieving mechanical repeatability.

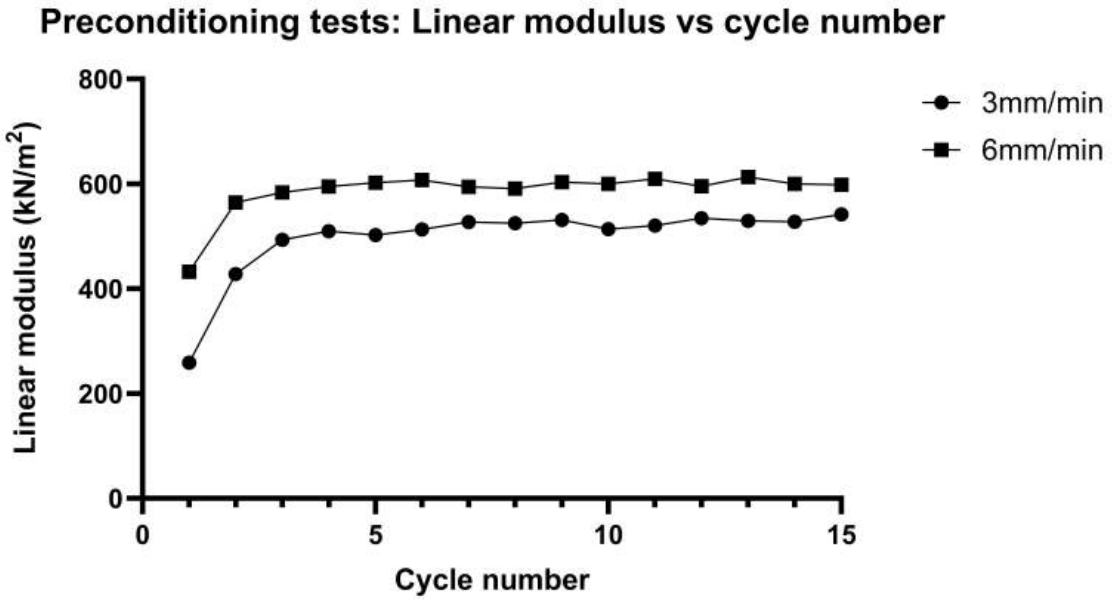

Figure 3.10: Scatter plots depicting the linear modulus from 15 repeated loading cycles conducted at loading rates of 3 mm/min and 6 mm/min.

Cycle number	Linear modulus (kN/m^2)	
	3 mm/min	6 mm/min
1	258.95	431.99
2	427.71	564.52
3	493.29	583.26
4	509.54	594.94
5	502.19	602.11
6	512.85	607.14
7	527.20	594.42
8	524.95	590.89
9	530.85	603.47
10	513.44	599.86
11	520.22	609.27
12	534.09	595.45
13	529.04	613.11
14	527.31	599.58
15	541.84	598.12

Table 3.2: Summary of linear modulus values at different speeds and cycle numbers

A significant advantage of the stress control method is that it allows for direct comparison of differences across cycles. A key observation from the data is the accumulation of residual strain, particularly pronounced during the initial cycles. The

tissue undergoes slight permanent deformation (not fully recovered during the unloading phase), observable as an increase in strain at the start of successive loading phases. As the tissue deforms under load, its internal molecular structures such as collagen and elastin fibers experience resistance, and some energy is spent overcoming this internal friction. When the load is removed, the tissue doesn't return all the stored energy because part of it was converted into heat. Simultaneously, the area of the hysteresis loop diminishes with each cycle and gradually remain unchanged, indicating reduced energy dissipation. This behaviour suggests that the tissue adapts to the imposed mechanical environment, transitioning to a more stable state over repeated loading cycles. These outcomes align with the literature, which emphasizes the importance of cyclic preconditioning in stabilizing the structural integrity of biological tissues under mechanical stress.

The effect of loading speed on tissue mechanics is evident in the observed differences between strain rates of 3 mm/min and 6 mm/min. The loading speeds significantly influence the initial slope of the stress-strain curve, with higher speeds resulting in a more rapid increase in stiffness. The detailed effects of loading speed were studied and will be presented in later sections.

Although the exact mechanisms of preconditioning remain incompletely understood, the observed trends are consistent with the literature. The gradual stiffening during cyclic loading is likely related to the alignment and recruitment of collagen fibers, as well as viscoelastic adaptations in the tissue matrix. These structural and compositional characteristics, influenced by species-specific fiber arrangements, contribute to the complex mechanical behaviour of biological tissues. However, as this part of study does not aim to explore these mechanisms in detail, further investigation would be necessary to elucidate their contributions. On the other hand, this study primarily used the continuous cyclic loading method to complete the tests. Although tests were also conducted using the cyclic loading with tissue rest method, no significant differences were observed, no in-depth research was conducted in this area for the same reason.

The findings of this study provide valuable insights into the material properties of intestinal tissue under cyclic loading conditions. As highlighted in the data, limiting preconditioning to six cycles was sufficient to establish reproducibility while avoiding

unnecessary mechanical loading.

3.3.4 Strain-rate test and stress relaxation test

In this section, to investigate the viscoelastic properties of porcine intestinal tissues and the effect of loading rate on tissue response, a series of indentation tests were conducted and stress-strain and stress-time data were obtained under controlled conditions. Additionally, the mechanical behaviour of animal tissues was compared to synthetic tissues to identify differences. Curve-fitting techniques were applied to mathematical models to evaluate their ability to accurately represent the observed mechanical properties.

3.3.4.1 Method

Still using the IMADA testbed, the overall test protocol was shown in Figure 3.11a. Based on the previous results, six preconditioning cycles were conducted at the same loading rate used in the subsequent tests. The primary tests were then carried out by using the strain-control method, beginning with the loading phase, where the indentation probe applied a controlled displacement to the tissue at predefined constant loading rates. These rates were selected based on the physiological range of intestinal tissue segmentation movement from previous studies and included 0.5, 3, 6, 9, and 12 cm/min [113–115]. The strain rate was replaced by the loading rate to simplify the experimental procedure. The tissue was compressed to a strain corresponding to approximately 50% of its initial thickness, consistent with methodologies reported in prior studies.

After reaching the target strain, the indentation probe was held in position for 30 seconds to observe the stress relaxation behaviour of the tissue (Figure 3.11b). This time duration was determined based on preliminary tests, which indicated that it was sufficient to capture the characteristic stress decay observed in viscoelastic materials. During this relaxation phase, the force applied by the tissue to the indenter was recorded as a function of time. Following the relaxation phase, the probe was retracted at the same speed used during loading, completing the unloading phase. The SynDaver synthetic tissue also followed the same method to conduct these tests.

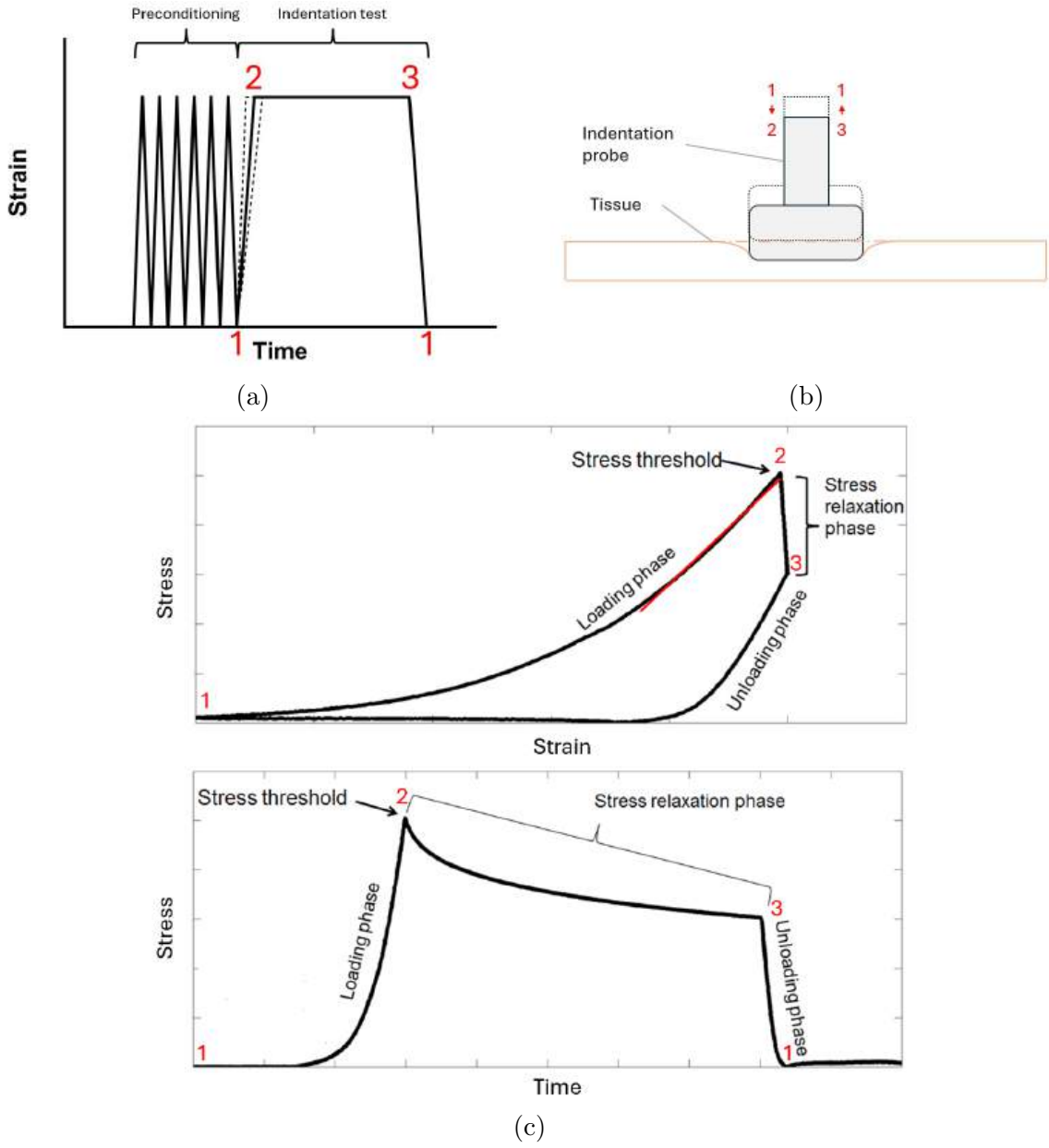

Figure 3.11: (a) Test protocol for the strain-rate effect on stress relaxation. (b) Illustration of the relative movement between the indentation probe and the tissue sample. (c) A typical indentation test on soft tissue response yields two key curves: the Stress-Strain curve (top) and the Stress-Time curve (bottom). Adapted from [99].

Previously, indentation tests were performed at a single location under varying strain rates to directly observe the effects of loading rate variations while controlling the variable of doing tests on the same spot. However, this approach presented significant challenges. The recovery time between tests was either insufficient or hardly unverified for the tissue to fully restore to its original state. Moreover, the extent of recovery in ex vivo tissues remained uncertain. As a result, subsequent experiments functioned as compression tests on tissue already deformed from prior tests, leading to errors in strain calculations. These errors arose from using the tissue's original thickness rather than its actual compressed thickness after each test. While adjustments using the real compressed thickness improved accuracy, this method artificially increased the tissue's apparent elastic modulus, deviating from its true mechanical properties. Therefore, loading rate tests were conducted at different distinct tissue spots. This approach eliminated the recovery-related issues of the previous method. Although the tests were conducted on different spots, introducing other factors that could affect the accuracy of the conclusions, assuming the structure integrity of the tissue, this method provided a more reliable representation of the tissue mechanical behaviour.

The typical tissue responses are represented in both the stress-strain and stress-time graphs, shown in Figures 3.11c. Each loading rate was tested ten times (five speeds across five different spots on each tissue sample), with the results averaged to ensure reliability. The linear modulus was calculated for each test using the same method as in the preconditioning tests. Model fitting to describe the stress response was performed using the MATLAB 'Curve Fitter' app, with the following equations as input and the values for the variables were automatically calculated. It is important to set the minimum value of variables greater than zero to avoid incorrect results.

For the compression phase, Woo et al. [116] proposed that the non-linear elastic response function for soft tissue to fit the curve:

$$\sigma(\varepsilon) = A\left(e^{B\varepsilon} - 1\right) \tag{3.3}$$

where $\sigma(\varepsilon)$ is the stress at strain ε, A is a linear factor, and B is a non-dimensional parameter. Both A and B are obtained by calibrating the model against the experimental data.

For stress-relaxation phase, followed by the conclusion of previous studies, equation 2.3 of 5-element DMW model was used to fit the curve and the parameters E_0, E_1, E_2, η_1, and η_2 are determined by fitting the model to the experimental data. Subsequently, the viscoelastic ratio VR is defined as the ratio of the relaxed modulus E_∞ to the instantaneous modulus E_{ins}. The relaxed modulus is determined when time approaches infinity which is E_0. The instantaneous modulus E_{ins} is determined as the sum of the three moduli ($E_{\text{ins}} = E_0 + E_1 + E_2$), representing the initial stress modulus value observed at the onset of the stress relaxation process, where the peak stress occurs [117]. Therefore, the overall equation can be described as:

$$VR = \frac{E_\infty}{E_{\text{ins}}} = \frac{E_0}{E_0 + E_1 + E_2} \tag{3.4}$$

A smaller VR value signifies a larger percentage of stress relaxation, while a larger value indicates a smaller percentage of stress relaxation [118,119]. The changes in the linear modulus, model parameters, and viscoelastic ratio VR were analysed to better understand how the mechanical properties are influenced by the loading rate.

3.3.4.2 Results

The results of the two tissue types' responses under different loading rates are shown in Figure 3.12, while the linear modulus and fitting properties are presented in Tables 3.3, 3.4, and 3.5. To directly compare the stress relaxation rates, normalized stress was used due to differing starting stress values. The viscous moduli were ordered from the lowest to the highest ($E_1 < E_2$) for easier comparison. The original curves can be found in Appendix B. The stress-strain curves illustrate how the tissues deform under applied stress, providing insights into their elasticity and stiffness. In contrast, the stress-time curve captures the tissues' viscoelastic behaviour by showing how stress varies over time under constant strain.

The effect of varying strain rates on the stress-strain responses of porcine tissue was investigated (Figure 3.12a, Table 3.3). The five average curves of each loading rate exhibited the same trend, following the typical J-shaped line. The results show that higher strain rates lead to a quicker tissue response, as evidenced by the smaller strain value at the inflection point where the tissue enters the viscoelastic region. Additionally, the curve becomes steeper at higher strain rates, resulting in larger peak stress values at the same strain limit. The average $\pm$ SD values for linear

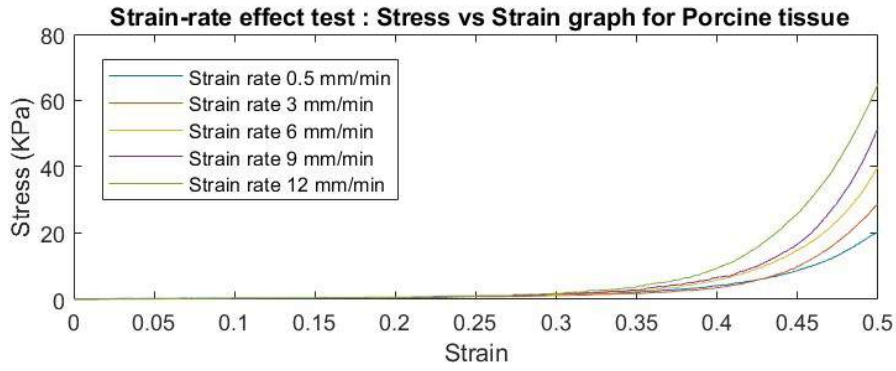

(a)

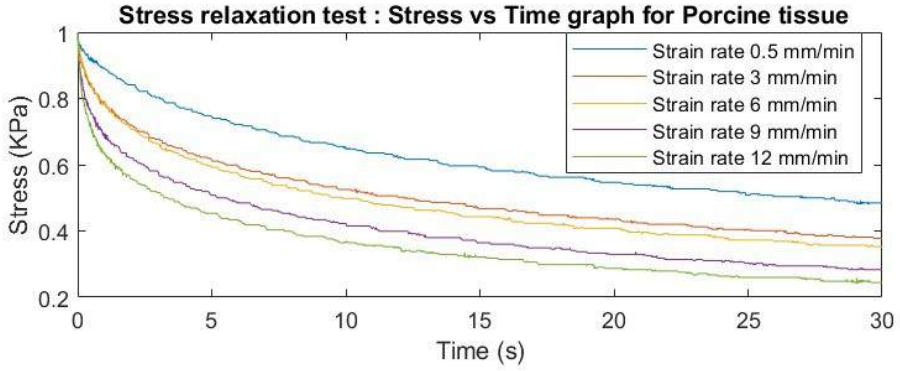

(b)

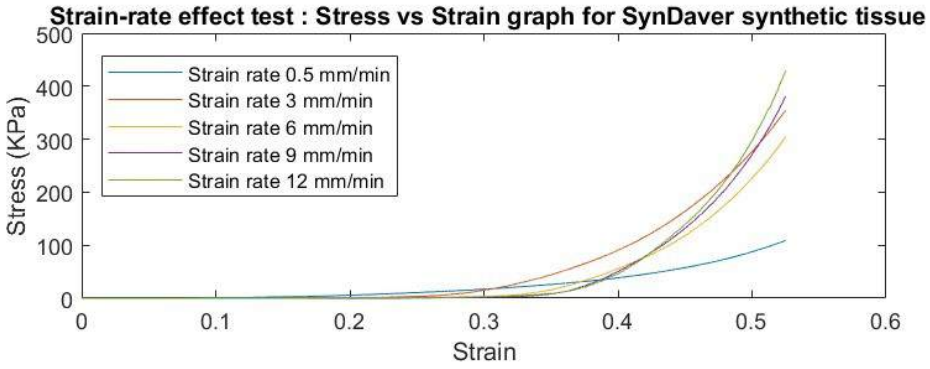

(c)

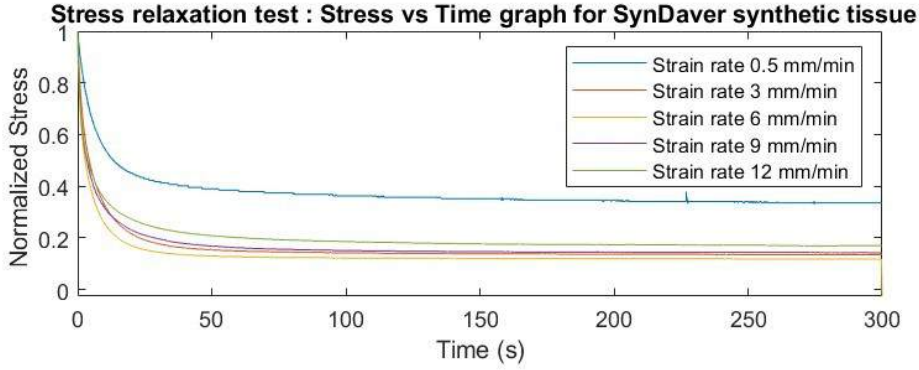

(d)

Figure 3.12: (A) Strain-rate effect test: Stress vs Strain graph for Porcine tissue. (B) Stress relaxation test: Stress vs Time graph for Porcine tissue. (C) Strain-rate effect test: Stress vs Strain graph for SynDaver synthetic tissue. (D) Stress relaxation test:

modulus (KPa) could also support this situation, calculated from the slope of the stress-strain curve for loading speeds ranging from 0.5 to 12 mm/min, were 287.4 ± 98.8, 452.6 ± 161, 655.9 ± 177.4, 898.5 ± 201.3, and 923.6 ± 187.63, respectively. Data analysis showed that for each loading speed, the linear modulus values are normally distributed. Notably, the linear modulus values for loading rates of 9 and 12 mm/s did not show significant differences, but overall, the data suggest that the linear modulus is strain-rate dependent. Table 3.4 presents the fitting values of the variables used to describe the viscoelastic model during the compression phase. All fitting models have R^2 values greater than 0.99, indicating the goodness of fit of the model. It is observed that as the loading rate increases, the properties of variable A show a decreasing trend, while those of variable B exhibit the opposite behaviour.

The results of the loading rate effect on stress relaxation are shown in Figure 3.12b, and the model fitting results with VR values are presented in Table 3.5. Consistent with previous studies, the stress-relaxation curves of porcine intestine exhibited a similar downward trend and were nonlinear over time [42,45]. All five curves initially decreased sharply within the first 10 seconds under constant strain, then gradually slowed down before flattening out, reaching an equilibrium state. Among them, at higher loading rates, the curve showed a steeper initial drop in stress, indicating a more rapid relaxation, exhibited a less viscous response in the short term. At the end of the relaxation time, the final stress values exhibited a downward trend, following the sequence from 0.5 to 12 mm/min, from top to bottom. This indicates that higher loading rate corresponds to the larger percentage of total stress relaxation. These phenomena were also reflected in the changes in the model variables and VR values as the loading rates change. As the VR decreased which suggests that the tissue experienced a larger percentage of stress relaxation at higher loading rates so that the curves of high loading rates were at the bottom. Meanwhile, at lower loading rates, the higher viscosity coefficients of models leads to greater resistance to stress relaxation, resulting in slower downward-creep. The variables exhibited a consistent trend with increasing loading rate, resulting in a larger E_1, while all other variables decreased.

The behaviour of SynDaver tissue in both the compression and stress-relaxation phases differed significantly from that of porcine tissue. Specifically, the inflection points showed opposite trends: at higher loading rates, the transition occurred later. The linear modulus across different loading rates followed a similar trend as the

porcine tissue and the peak stress at the strain limit was lower at lower loading rates. As shown in Table 3.3, the linear modulus values for SynDaver tissue were considerably higher than those for porcine tissue, ranging from 587.9 to 3434.6 KPa, with larger standard deviations. For the stress-relaxation test, the curves did not follow a clear trend. The 0.5 mm/min curve exhibited distinctly initial slower creep, while the other curves show similar stress drops. The sequence of stress relaxation percentages, from smallest to largest, was 0.5, 12, 9, 6, and 3 mm/min. This trend was also reflected in the model fitting results. While the compression models generally followed the same trend as porcine tissue (except at 0.5 mm/min), the other variables and VR showed an opposite trend in the stress relaxation phase, increasing with higher loading rates, unlike the decreasing trend seen in porcine tissue.

Loading Rate (mm/min)	**SynDaver Intestine (kPa)**	**Porcine Intestine (kPa)**
0.5	587.9 ± 172.9	287.416 ± 98.8
3	1867.9 ± 200.7	452.6 ± 161
6	2034.4 ± 283.4	655.9 ± 177.4
9	3022.8 ± 434.6	898.5 ± 201.3
12	3434.6 ± 463.1	923.6 ± 187.63

Table 3.3: Linear Modulus for SynDaver and porcine intestine at different loading rates.

Loading rate (mm/min)	**SynDaver intestine**		**Porcine intestine**	
	Property			
	A	**B**	**A**	**B**
0.5	1.448	6.025	0.007289	15.82
3	0.4069	8.756	0.001643	19.48
6	0.09059	10.69	0.001566	20.28
9	0.04453	12.02	0.001272	21.17
12	0.03274	12.62	0.001242	21.9

Table 3.4: Variable properties of the compression phase for the average curve of SynDaver and porcine intestine at different loading rates.

Tissue type	Loading rate (mm/min)	Property					
		E_0 (KPa)	E_1 (KPa)	E_2 (KPa)	η_1 (KPa s)	η_2 (KPa s)	VR
SynDaver intestine	0.5	48.67	16.58	75.24	1195	486.3	0.346
	3	47.39	142.6	174	1478	320.4	0.130
	6	59.43	154.9	192.6	2131	524.8	0.146
	9	75.35	135.3	253.6	2580	662.3	0.162
	12	100.3	116.8	279.2	3382	912.2	0.202
Porcine intestine	0.5	21.35	8	26.66	18.32	493.6	0.381
	3	19.58	11.78	22.88	13.89	318.5	0.361
	6	18.24	12.7	23.27	15.81	299.8	0.336
	9	15.14	14.7	22.94	11.99	261.9	0.287
	12	13.41	17.5	21.19	12.66	223.4	0.257

Table 3.5: Variable properties of the stress relaxation phase for the average curve of SynDaver and porcine intestine at different loading rates.

3.3.4.3 Discussion

Accurate characterization of biological tissue mechanics is crucial for advancements in applications such as surgical simulation, synthetic tissue development, and tissue-device interaction studies [46]. In this study, the stress-strain and stress-time responses during compression and stress relaxation of porcine intestinal tissue were measured. The representative average results for each loading rate were used to adapt viscoelastic models, which successfully describe the mechanical properties with a high goodness of fit. Comparison with previous studies shows that the behaviour of strain rate effects during the compression and stress relaxation phases of porcine tissue is consistent with findings from other soft tissue loading tests [99,105,120,121]. The linear modulus of the pig large intestine at an indentation speed of 0.1 mm/s (approximately 0.5 mm/min) was around 350 kPa, yielding consistent results. Furthermore, when compared with the modulus of the acrylic support used in the holder, it was determined that the base effectively acted as a 'rigid' support. This indicates that the measured results are mainly reflect the properties of the intestinal tissue with minimal effect caused by the support material.

Using a large sample-to-tip dimension ratio ensured realistic volume comparisons between the capsule robot and the intestine, aligning with actual conditions. The tissue holder that can contain PBS was designed to avoid hydration problems. The loading rates were carefully determined by referencing the actual intestinal segmentation speed to avoid the risk of causing significant vibrations. By comparing the results across different loading rates, the study evaluated the dependence of tissue viscoelasticity on loading rate. It is clear that higher loading rates result in increased stiffness, as indicated by the higher linear modulus.

Intestinal tissues have a complex hierarchical structure such as the mucosa, submucosa and serosa layers, meaning that different levels of tissue organization (from the molecular level to the fibrous network) contribute to the stress relaxation process. These hierarchical relaxation mechanisms combine to produce a two-phase stress relaxation profile, an initial rapid decay (due to fast processes) followed by a slower, more gradual stress reduction as slower relaxation mechanisms dominate [122]. The fast relaxation (the early phase of rapid stress drop), occurs because the fibers within the tissue slide relative to one another, and bonds, such as those between collagen fibers, break [121–123]. This phase involves quick redistribution of the tissue deforming or adjusting to the applied strain [124]. Following this, the slow relaxation (later phase) occurs, where the relaxation rate slows down. In this phase, fibers experience slower movement as they reorient or slide within their matrix, and internal molecular interactions, like interfibrillar sliding or crosslink breaking, adjust over time [121]. The slower relaxation is due to the more time-consuming processes at the molecular and fibrillar levels, where bonds and molecular interactions are reformed or realigned.

The rate at which strain is applied to the tissue also affected the observed stress relaxation behaviour. When strain is applied slowly (at a low strain rate), more time is available for the fibers to slide and for bonds to break or reform, resulting in a greater dissipation of viscous stress in the loading phase. Conversely, when strain is applied quickly (at a high loading rate), there is less time for the fibers to slide or for internal bonds to break during the compression phase (ramp period). This leads to the majority of the viscous stress decay occurring during the initial phase of stress relaxation. This can be reflected onto the components of the viscoelastic model. For example, the high viscosity tissue resists stress relaxation more because of the higher internal friction or resistance to motion at the molecular or microstructural level. While smaller η_i and VR values mean a less viscous response of the material to a mechanical stress, tend to creep more quickly and relax stress more readily when a constant strain is applied.

The results indicated that SynDaver synthetic tissue does not exhibit similar mechanical properties or loading responses as porcine tissue. The data did not show consistent regularity, which may be attributed to two main factors: first, the manufacturing materials and processes result in structural variations across different positions, unlike the uniformity biological structures found in animal tissue. Second, synthetic tissues tended to lose moisture and dry out during experiments, which may

explain why they appear stiffer at lower loading rates, likely due to dehydration over the course of the experiment. Additionally, the linear modulus of synthetic tissues was much higher than that of animal tissues, combined with other differences discussed in the results section, this further emphasizes the disparities between the two tissues. Given these conclusions, it is important to carefully consider the use of synthetic materials in future experiments.

3.4 Measurement of surface textures of porcine intestinal tissues

3.4.1 Introduction

As stated in the literature review, the surface texture of the small intestine wall is extremely complex. The intricate physiological activities, including digestion and peristalsis, contribute to the unique "circular folds" structure of the small intestine. In addition, the surface texture is not uniform, but varies in each segment of the small intestine across individual organisms. These characteristics of the small intestinal surface profoundly impact the frictional movement of capsules within the small intestine. However, there is a deficiency in the existing literature regarding relevant knowledge on this topic.

Therefore, the measurement of surface textures of intestinal tissues has two main implications. First, the uneven surface texture and tissue biological variability will inevitably affect friction. If more accurate knowledge in this regard can be obtained, it will be helpful for understanding subsequent frictional behaviours. Second, if more realistic artificial intestinal tissues are to be fabricated, precise mapping of the distribution of the surface texture is essential.

To address the research gap, Microset replicating material was employed to capture the surface texture of the small intestine for a detailed investigation of its shape. Results were systematically recorded and analysed, leading to comprehensive insights and conclusions.

3.4.2 Method

3.4.2.1 Tissue preparation

As stated before, tissue samples were obtained from the mid sections-small intestine of twelve pigs. Samples were cut, washed, and stored in 4°C PBS solution. Before starting the experiment, cotton balls were used gently to absorb excess residual liquid on the surface (try not to compress the tissue) to maximize the acquisition of the most realistic data of surface textures.

3.4.2.2 Copy surface textures of tissues

Previous attempts to observe the tissues directly using the Alicona device were unsuccessful, as illustrated in Figure 3.13. The black areas in Figure 3.13a represent regions of the small intestine's surface that the Alicona failed to capture accurately. The problem is that Alicona uses an optical system that obtains the 3D planar data by continuously changing focus and scanning vertically, but the existed probe in the lab was unable to cope with a shiny surface with irregular surface patterns like tissues.

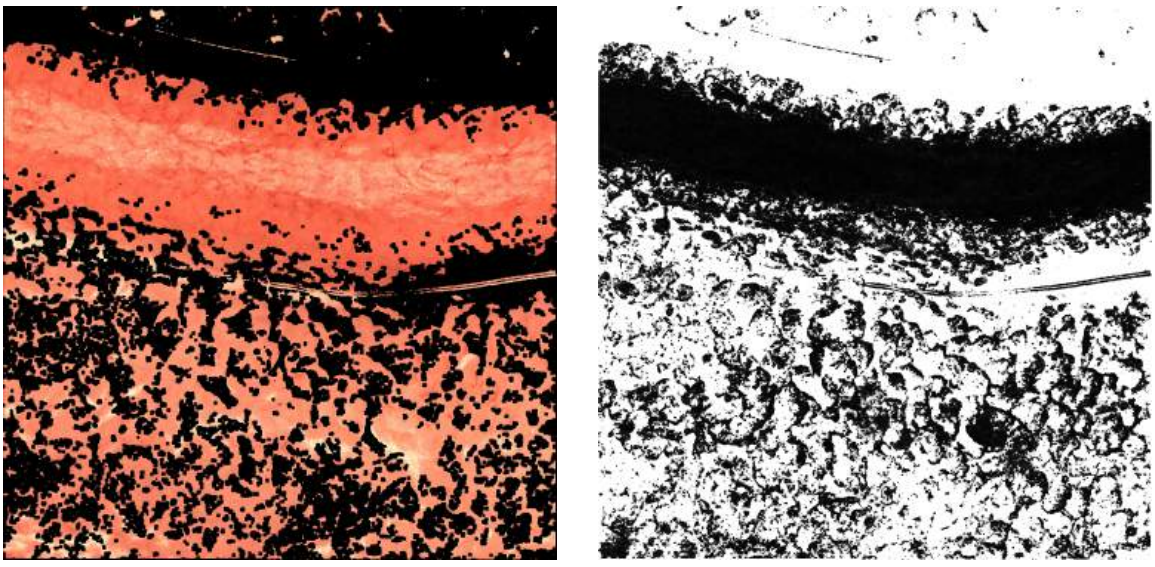

(a) (b)

Figure 3.13: Photos of unsuccessful imaging of porcine tissue: (a) Texture; (b) Quality map.

Therefore, instead of scanning tissues directly, Microset 101 RF fluid (Microset Products Ltd) replicating compounds were used to capture the surface texture of the

intestinal tissues. The idea was inspired by a similar method of defecting metal damage, this rapid cure material can replicate the surface in a very high solution of 0.1 microns. The replicating compounds were sprayed onto the tissue and a backing slide was placed on the replica. A small, even force was applied to the slide to ensure that the slide, replica and tissue fit tightly together to eliminate as much air as possible. After five minutes of cure time, the slice was removed, and the surface was cleaned and dehydrated and ready for later scanning.

To validate the feasibility of this method, photographs were taken before, during, and after the tissues were covered with Microset fluid. These images were captured to compare whether there were deformations on the tissue surface due to fluid coverage and energy dissipation of curing.

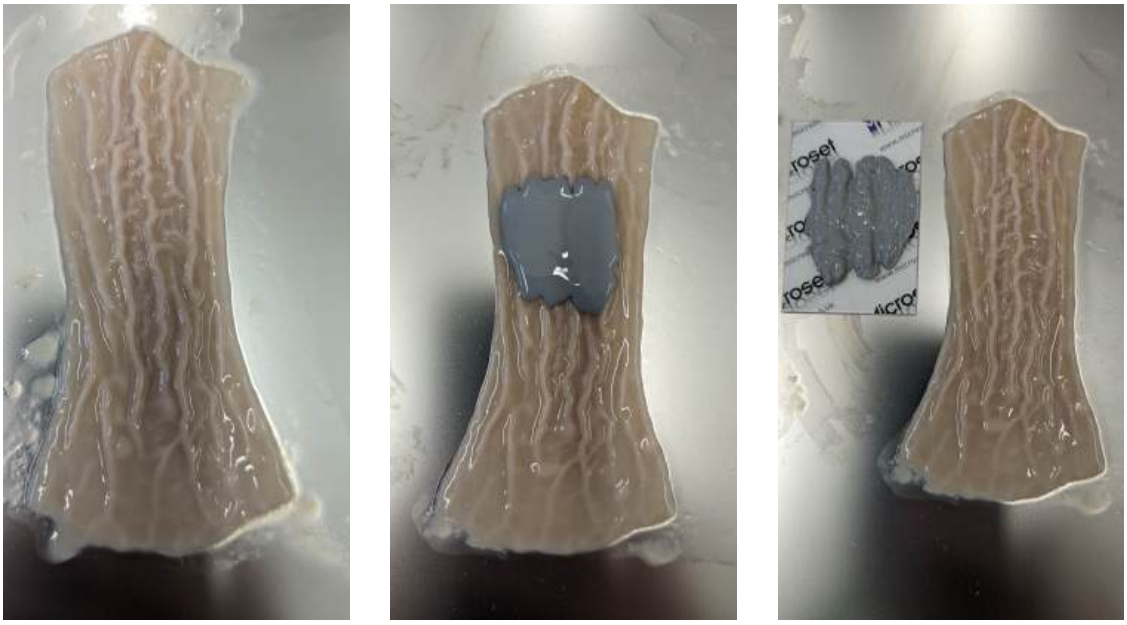

(a) (b) (c)

Figure 3.14: Pictures of spraying Microset compounds: (a) Before; (b) Capturing; (c) After onto the intestinal tissues.

3.4.2.3 Data acquisition from Alicona

The shape of the circular folds were acquired by using the Alicona. Alicona (InfiniteFocusSL) is a cost-efficient optical 3D measurement system for easy, fast and traceable measurement of shape and finish on micro structured surfaces. For each

measurement, a $2.5 \times 2.5\,\mathrm{cm}^2$ square area was selected to assess surface texture, resulting in high-contrast colour images with enhanced depth of focus.

Even though replicas were used to get better scan data and various settings of contrast, brightness and resolutions were tried, blank spots and holes still occurred in some irregular areas (Figure 3.15a). Therefore, to avoid the impact of these not scanned areas on experimental data, a newly filtered region of each sample was chosen to analyse data (Figure 3.15b). After this, colourful image of the height was generated to figure out the highest peak of the surface which represent the most protruding section of the tissue which can be referred to the presence of circular folds (Figure 3.15c). And then, a side cut of this section was done to analyse its shape, length and height (Figure 3.15e).

3.4.3 Results

The photos of the tissue before and after the replication tests were compared, showing no visible changes. This suggests that the impact of the curing effect of the Microset fluid is minimal and acceptable. It can be seen that the circular folds on the surface of the small intestine are arranged in a grid pattern, with axial folds being the most prominent. Additionally, circumferential folds connect these axial folds, linking themselves together.

As shown in Figure 3.16a, the length and height of folds ranged from 1.342 mm to 2.755 mm and 281.4 μm to 1234 μm with the standard deviation of 435.7 and 294.3, respectively (Statistic table is available in Appendix C). L. Sliker et al. reported similar measurements for small bowel tissue, validating the accuracy of these measurements [45]. The high standard deviation in fold length indicates significant variability. Longer folds are observed at the junctions where axial and circumferential folds intersect. The average fold height was 703.1 μm, which is consistent with previous tissue thickness measurements (Figure 3.7a), as the difference between the two large groups of values is approximately 0.7 mm. The fold height also showed significant variation, with some regions exhibiting sharp, pronounced folds, while others were more subdued or flattened, contributing to a diverse and irregular surface profile.

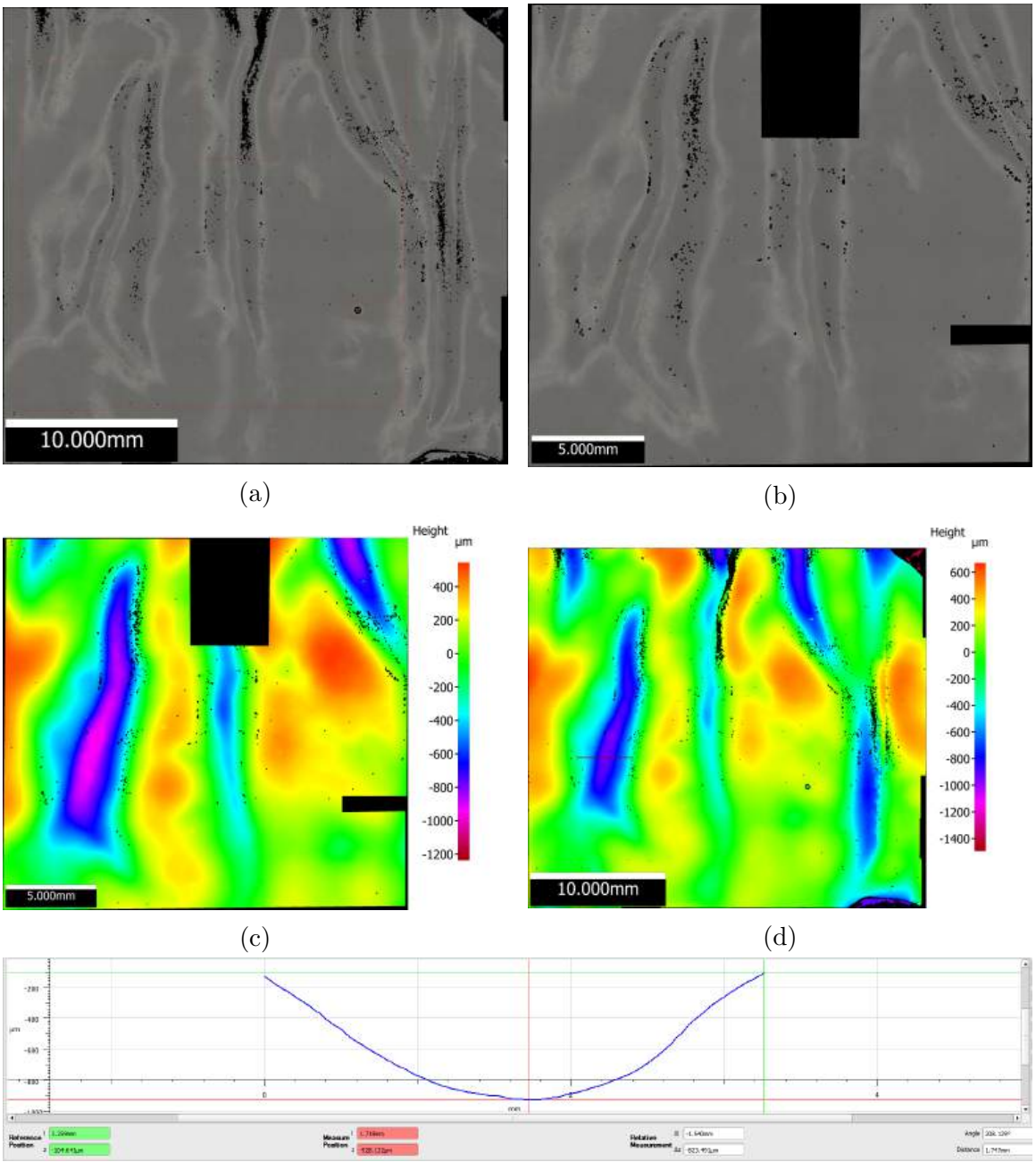

Figure 3.15: Alicona figures: (a) Original graphics; (b) Selected area after filtration of blank area; (c) Colour image of depth (height) of the surface; (d) Selected line of side cut based on the lowest point of the circular fold; (e) The shape of the circular fold.

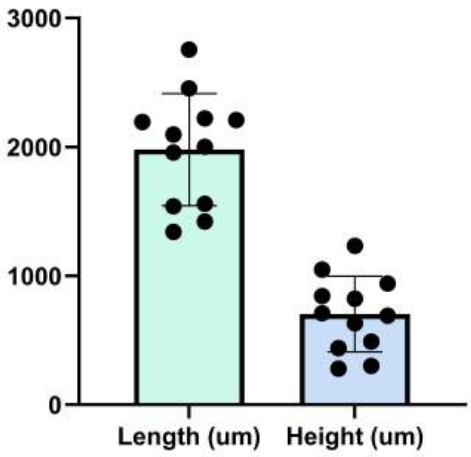

(a)

Figure 3.16: Folds' height and length measurements for 12 samples.

3.4.4 Discussion

In terms of general surface pattern, the circular folds of the small intestine were observed to form a series of concentric ridges on the intestinal surface. The folds themselves followed an irregular pattern where the circular folds were not uniform and not evenly distributed. While some sections of the tissue showed highly pronounced and regular folds, other areas demonstrated less defined or more scattered folds (Figure 3.17). This irregularity, combined with variations in fold height and width, is likely to influence the overall surface flatness. More prominent and elevated folds contribute to increased topographical variation, which in turn can elevate the frictional forces experienced by objects traversing the intestinal lumen.

The measurement of the height and width of the largest folds provides further insight into the anatomical features of the small intestine. These folds, which are part of the circular folds of the intestine, contribute to the increased surface area for digestion and nutrient absorption. The data suggest that while some folds are relatively small, others are much larger which reflects the natural variability in fold size across different tissue sections, indicating a non-uniform distribution of fold sizes across the tissue. This variation may have functional implications, as larger folds may contribute more significantly to the mechanical properties of the tissue. Also, the variability in folds' length and height values across different samples suggests that surface texture may differ notably between intestinal segments and across individuals.

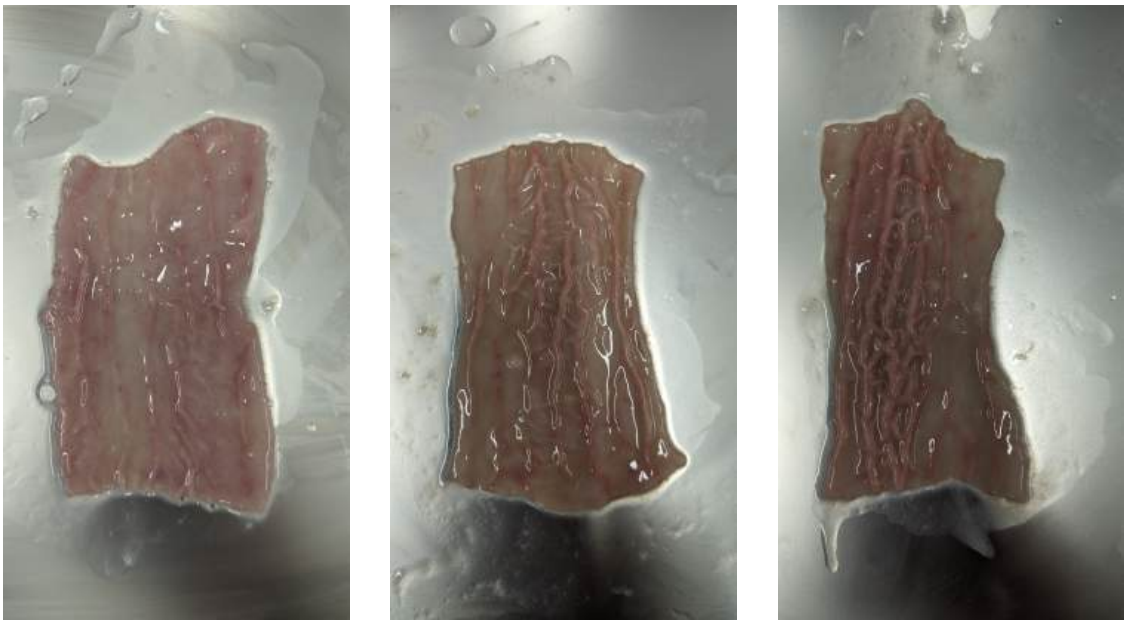

(a) (b) (c)

Figure 3.17: Images of three samples were compared to highlight the differences in their surface textures.

It should be noted that human error could influence the measurement accuracy. It is difficult to completely remove surface liquid and air bubbles prior to Alicona scanning, and the force applied to press the slide against the tissue may compress the soft tissue, potentially affecting the surface texture. When selecting the measurement area, the process remains somewhat subjective. For instance, choosing a section with more concentrated folds could significantly alter the results. Additionally, determining the precise endpoint of the fold length is challenging. These areas still require improvement.

3.5 Conclusions

Incorporating the IMADA tester and designed devices, a methodology for performing indentation tests on soft tissues was successfully developed.

Preconditioning tests on porcine intestinal tissue were completed and proved that tissue became more elastic and stiffer during loading-unloading cycles, and the results showed that the tissue generally took six cycles to reach a steady state.

A series of comprehensive measurements of porcine intestinal tissue properties were conducted, including tissue thickness, surface patterns, circular fold dimensions, stress-strain relationship, stress-time relationship, linear modulus, and viscoelastic model fitting under different loading speeds. It was observed that higher strain rates resulted in faster tissue responses, increased linear modulus, and a more rapid initial stress relaxation phase, with a greater percentage of overall stress reduction.Furthermore, these investigations provided a deeper understanding of the viscoelastic nature of intestinal tissue, including its time-dependent behaviour, hysteresis phenomenon, and valuable insights into tissue response for subsequent friction tests.

SynDaver synthetic tissue and porcine intestine exhibit significant differences in mechanical property tests. Therefore, ex vivo porcine tissue would be used in later friction experiments instead of synthetic tissues.

The stress-strain and stress-time data from this study offer valuable insights for designing silicone substrates that mimic real conditions more closely for developing the testbed for friction test in the next chapter. Additionally, when integrated with surface measurement data, these findings could contribute to the development of more realistic synthetic intestines in the future.

Chapter 4

Development of the methodology for ex vivo tribological assessment of endoscopic capsule intestinal interactions

4.1 Introduction

From the conclusions of literature review in chapter 2.3, it is evident that there are areas for improvement in previous test bench configurations and methodologies. Therefore, the work set out in this chapter is to establish an ex vivo methodology that mimics the interactions between capsules and the intestinal lumen to assess friction behaviours, and ultimately provide guidelines for other researchers in the field to measure these properties. By combining the laboratory's existing equipment with an analysis of previous test benches, the Universal Mechanical Tester (UMT, Bruker Corporation, USA) was selected as the primary tribometer. The setup, equipped with capsule prototypes, an adjustable angle probe holder, and a bathtub-like tissue holder, enables experiments for various research objectives. After initial testing, the experimental designs were reviewed to identify unreasonable aspects, leading to the development of improved designs that better meet experimental requirements.

Additionally, the experimental methods were enhanced compared to those used in previous studies. As detailed in the previous chapter on small intestinal tissue characteristics, a method involving repeated unidirectional sliding cycles was adopted to account for the preconditioning effect and achieve a repeatable mechanical response. Furthermore, intestinal fluid was incorporated into the experimental environment by creating a synthetic mucus to simulate the intestinal juice typically secreted by glands

during digestion.

Finally, the establishment of this ex vivo methodology and the use of the testbed have demonstrated that stable and continuous friction data can be successfully obtained. This test bench shows significant potential for investigating the interactive effects of various variables on capsule robots and small intestinal tissue, providing valuable insights and laying a robust foundation for subsequent friction experiments.

4.2 Initial designs of the test platform

This section introduces the various components of the testbed, explaining the rationale behind their selection as well as the design concepts.

4.2.1 UMT machine

The UMT machine is a highly versatile and precise instrument extensively used in tribological and mechanical testing. Its modular design enables users to customize the system with various sensors, environmental chambers, and accessories to meet specific testing requirements. In this study, the advanced DFH-5.0 sensor was used to measure load, torque, and displacement changes during the friction tests, ensuring high measurement precision, crucial for generating accurate and reproducible results. The UMT's software supports real-time data acquisition and analysis, facilitating stable or immediate adjustments to outputs such as loads and speeds, as well as an in-depth examination of material behaviour. According to the specifications and dimensions of the linear drive platform, custom test protocols were able to be created and installed freely. Additionally, the UMT offers automated testing features that streamline processes and improve throughput by reducing the need for constant manual intervention. Therefore, after thorough evaluation, the UMT machine was selected as the primary instrument for conducting experiments and recording data, with supplementary equipment added to complete the entire experimental setup.

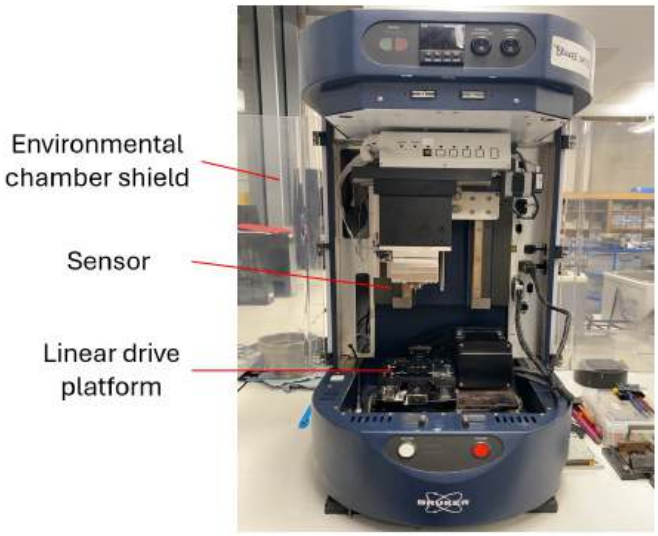

Figure 4.1: The UMT machine was selected as the primary tribometer for conducting friction tests.

4.2.2 Design of capsule prototype

The shell structure of commercially available capsule endoscopy products is simple, typically consisting of a cylindrical body between two hemispheres, as suggested by the name "capsule". Given that this study focuses on the frictional interaction between the small intestine and the capsule robot, and considering the high cost of commercial capsule endoscopes, it was determined that purchasing a real capsule endoscope was unnecessary. Instead, a custom-designed prototype was developed to conduct the preliminary test as shown in Figure 4.2.

The mechanical component adopts an integrated design, which can be divided into three main parts. The uppermost part consists of a cylindrical structure designed to connect to the UMT holder. Specifically, the UMT holder is a hollow cylindrical sleeve, with dimensions comparable to the cylindrical part on the prototype. Once inserted, the frictional force between the parts ensures a stable connection, maintaining the fixture's position during operation.

The central region features a perforated disc that serves as an angle-locking mechanism. The operating principle of this device is similar to that of the connection mechanism, with grooves on the disc designed to lock into the cylindrical part of the UMT holder. This locking system allows the user to select and fix the orientation of the capsule's head during the experiment, ensuring stable angle positioning

Figure 4.2: CAD model of the capsule prototype design is shown in the front view (left), oblique view (middle), and side view (right).

throughout the process. The disc will be firmly pressed against the holder's boundary, ensuring that the capsule remains parallel to the horizontal plane during the tests.

At the bottom of the structure lies the simulated capsule shell. According to the product data gathered in Table 2.1, the dimensions of the simulated capsule are 11 mm in diameter and 26 mm in length. This design ensures that the size of the simulated capsule closely matches that of the actual product, enhancing the realism and effectiveness of the experimental simulation.

The capsule prototype was manufactured using 3D printing with PETG. Since this design was intended for preliminary testing, additional angle holes and capsules with different dimensions were manufactured after the methodology was validated.

4.2.3 Tissue holder

The tissue holder used was the same as the one employed in the previous mechanical properties test as shown in section 3.3.1.1. The core function and primary design concept of the tissue holder setup are threefold. First, it must securely hold the intestinal samples in place for testing. Second, it should be capable of contain liquid to simulate the presence of intestinal juice, semi-fluid-solid mixtures like chyme, or even more complex pathological conditions such as blood. Third, the setup aims to replicate the soft contact characteristics of the small intestine in its natural position

inside the body. This could be achieved by layering the intestinal tissue over a silicone substrate. The small intestine, which is approximately 5-7 meters long in adults, is tightly coiled in the lower abdominal cavity due to space limitations. Therefore, a soft substrate with mechanical properties similar to real tissue was implemented in this study. The compression behaviour of the supporting material was considered to achieve a stress-strain curve that mirrors that of real tissue, ensuring similar deformation under loading conditions.

4.2.3.1 Silicone substrate fabrication

Previous work including compression tests, were performed to learn the stress-strain relationship of the porcine intestinal tissue (3.3.4). After that, groups of Polycraft GP3481-F silicone (MB Fibreglass company) with different deadener weight ratios were manufactured to compare which compounds were closest to the original tissue. The specific manufacturing process is introduced as follows.

The preparation of silicone substrate followed a systematic procedure to ensure uniform consistency and high-quality results. Clean, contaminant-free container cups were used to measure 100 parts by weight of silicone base, 10 parts by weight of silicone catalyst, and 30, 40, or 50 parts by weight of deadener. The addition of Polycraft silicone deadener (MB Fibreglass company) was aimed at reducing the stiffness of the silicone by limiting the cross-linking of polymer chains during the curing phase. These specific ratios were chosen to determine which formulation best replicated the properties of real tissue. During testing, it was found that the deadener should not exceed a 10:1:5 ratio of the total silicone mixture, as higher amounts may interfere with the curing process and negatively impact the final properties of the material. The base, curing agent, and deadener were thoroughly mixed manually using a clean stick to ensure uniform dispersion of the components. It should be noted that excessive mixing was avoided to prevent overheating of the mixture, ensuring the temperature did not exceed 35°C as suggested. To eliminate any trapped air, the mixture was subjected to vacuum de-airing. In this process, the mixture was placed in a vacuum chamber, where it was allowed to expand fully and then collapse (Figure 4.3a). This step was repeated for 1–2 minutes to ensure all air bubbles were removed. After vacuum de-airing, the mixture was inspected for remaining air bubbles to confirm its readiness for use. During this procedure, the volume of the mixture increased by 3–5 times; therefore, large plastic cups with sufficient capacity were used to accommodate

the expansion. Once de-airing was completed, the mixture was immediately poured into the mold, which had been pre-treated with silicone mold release spray, to prevent air entrapment that could compromise the material's quality (Figure 4.3b). The silicone mixture was then left to cure at room temperature, solidifying into a flexible substrate within 24 hours.

(a) (b)

Figure 4.3: (A) Vacuum machine that was used for de-airing. (B) Silicone curing in the mould.

4.2.3.2 Silicone comparison

The stress-strain graph derived from indentation tests comparing porcine intestinal tissue with silicones demonstrates distinct mechanical behaviours under compression. The tests, performed using identical protocols (3.3.4.1) on porcine tissues and silicone samples at a constant loading rate of 9 mm/min, produced averaged results for comparison (Figure 4.4).

From the graph, a clear trend is observable: increasing the deadener weight ratio in the silicone compositions (10:1:3, 10:1:4, and 10:1:5) shifts the stress-strain curves progressively to the right. This indicates the silicone became softer (smaller stress value under same strain) with higher deadener ratios. However, even with the highest ratio of 10:1:5, the silicone materials exhibit stiffer behaviour compared to the porcine small intestinal tissue, as reflected by the significant gap of the stress-strain curve for the tissue at same strain levels. Additionally, the stress relaxation tests highlight further differences between the silicones and the biological tissue. When

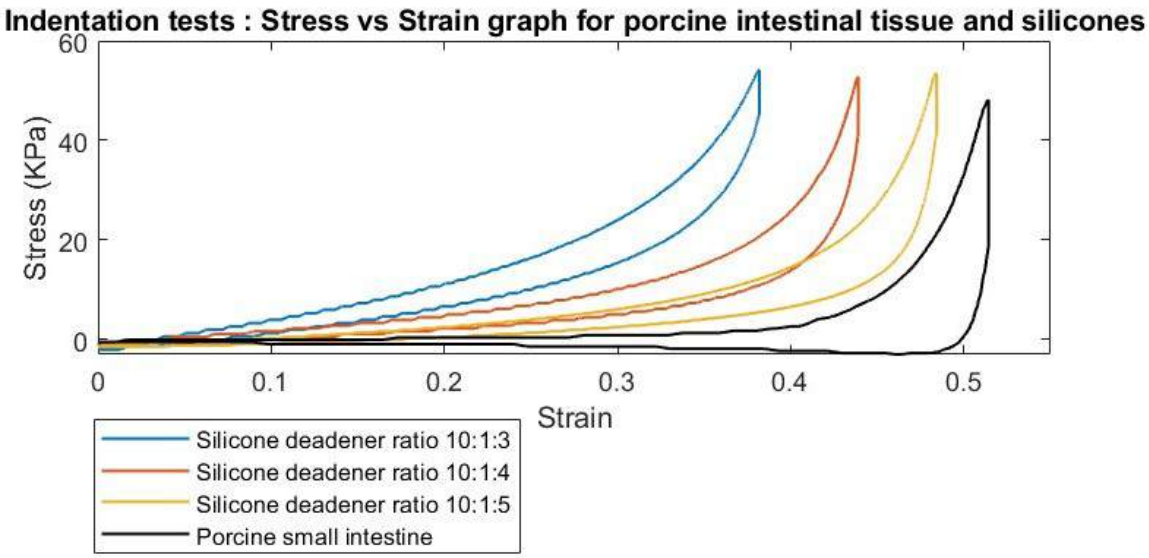

Figure 4.4: Comparison of indentation test results for porcine intestinal tissue and silicone materials.

subjected to constant strain, the porcine tissue demonstrated a larger degree of stress relaxation, evidenced by a more substantial reduction in stress over time compared to the silicone samples. This finding emphasizes the pronounced viscoelasticity of the intestinal tissue, which is challenging to replicate in synthetic materials. The larger percentage of stress relaxation and dissipation area observed in the tissue reflects its superior capacity to dissipate energy and adapt under sustained loading conditions, characteristics crucial for biological functionality.

Overall, among the tested formulations, the silicone with a 10:1:5 ratio displayed the closest linear modulus and mechanical behaviour to the porcine tissue.

4.2.3.3 Discussion and conclusion

The progression of the stress-strain curves with increasing deadener weight ratio in silicone samples reflects the impact of formulation on material properties. While increasing the deadener ratio enhances the silicone's flexibility and reduces stiffness, it remains insufficient to fully replicate the soft, highly compliant behaviour of intestinal tissue. Also, The observed differences in stress relaxation further highlight the limitations of silicones in mimicking tissue dynamics. Biological tissues, like the intestine, are optimized for energy dissipation and adaptability, which are difficult to achieve

with homogeneous polymer systems. These limitations have implications for designing biomimetic substrates, particularly for applications requiring close emulation of tissue mechanics, such as in biomedical implants or surgical simulators. This suggests that further modifications, such as incorporating additional viscoelastic modifiers or using hybrid materials to create layered structures similar to biological tissue, may be required to bridge the gap between synthetic and biological performance.

The final decision was to choose use the ratio of base, catalyst, and deadener in the 10:1:5 weight ratio for the silicone formulation for subsequent testing, balancing the need for mechanical similarity with material manufacturing considerations. While it does not fully replicate the tissue's viscoelastic properties, it offers a reasonable approximation for applications where exact replication of biological mechanics is hard to achieve.

4.3 Initial testbed validation tests

This section primarily explores the use of experimental methods to validate the stability of each component of the test bench during the experiment. It also examines whether the design concepts of the various components meet the experimental requirements, and identifies any potential issues in the overall experimental process that could be improved.

4.3.1 Initial design of friction testing methodology

All components were assembled on the UMT to simulate the friction behaviour between the capsule robots and small intestines in the open state, as shown in 4.5. The capsule prototype was clamped by the UMT holder, integrated with the sensor for real-time synchronous measurement and data recording and the tissue holder was fixed on the platform of the linear drive to enable relative motion between the capsule and the tissue.

To study the general friction behaviour, a programmed reciprocating linear motion method was employed to simulate the sliding interactions between the capsule and the small intestine. When the capsule came into contact with the tissue surface, it gradually descended until the loading force increased to the desired value. The

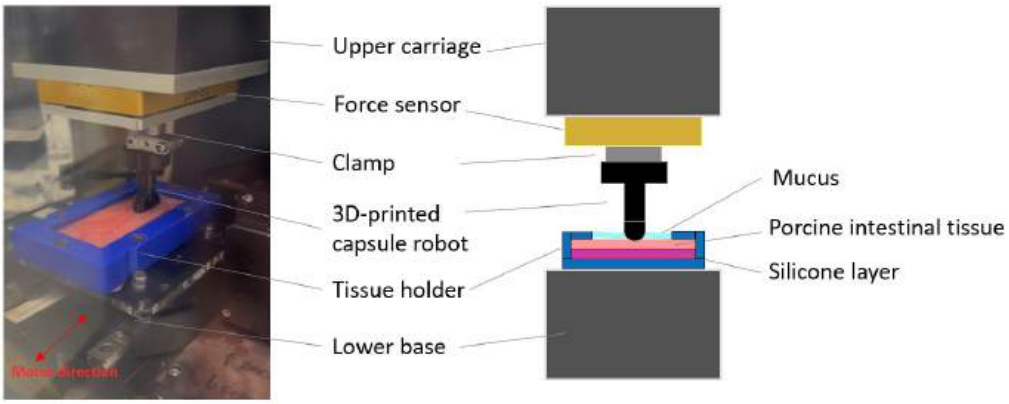

Figure 4.5: Photo and schematic diagram of the complete setup of the UMT-TriboLab friction testbed.

UMT machine was operated in displacement control mode, meaning the vertical position of the capsule was held constant throughout the sliding process. This approach aimed to capture the influence of tissue accumulation on frictional behaviour during the stick-slip phenomenon throughout the sliding phase while the load force could maintain relative stable. Once the loading phase was complete, the capsule slid at a constant speed until the sliding distance was covered and then stopped. Afterward, the sliding direction was reversed, and the capsule followed the same path, returning to the starting position. 20 reciprocating cycles were performed on each path to verify the consistency and validity of the method. Based on the width of the specimens, 3 sliding paths were selected for the experiments for each specimen. A sliding speed of 5 mm/s was selected, as peristalsis in the small intestine can move at speeds of 5–20 mm/s [125]. A normal load of 0.5 N, slightly greater than the typical commercial weight of CE robots, was chosen to simulate the larger force effect caused by hoop stress from intestinal movements, such as peristalsis, that would be applied to both the capsule and the tissue [36]. Mucus was prepared by mixing unpurified porcine gastric mucin powder (Mucin Type II, Sigma-Aldrich) at a concentration of 5 mg/ml with deionized water, to more realistically simulate intestinal juice. A total of 10 mL of mucus was added to the holder, as this amount was determined to provide sufficient coverage of the tissue. The sliding distance was set to 30 mm to collect sufficient friction data for analysing friction behaviour.

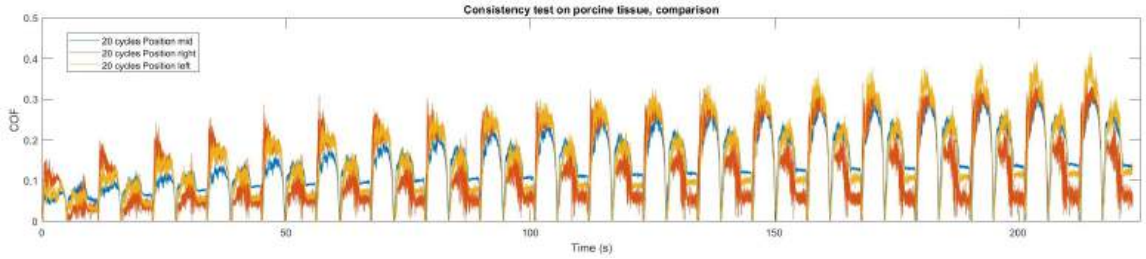

(a)

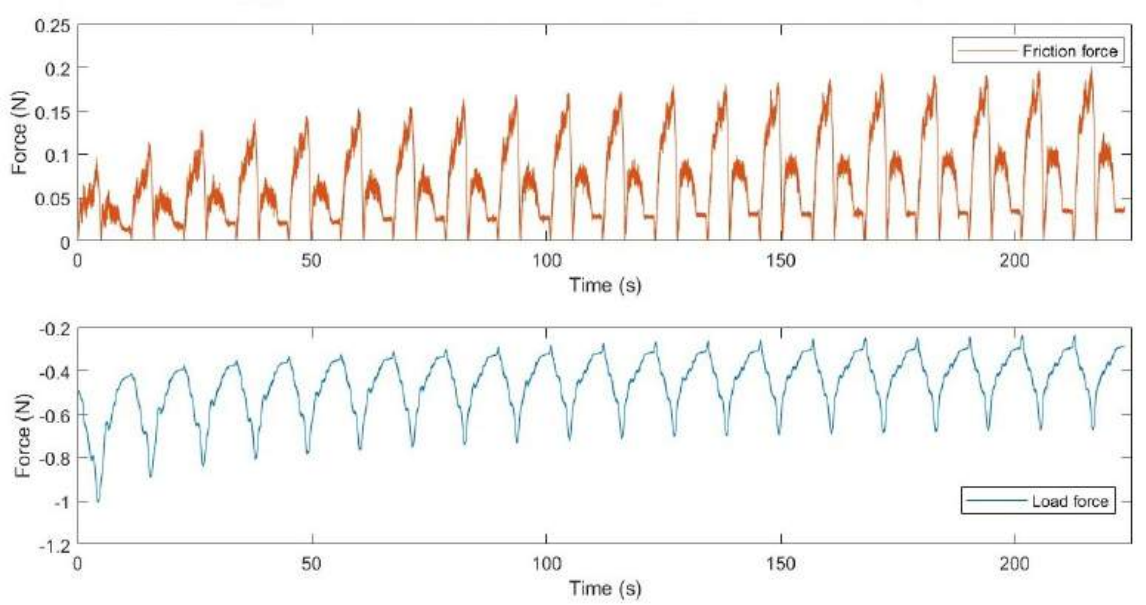

(b)

Figure 4.6: (a) Typical coefficient of friction (COF) results over 20 cycles across three tests. (b) Typical results of the load force and friction force for a single test. The negative sign of the force value merely indicates the direction of the applied force; The absolute value of the load force is the true magnitude of the force experienced during the experiments.

4.3.2 Results

The results of the coefficient of friction, friction force, and normal load measured during 20 sliding cycles were directly generated by the software of UMT, to provide valuable insights into the tribological behaviour of the system, as depicted in Figures 4.6 and 4.7. Both the COF and friction force increased as the number of reciprocated cycles progressed. In particular, the forward motion consistently produced higher values for both COF and friction force compared to the backward motion. The normal load exhibited significant variation during sliding, rather than remaining constant as initially set up. It also increased during forward motion and decreased during backward motion. However, the overall trend showed an upward shift in the normal load which meant the load force at the same location decreased over successive cycles.

These unusual variances can be ascribed to tissue abrasion and deformation. During forward motion, high friction between the capsule and tissue surface (resulting in a high initial COF) reduced relative motion. As a result, the tissue continued to fold in front of the capsule's travel direction, and the superficial layers of tissue were even separated from the deeper layers due to friction, causing an increase in resistive friction force. In backward motion, both COF and friction force decreased as the tissue surface became smoother compared to the forward motion. This was due to the majority of tissue and circular folds being stretched or damaged, and the reduction in tissue stretching as the tension recovered, which resulted in lower friction during the return motion. During successive cycles, as the tissue undergoes repeated abrasion, its surface becomes rougher. Additionally, repeated loading causes the tissue to become stiffer, further impeding capsule movement and increasing resistance.

The variation in normal load reflects the changing geometry of the tissue as it undergoes compressive forces during sliding. Since the vertical position of the capsule remained unchanged during sliding, the interaction between the tissue and capsule involved significant deformation, with increasing folds indirectly affecting the interaction. As the tissue structure thinned and compacted with each cycle, the load force at the same location decreased, which would typically reduce friction if COF was supposed unchanged. However, despite this, both the friction force and COF increased, indicating that the combined effects of tissue abrasion and stiffening had a larger impact on friction, ultimately increasing the overall resistance to motion.

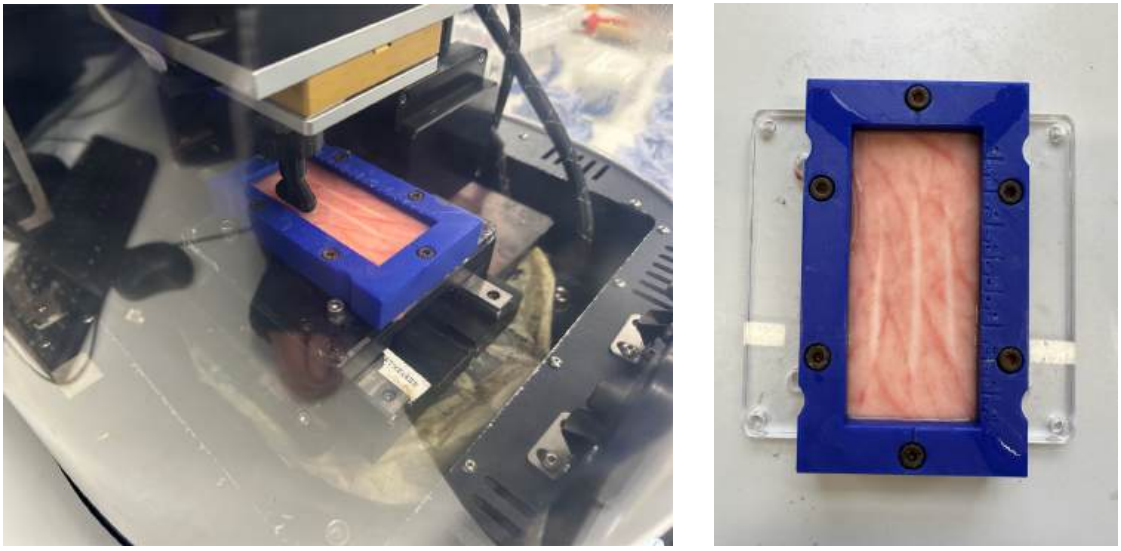

Figure 4.7: Wear scars were observed during the test.

4.3.3 Discussion

Based on the data and the previous analysis, it can be concluded that the methodology did not achieve the intended goal, which was to realistically simulate the friction environment between the small intestine and the capsule robot. The irreversible damage observed on the small intestine tissue, as well as the lack of consistency in the experimental data, which showed changing, unstable trends, suggest that the roughness of the capsule surface was too high and did not align with the real-life conditions. Therefore, improving the smoothness of the capsule surface is essential.

Additionally, the experimental method used for the capsule's reciprocating motion on the small intestine tissue does not accurately replicate the capsule's unidirectional movement in the small intestine. Although the original idea of using reciprocating motion was to obtain more friction data within a shorter experimental time, the results revealed that reverse motion influenced the stress response of the tissue and increased the risk of abrasion. This load response also corresponds to the stress–strain behaviour discussed in Chapter 3, as the ex vivo tissue does not fully recover within the limited time frame between successive loading events. This aspect of the experimental method should be revised. Furthermore, the use of displacement control mode on the UMT, which fixed the capsule's vertical position at an initial normal load of 0.5 N with the expectation that the resulting contact force would remain relatively stable and could better reflect frictional variations associated with stick-slip events,

did not yield the anticipated stability in force results. The load force on the capsule fluctuated significantly, which made it difficult to apply the controlled variable method in subsequent research on other factors. Consequently, it was challenging to determine whether the observed changes in experimental data were due to other factors or abnormal load fluctuations.

The experiment also revealed some issues with the designed equipment that could be improved. Regarding the capsule prototype, if the only modification needed is a change in the capsule size, it would require reprinting the entire structure, which wastes materials. Therefore, a more rational approach would be to design the capsule and the upper connection device as separate components. This would not only make it easier to replace the capsule but also streamline the process. Besides, improvements are needed for the tissue holder. Firstly, while the holder performed well in securing tissue for mechanical property testing, as it did not involve lateral forces, its fixation performance in friction tests was inadequate. In multiple instances, the tissue would detach from the boundary fixation and became loose during the friction testing, resulting in the inability to collect valid data. Secondly, during the experiment, mucus leakage was observed, likely due to the thinness of small intestine tissues and the relatively long duration of the experiment. The simple clamping structure sometimes failed to provide a good seal, leading to leakage and potential contamination of other equipment. Thirdly, the process of adding mucus with a syringe before the experiment was complicated by the insufficient depth of the bathtub, making it difficult to add the mucus effectively. These design issues should be addressed in future iterations.

4.4 Improvements of the methodology

This section introduces the improved design of the testbed components and the associated testing methods. All technical drawings of each component are provided in Appendix D.

4.4.1 New design of the capsule prototype

As analysed previously, a detachable design of the capsule prototype allows for more flexibility (Figure 4.8). The simulated capsule robot is detachable from the capsule holder. The upper part of the capsule holder retains a similar design to the previous model. The disc with 30-degree divisions allows the capsule to be oriented in different

directions, with the option for further small-angle divisions to be modified and manufactured based on specific requirements. The lower part has been redesigned with a clamp shape, where the cylindrical extrusion of the capsule robot is flat and aligns perfectly with the clamp's boundary, ensuring that the capsule remains parallel to the horizontal plane during tests. The internal locking mechanism, allows a nut to be placed into the hollow part of the capsule, which can be securely tightened with a bolt that penetrates the probe holder. This design prevents unwanted slippage, tilting, or vibration that could otherwise affect the test results. Since the capsule holder does not require fine surface details, the probe holder was 3D printed using PETG.

Figure 4.8: Images include the probe holder, schematic drawings in exploded view, and cross-sectional views.

Based on the size specifications of commercial products from Table 2.1, several capsule prototypes were manufactured with diameters ranging from 10 to 12 mm and lengths from 26 to 32 mm, as these sizes cover the majority of clinical applications. Instead of using 3D filament (FDM) printing with PETG, resin 3D printing was employed, as it offers higher print quality and smoother surfaces. SLA 3D printers (Form 3+, Formlabs) operate by curing light-reactive thermoset materials (resin) using specific wavelengths of light, a process that polymerizes monomers and oligomers, forming rigid or flexible solid geometries. The SLA printer can achieve extremely fine details, with layer heights as thin as 25 microns from the product data-sheet. In contrast, FDM printing typically offers lower resolution, with layer heights ranging from 100 to 300 microns, leading to more visible layer lines and increased surface

roughness. The capsules were printed using Grey Resin (Formlabs), primarily composed of urethane dimethacrylate and methacrylate monomer. With a finer surface finish, the average surface roughness was measured to be 8.5 µm.

The overall design ensures that the simulated capsule closely matches that of the actual product. Although surface roughness data for commercial products is unavailable, the friction results presented later demonstrate that no significant damage was caused to the tissue during sliding, thereby enhancing the realism and effectiveness of the experimental simulation.

4.4.2 New design of the tissue holder

A new tissue holder with tub-like structure was designed to meet the previous requirements without any leakage issues, thus preventing contamination (Figure 4.9). Building on the previous design, a double-layer structure was also adopted, with tissue placed on the silicone base to simulate the intestinal environment. To prevent the tissue from slipping during the experiments and to provide a certain amount of tension, rectangular frames or bars with grooved contact surfaces (depending on the tissue size), secured with bolts, were used to firmly fix the tissue in place. The holder can accommodate tissue with a maximum size of 60 mm by 105 mm. Only the central region of the tissue was selected for the friction test to minimize boundary effects caused by the restraints, which could strengthen the tissue. The tissue holder was initially 3D printed using PETG, and later an aluminum alloy version was machined for improved durability.

4.4.3 New friction test methodology

The whole set up of the testbed is shown in Figure 4.10.

A programmed unidirectional test cycle was employed to simulate the capsule-small intestine sliding interactions and minimize excessive abrasion. Figure 4.11 illustrates the test steps. In Step 1-2, the probe lowered at a slow speed of approximately 0.2 mm/min after detecting contact, and the applied load was gradually increased to the desired value. The capsule then remained stationary for 10 seconds to allow for force stabilization. Step 2-3 depicts the sliding motion, where the capsule quickly accelerated and slid at a constant speed over a 30 cm distance before

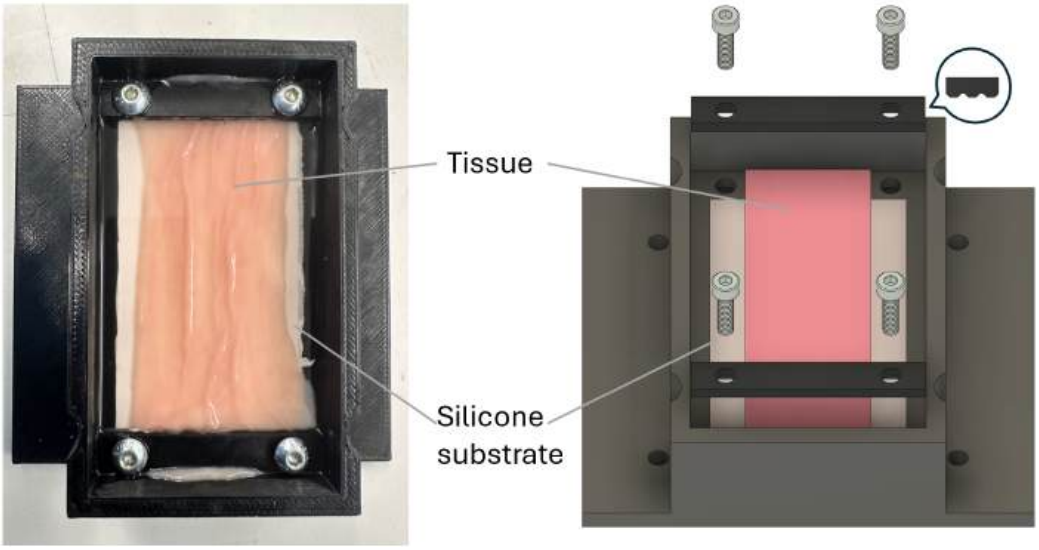

Figure 4.9: Image of the tissue holder and an exploded view schematic drawing.

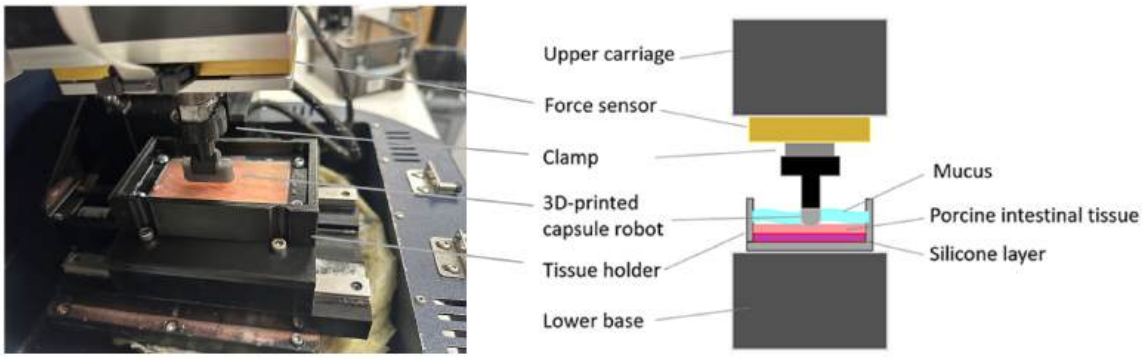

Figure 4.10: Photo and schematic diagram of the complete setup of the new testbed.

stopping. During sliding, the load control function of the UMT machine was used to automatically adjust the normal load to a certain value, preventing large fluctuations. In Step 3-4-1, after completing the sliding test, the probe lifted and returned to the starting position, preparing for the next cycle. Consistency tests were performed on three samples, with each sample tested on 3 sliding paths, and each path was spaced at least 12 mm apart to ensure that different sliding paths did not overlap. A marker pen was used to mark the capsule's starting position, allowing for easier comparison of any friction damage to the tissue before and after the tests. Each path underwent 10 cycles to assess the results. All test parameters, including sliding speed and initial normal load, were kept the same setting in previous tests. The capsule size was selected to match the same dimensions, and the mucus used was of the same type and mucin concentration as in the first testbed validation test.

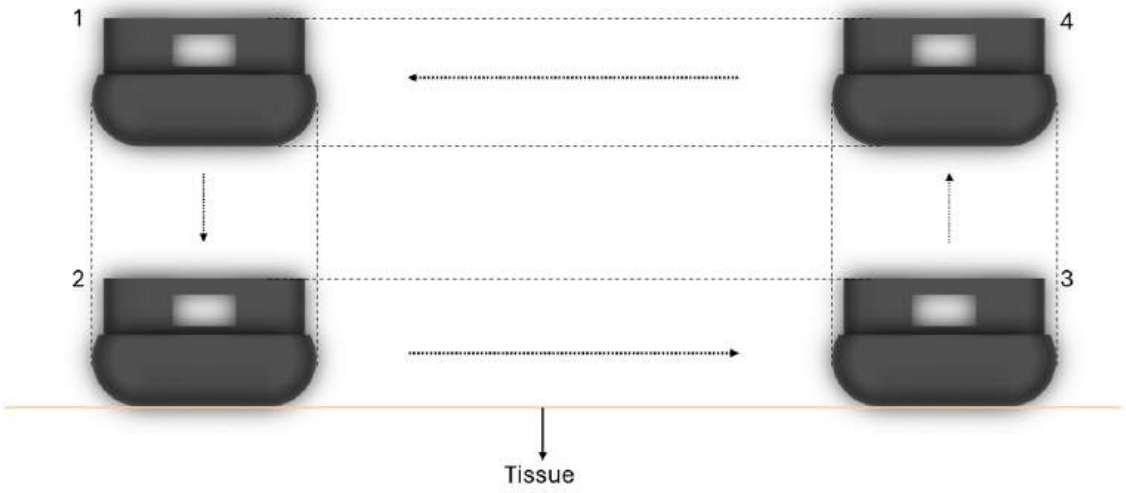

Figure 4.11: A schematic diagram of the unidirectional test cycle.

4.4.4 Results

Figure 4.12 presents the typical results of the first four cycles of normal load, friction force and COF versus time in each single graph to directly compare the differences between each cycle. A more enlarged and distinct graph is appended in Appendix E. It can be observed that the fluctuations in normal load are relatively small, and the irregularities reflect the normal folding and crossing phenomena during the sliding motion. In addition, for friction force and COF results, it is evident that the cycles begin to converge after 2 or 3 cycles, showing strong consistency, as the results nearly align with each other. Moreover, Figure 4.13 further suggests that no visible friction damage was observed with a normal load of around 0.5 N, as indicated by the comparison of the figures' differences. These phenomenons were observed in all 9 tests across 3 different samples, indicating that the friction results after the third cycle are reliable and can represent the typical response to sliding.

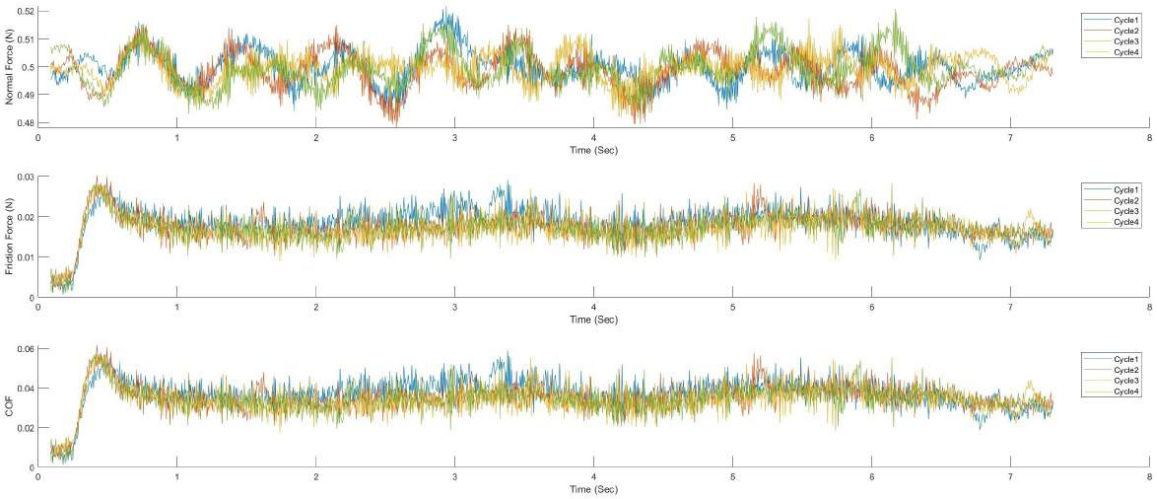

Figure 4.12: From top to bottom, the sliding results of the first four cycles for normal load, friction force, and COF values are shown from the consistency tests.

4.4.5 Discussion

The results presented in Figure 4.12 and Figure 4.13 highlight the successful validation of the testbed, confirming that it is now capable of accurately assessing the friction interactions between the capsule robot and intestinal tissues. The observed consistency in the data, particularly after the third cycle, indicates that all previous issues regarding instability and inconsistency have been resolved, providing reliable results that can maximumly reflect real-world interactions.

One of the main challenges identified in earlier testing was the inconsistency in the normal load, friction force, and coefficient of friction, which made it difficult to draw reliable conclusions about the capsule's performance. However, the current results show significant improvement as illustrated before, indicate previous issues were solved with the new experimental setup. Most notably, the friction force and COF values begin to converge after two to three cycles, demonstrating a high degree of consistency. This convergence and near alignment of frictional values mark across multiple cycles a key milestone, confirming that the system has stabilized and can now consistently replicate results under controlled conditions.

Another significant improvement observed in the experiment was the absence of visible friction-induced damage to the small intestine tissue when a normal load of approximately 0.5 N was applied, as shown in Figure 4.13. In previous iterations, excessive loading or improper surface characteristics of the capsule led to damage

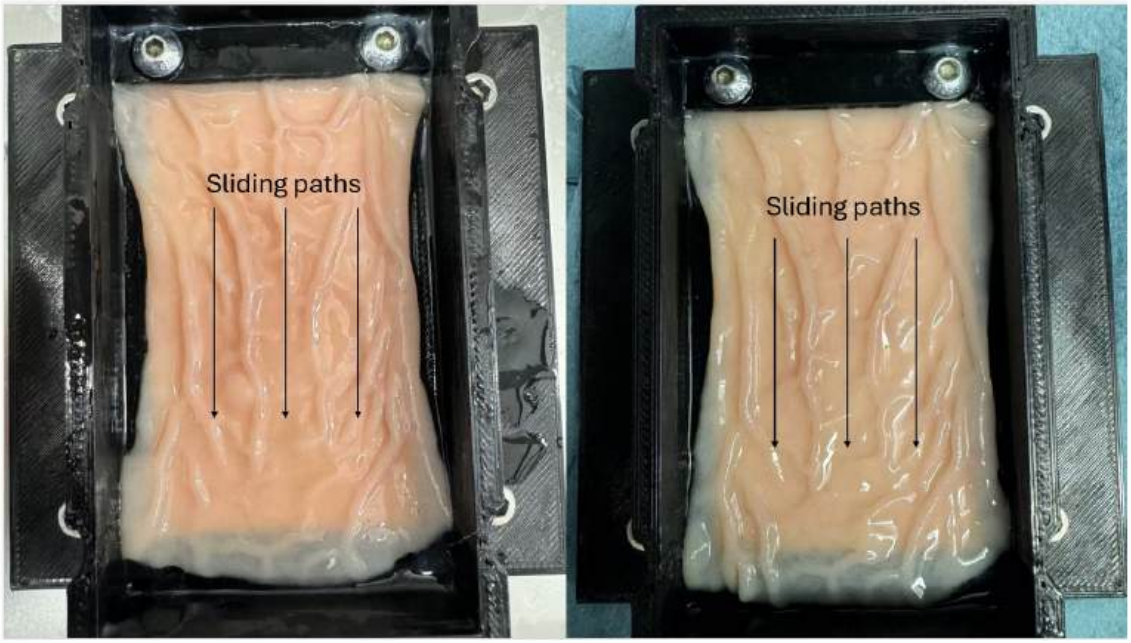

Figure 4.13: Photos were taken before (left) and after (right) friction tests to compare the difference.

and irregularities, which compromised the integrity of the tissue samples. However, the current results suggest that the capsule's design and the experimental conditions are now optimized to prevent such damage, allowing for a more accurate simulation of real-world conditions. This improvement is critical for ensuring the safety and effectiveness of capsule robots in medical applications.

The reliability of the test bench is further demonstrated by the consistent results obtained across all nine tests conducted on three different tissue samples. This reproducibility indicates that the test bench is robust and capable of handling variability in biological materials, which is a key requirement for any experimental setup intended for real-world medical research. The fact that all tests showed similar results after the third cycle suggests that the bench is validated and can be confidently used to assess the frictional interactions between capsule robots and intestinal tissues in a variety of experimental conditions.

The consistent performance observed in this set of experiments validates the test bench's design and operational efficiency. All previous problems, including inconsistent results, improper motion dynamics, and capsule surface roughness issues, have been addressed. The improvements to the capsule's surface smoothness, motion mech-

anism, and load control have proven effective in producing consistent and accurate results, validating the test bench as a reliable tool for studying capsule robots and their interactions with intestinal tissues. This platform can be used to explore a range of factors influencing the frictional behaviour, including varying capsule surface textures, different intestinal tissue conditions, and alternative motion patterns. Moreover, the ability to simulate real-world conditions in a controlled and reproducible manner will enable the development of more effective capsule robots, optimizing their design for medical applications such as drug delivery, diagnostic procedures, and minimally invasive surgeries.

While this test platform was primarily developed to investigate the frictional interaction between capsule robots and small intestinal tissue, its underlying methodology demonstrates broader applicability to the study of soft tissue–device interactions in general. This potential has been exemplified in a collaborative project with researchers from TU Delft, in which the platform was adapted for an ex vivo validation study evaluating the performance of ultrasonically-lubricated catheters [126]. In this study, porcine aorta tissue was used to assess the reduction in sliding friction achieved through ultrasonic actuation. The successful adaptation of the platform in this context underscores its versatility and value in assessing the tribological behaviour of various medical devices across different soft tissue environments. However, caution is warranted when generalizing the results due to fundamental differences between the ex vivo test setup and actual in vivo tribosystems. Factors such as tissue perfusion, active peristalsis, mucosal secretion dynamics, and physiological temperature are absent in ex vivo environments but significantly influence in vivo frictional responses. Additionally, the current test platform primarily simulates linear motion under simplified loading conditions; more complex interactions such as rotational forces, multi-axial stress states, and long term cyclic loads require platform refinements. Future development of biomimetic testbeds that more accurately replicate in vivo boundary conditions and dynamic tissue responses would be critical to extending this framework's validity and utility across various biomedical applications.

4.5 Conclusions

The successful resolution of previous experimental challenges and the consistent, repeatable results obtained in a series of tests confirm that the methodology with the

designed testbed for accessing the friction interactions between the CE robot and intestinal tissue is fully validated.

Although a marginal disparity persists between the silicone and porcine intestinal tissue in the indentation tests, the silicone utilized as the lower substrate was manufactured with a base:catalyst:deadener weight ratio of 10:1:5, due to its mechanical characteristics being the most proximate to those of the animal tissue.

This study demonstrates the versatility of the developed test platform for evaluating soft tissue–device interactions beyond capsule endoscopy, as shown in its successful application to ultrasonically-lubricated catheters. However, limitations of ex vivo testing, such as the absence of physiological conditions highlight the need for future enhancements. Incorporating biomimetic features and complex loading scenarios will be key to extending its relevance to in vivo applications.

Chapter 5

Friction tests: Mucus

5.1 Introduction

The interaction between the capsule robot and the intestinal wall generates frictional forces that can hinder its movement and reduce diagnostic efficiency. Intestinal juice, secreted by epithelial cells of the small intestine, plays a critical role in digestion. This slightly alkaline fluid contains bicarbonates that neutralize the acidic chyme discharged from the stomach, creating an optimal environment for digestive enzymes. Additionally, intestinal juice is rich in mucus, which provides essential lubrication, facilitating the smooth passage of chyme through the intestines while protecting the intestinal walls from mechanical damage and enzymatic activity.

The work described in this chapter aims to analyse the lubrication effect of mucus on capsule endoscopy movement, a topic not extensively addressed in previous research. Friction tests were also conducted using PBS as a control group. Furthermore, this research investigates how variations in mucin concentration, pH, and mucus viscosity influence friction and lubrication performance. By systematically examining these factors, the study offers insights into the role of mucus properties in reducing friction and underscores their importance in optimizing capsule endoscope design, improving patient comfort, and enhancing diagnostic outcomes.

5.2 Materials and method

5.2.1 Tissue preparation

The detailed tissue preparation process is described in Section 3.2.1. One key difference was that the time required to complete the friction test was significantly longer than the mechanical properties tests due to the larger number of variables examined. As a result, it was challenging to complete the entire schedule, including tissue acquisition, transportation, preparation, and testing within 5 to 7 hours on the same day. To address this issue, a method for tissue storage was developed based on previous studies [127]. After excising the tissue to the size suitable for the tissue holder, it was spread out as much as possible, wrapped in a blue roll and sprayed with PBS solution to retain moisture and preserve the surface structure. The tissue was then sealed in a sterile plastic bag and stored in a freezer at -80°C to retain the original condition of the live intestine as much as possible (Figure 5.1a). When it was time to conduct the experiment, the tissue bag was placed in a room-temperature water bath (Figure 5.1b). Once thawed, the tissue was removed from the bag and immersed in PBS solution in preparation for the experiment. For consistency, all tissues were used within a week of slaughter, with experiments conducted on the same day. Degradation was assumed to occur uniformly across all samples.

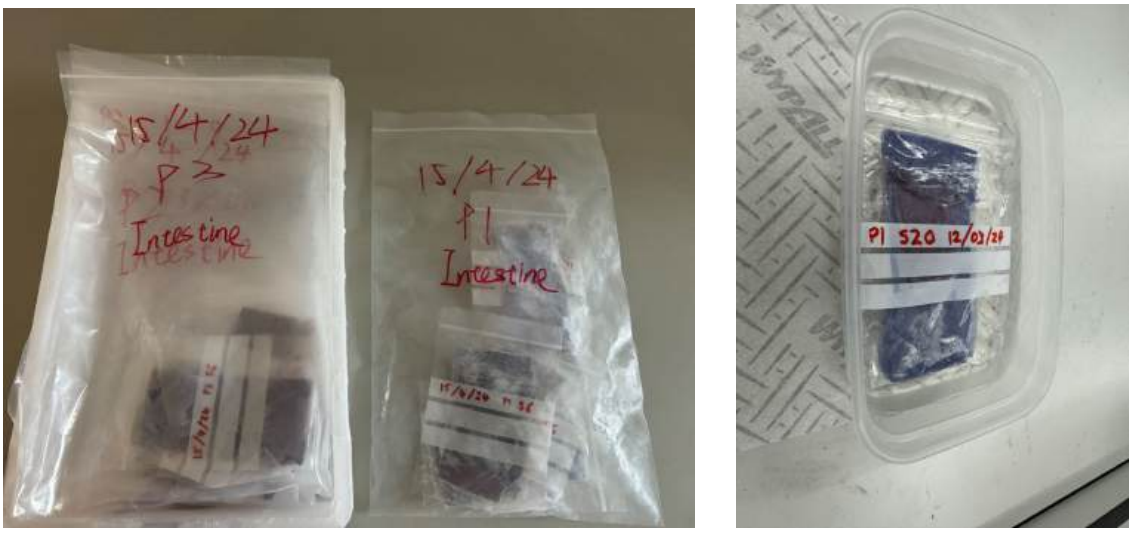

(a) (b)

Figure 5.1: (a) Tissue samples were marked with the slaughter date and stored in the freezer. (b) The tissue was thawed using a water bath.

5.2.2 Mucus preparation

Mucus was prepared using unpurified porcine gastric mucin powder (Mucin Type II, Sigma-Aldrich), providing a more realistic representation. To achieve the desired mucin concentrations, the powder was gradually placed in a weighing boat and weighed using a balance, with the error controlled within ±0.005g (Figure 5.2a). The measured powder was then transferred into a clean glass bottle containing the appropriate amount of deionized water. A magnetic hotplate stirrer was used to heat the solution to 36.5°C and assist with mixing (Figure 5.2b). After approximately 30 minutes of mixing, the bottle was transferred to a pH meter. Sodium hydroxide (NaOH) solution was gradually added to adjust the pH to around 7.5, which is close to the pH of intestinal juice (Figure 5.2c). Finally, the mucus was transferred to a water bath machine set to maintain a temperature of 36.5°C to simulate body temperature conditions in preparation for the experiment (Figure 5.2d). Due to the limited information available regarding the mucin concentration of human intestinal juice, mucus solutions with concentrations of 1, 5, 10, and 15 mg/ml were prepared (Figure 5.2e). It can be observed that increasing the mucin powder concentration caused the solution to become darker and more turbid.

5.2.3 Test method

The friction test procedure followed the established methodology 4.4. After placing the tissue onto the tissue holder and setting up all components (a capsule prototype with a diameter of 12 mm and a length of 28 mm was used), the same loading-sliding-return cycle was applied to obtain the friction results as previously described. Based on the conclusion that tissue response converges after 3 cycles, a total of 6 cycles were performed on the same sliding path and only the data from cycles 4 to 6 were averaged and analysed at a sampling rate of 200 Hz. The normal load, sliding speed, and sliding distance were set at 0.5 N, 5 mm/s, and 30 mm, respectively, as before.

To study the lubrication effect of mucus, with a focus on the effects of mucin concentration and solution pH, mucin concentrations ranging from 1 to 15 mg/ml (all adjusted to a pH of 7.5) were tested. Additionally, 5 mg/ml mucus was divided into three portions, the original pH level of the mucus was 3.71, then the other two portions with pH levels adjusted to 6.0 (which is the pH level at duodenum), and 7.5 (which is the pH level at ileum) for testing [128]. All other testing parameters were

(a)

(b)

(c)

(d)

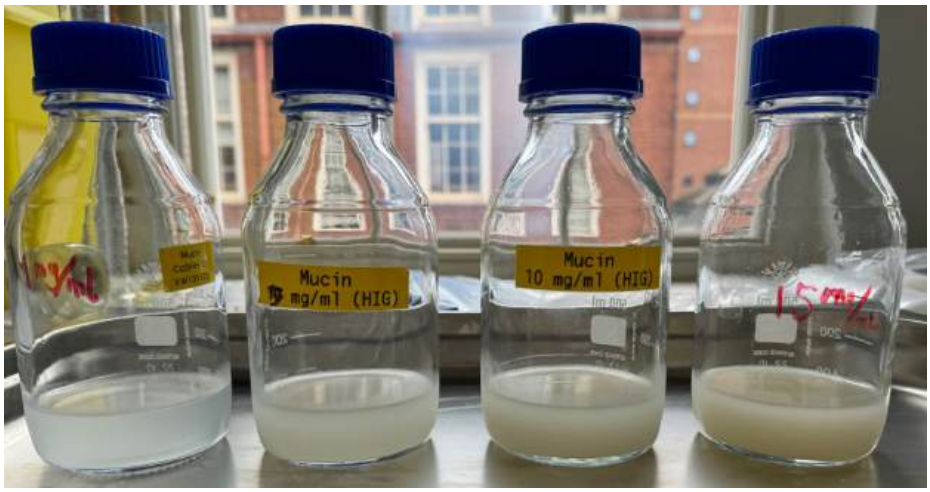

(e)

Figure 5.2: (a) Mucin powder being weighed in a weighing boat. (b) Mucus solution was mixed using a magnetic hotplate stirrer. (c) A pH meter was used to adjust the pH of the mucus solution. (d) A water bath machine was used to kept prepared mucus solution at 36°C. (e) Mucus solutions made with different mucin concentrations.

kept consistent to control for variables. For each test, 10 ml of mucus solution was added into the tissue holder using a syringe. At least 3 samples were tested, with a minimum of 9 tests performed for each study objective. After each test, a visual inspection of the tissue was conducted to assess the damage caused by friction.

Additionally, the viscosity of mucus of each mucin concentration and pH was measured using the HR-10 rheometer (TA Instruments). Mucus was squeezed into the cone-plate gap, and viscosity and shear stress data were measured and recorded as the shear rate increased at the same body temperature (36.5 °C). Each type of mucus was tested with at least 4 mucus samples, and the results were averaged for analysis.

Figure 5.3: Viscosity of each mucus type versus shear rate was measured by using the rheometer.

5.2.4 Data analysis

Figure 5.4 depicts the general friction results of the COF from the last three sliding cycles. COF was used because it took into account fluctuations in normal load and friction force, and provided data that was more suited to comparative analysis.

To present the data more concisely and clearly, instead of listing individual charts and averaging the curves, and then pasting them onto a single chart for direct comparison as done in the mechanical property testing chapter, the experimental data

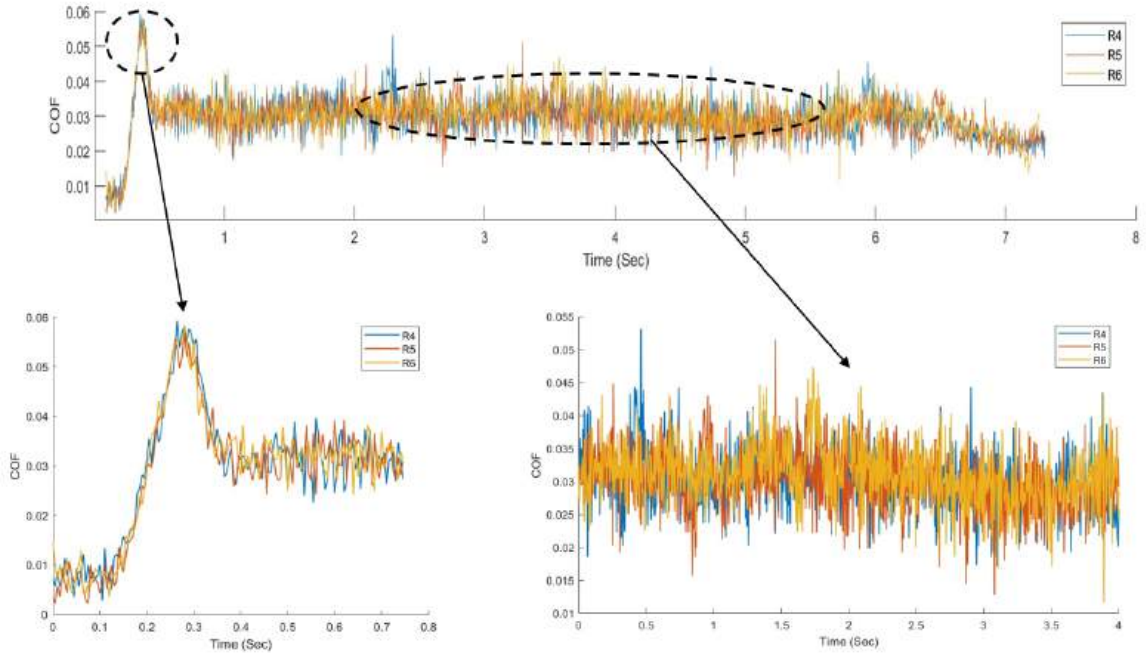

Figure 5.4: General friction results: COF versus time curves for the last three sliding cycles, including the static friction peak and dynamic friction region.

would be presented using bar charts showing the average COF values and standard deviations for each research objective. This approach was chosen because, although different parameters were used for each study objective, the friction curves did not differ significantly and tended to overlap, making it difficult to distinguish between them. Additionally, there were numerous small fluctuations in the curves, and for some data points, the peaks and valleys would concentrate and stack together, leading to an amplification effect that could compromise data accuracy and authenticity.

The friction results were separated into static and kinetic COF values, as they represented different friction characteristics. As shown in the figure, the maximum static friction occurred at the highest value in the initial part of the curve. The median kinetic COF value was selected when the speed reached a steady state (typically a 4-second, 20mm sliding distance region). The values from each cycle were averaged, and the standard deviation was calculated for each test.

A decision framework was used to determine whether the data showed a statistically significant difference caused by study objectives (Figure 5.5). The process for comparing means across three or more groups under the same test conditions was

carried out using GraphPad Prism software (Insight Partners), with statistical tests such as the Kruskal-Wallis test (a non-parametric test) or the one-way ANOVA (a parametric test) depending on the results of normality and variance tests. The level of statistical significance was set to $P < 0.05$. If a statistically significant difference was detected, post-hoc analysis was conducted to identify which specific groups differ. Additionally, the framework emphasized performing power analysis using GPower software (Heinrich-Heine-Universität Düsseldorf) to determine the sample size needed for adequate detection of significant effects, ensuring robust results in hypothesis testing [129].

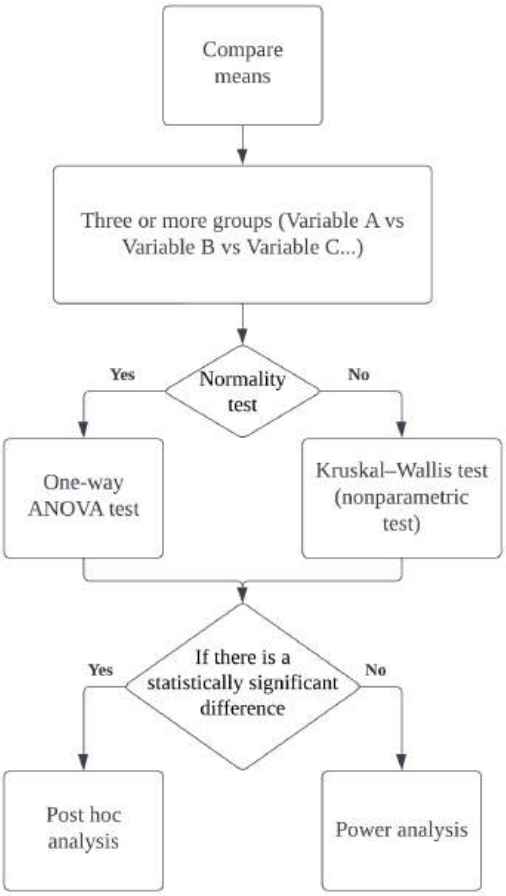

Figure 5.5: Decision framework for data analysis of friction data.

5.3 Results

In this study, the effect of mucus with various mucin concentrations and pH on the frictional resistance between the simulated capsule robot and porcine intestinal samples was evaluated under static and kinetic conditions (Figure 5.6). Box-and-whisker plots were used to visualize the distribution of COF values and compare variables. These plots display the median, quartiles, and outliers, providing insights into the influence of these variables on COF. Descriptive statistics tables were provided in Appendix F.

Figures 5.6a and 5.6b illustrate the distribution of COF values under static and kinetic conditions for mucus prepared with various mucin concentrations, including 1 mg/mL, 5 mg/mL, 10 mg/mL, and 15 mg/mL, along with a PBS control group. The test results indicated no significant differences in COF values across mucus samples with different mucin concentrations, suggesting that mucin concentration did not significantly affect the COF under static or kinetic sliding conditions. Both conditions showed considerable data points variance across and within groups, with a range of approximately 0.1. This variance led to observations where some COF values in one group were larger than those in another, while others were smaller, with no consistent pattern. A downward trend in the median bar locations suggested that COF might decrease with increasing mucin concentration, although statistical analysis showed that this trend could not be confirmed with sufficient confidence. To compare the lubricating effect of mucus, friction tests with PBS solution were performed, but no clear difference was verified, and the results were similar to those of 1 mg/mL mucus. Overall, the friction tests showed that the average COF with mucus as a lubricant was 0.0691 in the static friction phase and 0.04799 in the kinetic friction phase.

For the pH effect of mucus on COF, the variance in data points and lack of significant differences were similar to the findings for mucin concentration. As the mucus solution became more neutralized, a trend emerged showing an increase in static COF values. However, this trend did not extend to the kinetic sliding phase, where COF values remained nearly identical across different pH levels. Overall, the mean static COF values for mucus with pH 3.71, pH 6.0, and pH 7.5 were 0.07376, 0.07447, and 0.07843, respectively, while the kinetic COF was around 0.049 across different pH.

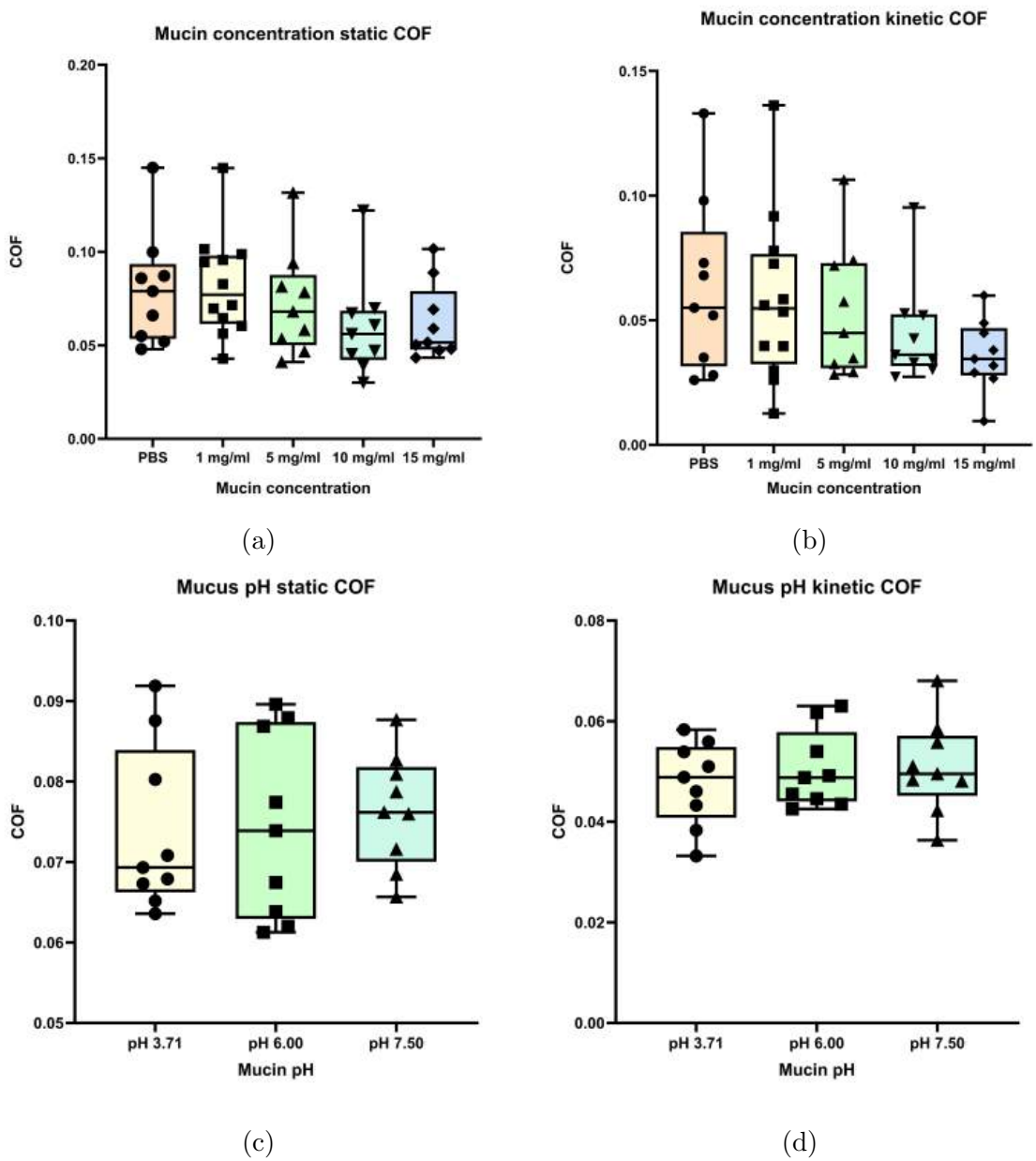

Figure 5.6: Friction results: Static and kinetic COF for different mucin concentrations (a),(b) and different pH levels (c),(d).

Since the results of the statistical analysis were non-significant, power tests were conducted to determine the probability of correctly rejecting the null hypothesis, which stated that changes in mucus pH or mucin concentration had no effect on COF, when the null hypothesis was false. Table 5.1 summarizes the results, presenting the power values alongside the recommended total sample sizes for each test type, providing an overview of the study's statistical strength. The power values of all tests were low, remaining below 0.8. Specifically, the likelihood of detecting

a true effect, if it existed, was 0.47 for static COF and 0.45 for kinetic COF when varying mucin concentrations. The power values for the mucin pH tests were even lower, at approximately 0.21 and 0.2 for static and kinetic COF, respectively. Given the non-significant results, it is likely that the sample size was insufficient to detect meaningful differences. The suggested sample sizes for a power of 0.95 for each test type were 170, 145, 357, and 375, respectively.

	Mucin concentration tests		Mucin pH tests	
	Static	Kinetic	Static	Kinetic
Power	0.40	0.42	0.21	0.20
Total sample size	170	145	357	375

Table 5.1: Power analysis results for the mucus tests.

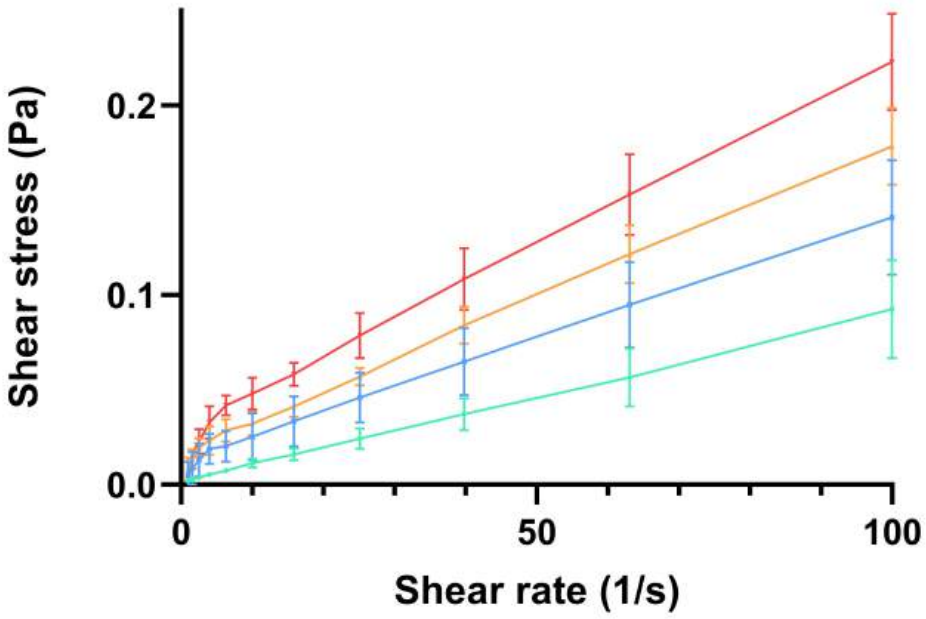

Figure 5.7: Shear stress versus shear rate results of mucus for different mucin concentrations.

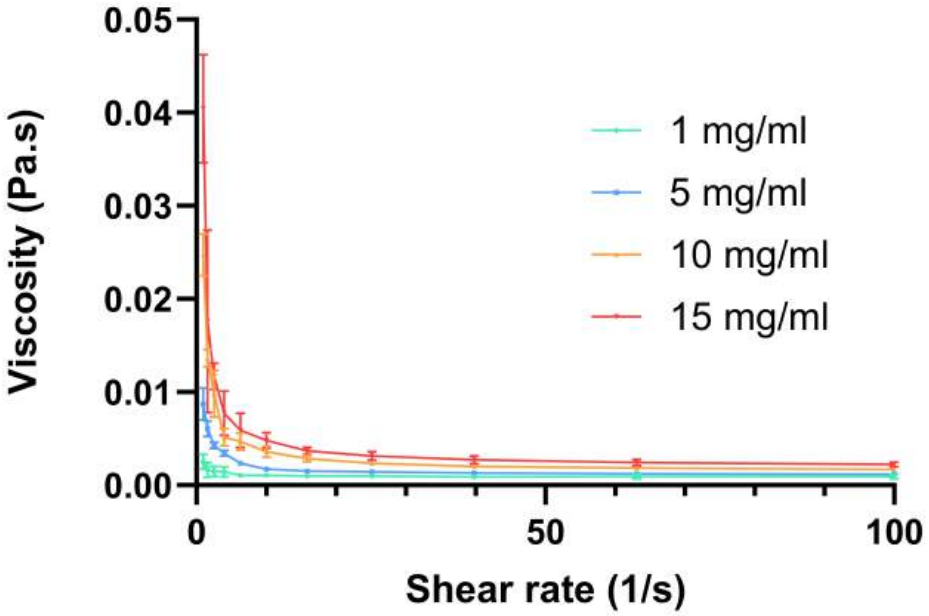

Figure 5.8: Viscosity versus shear rate results of different mucin concentrations.

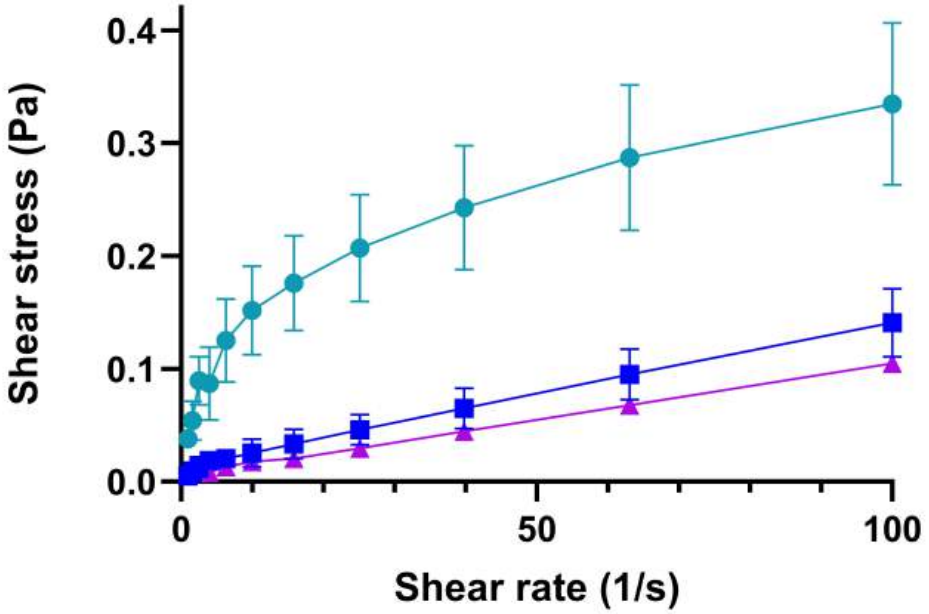

Figure 5.9: Shear stress versus shear rate results of mucus for different pH levels.

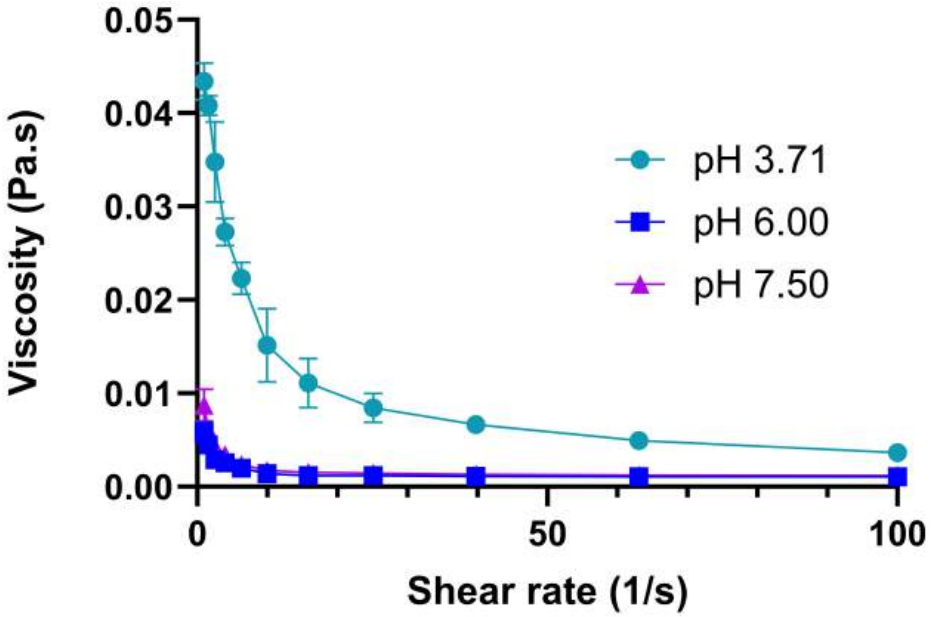

Figure 5.10: Viscosity versus shear rate results of mucus for different pH levels.

The graphs illustrate the changes in viscosity and shear stress across different mucin concentrations and pH levels of mucus during a shear rate sweep from 1 to 100 1/s (Figure 5.7, 5.8, 5.9 and 5.10). Overall, the mucus behaved like a typical non-Newtonian fluid behaviour. For mucus with varying mucin concentrations adjusted to pH 7.5, shear thinning behaviour was observed in the 1–10 1/s region. Beyond this range, from 10–100 1/s, the fluid exhibited more Newtonian behaviour. Additionally, higher mucin concentrations resulted in greater viscosity at every shear rate, with the curves consistently positioned above one another. Even though the viscosity at the shear rate of 1 1/s of each curve was very different (0.0025, 0.0087, 0.0247 and 0.0404 Pa.s), the final values became more concentric as the shear rate increased.

For mucus made with 5 mg/mL but at different pH levels, the original mucus with a pH of 3.71 (did not go through the neutralization process) displayed complete shear-thinning behaviour throughout the entire shear rate range from 1 to 100 1/s. In contrast, the curves for pH 6 and pH 7.5 were similar, showing shear-thinning behaviour only at low shear rates as mentioned above. Furthermore, the viscosity of the pH 3.71 mucus was significantly larger than that of pH 6 and pH 7.5 at shear rate 1 1/s (0.0434, 0.0087 and 0.0058 Pa.s), with a smaller decrease in slope as the

shear rate increased. The convergence of viscosity values at high shear rates was also observed in the mucus pH graphs.

5.4 Discussion

The results of this study provide significant insights into the influence of mucus composition, particularly mucin concentration and pH, on the frictional resistance between the simulated capsule robot and porcine intestinal samples under both static and kinetic sliding conditions. Despite observing trends and some variations in the data, the statistical analysis failed to demonstrate significant differences across the tested variables. This suggests that neither mucin concentration nor pH played a dominant role in influencing the COF under the tested conditions. The consistently low COF values indicate that the lubrication regime likely extends beyond classic lubrication regimes, pointing instead to alternative mechanisms. This discussion explores these findings in the context of lubrication theory and outlines key limitations of the study.

The classic Stribeck curve, commonly used to describe lubrication transitions, may not be entirely applicable in this case. As discussed in Chapter 3, intestinal tissue is extremely soft and highly permeable to water, which impedes the formation of a stable, pressurized fluid film required for hydrodynamic lubrication. In addition, the tested mucus solutions exhibited shear-thinning behaviour, characteristic of non-Newtonian fluids, whereas the Stribeck model assumes Newtonian behaviour, further highlighting its limitations in this biological context. Despite these constraints, fundamental lubrication principles can still guide interpretation of the low COF values. Given the low viscosity of mucus across all conditions, combined with moderate sliding speeds and normal loads, stable hydrodynamic lubrication is unlikely to occur all the time during sliding. Instead, the results are more consistent with boundary and hydration lubrication mechanisms. Mucin, the primary glycoprotein in mucus, is known to adsorb strongly onto biological surfaces, forming sterically and electrostatically repulsive interfaces that minimize direct contact and reduce friction at boundary layer [130]. More importantly, hydration lubrication likely plays a central role. Mucin increases surface hydrophilicity, allowing water molecules to form tightly bound hydration shells that act as lubricating layers and significantly lower interfacial shear resistance [131]. These mechanisms align with lubrication behaviour observed in other

physiological systems, such as tear film on the eye (COF around 0.05) and synovial fluid in cartilage (COF around 0.001) [132,133]. This lubrication mechanism may also explain why PBS showed no statistically significant difference compared to mucus, hydration lubrication can occur not only with macromolecules like mucin but also in the presence of hydrated ions, which are abundant in PBS.

The observed COF values in this study demonstrate the lubricating effect of mucus. Compared to previous studies that involved limited mucus presence, such as dry or minimally hydrated conditions, and reported kinetic COF values ranging from 0.1 to 0.32 [38,45,101], the current study recorded substantially lower average values (approximately 0.05). This suggests that even relatively dilute mucus layers can significantly reduce friction between the capsule and intestinal tissue.

The influence of mucin concentration was assessed across a range (Figure 5.6a). A general trend of decreasing COF with increasing mucin concentration was observed, particularly between the 1 mg/ml and 15 mg/ml groups; however, these differences were not statistically significant. This may be attributed to the relatively modest increase in apparent viscosity across the tested concentrations. While previous studies have demonstrated that viscosity increases with mucin concentration [134], the magnitude of this change in the current study was likely insufficient to form a full fluid-film lubrication regime as mentioned above. Higher mucin concentrations may promote greater adsorption of mucin molecules onto the intestinal tissue surface, enhancing lubrication via boundary and hydration mechanisms. This could explain the downward trend in friction values. Nevertheless, the small magnitude of these changes likely contributed to the lack of statistical significance. An additional explanation involves the shear-thinning behaviour characteristic of mucin solutions. While mucus samples with different concentrations exhibit distinct viscosities at low shear rates, the sliding motion during friction tests induces higher shear, which diminishes these viscosity differences and may reduce their impact on frictional outcomes. Furthermore, considerable variability within groups suggests that uncontrolled factors, such as tissue surface heterogeneity or inconsistencies in mucus preparation, may have exerted a stronger influence on frictional behaviour than the relatively small differences in viscosity.

pH-dependent changes in friction were also examined across pH levels of 3.71, 6.0 and 7.5. Slightly higher static COF values were observed at neutral pH, which

may be attributed to structural changes in mucin during neutralization. At acidic pH, mucins are more protonated and tend to form gel-like networks, promoting film stability and hydration-mediated lubrication. In contrast, neutralization may disrupt the mucin polymer structure or cause partial denaturation, resulting in reduced viscosity and inferior lubrication performance. However, similar to mucin concentration, the observed differences were not statistically significant. It is likely due to the modest pH-induced effects and a limited sample size insufficient to detect subtle changes, highlighting the need for future studies with larger experimental data to investigate this relationship more thoroughly.

Several limitations constrain the interpretation of the results presented in this study. First, the use of porcine gastric mucin (MUC2) as a surrogate for native intestinal mucus may not fully replicate the complexity of in vivo conditions. Native intestinal mucus contains a range of additional components, including lipids, ions, enzymes, and microbiota, that contribute to its rheological and lubricating properties. Second, the preparation method imposed constraints on the achievable mucin concentration due to solubility limitations, likely arising from the unrefined nature of the commercial mucin powder. At a concentration of 10 mg/mL, visible undissolved residues were observed, precluding the use of higher concentrations and limiting the ability to evaluate concentration-dependent effects. Furthermore, the artificial mucus layer used in this study is static and does not reflect the dynamic turnover, secretion, or enzymatic degradation processes that occur in vivo. This static model fails to capture the continuous renewal and complex biochemical interactions inherent to the gastrointestinal environment. Additionally, the viscosity of the prepared mucus solutions was lower than physiologically reported values (e.g., approximately 0.085 Pa·s at comparable shear rates, as noted by Lai et al. [84]), which may have reduced their ability to mimic natural lubrication behaviour. Although general lubrication effects were observed, the weak correlation between viscosity and COF, as well as the modest effect sizes, suggest that future studies should aim to incorporate more physiologically accurate mucus models and test conditions to better elucidate the role of mucin in gastrointestinal lubrication.

5.5 Conclusions

The experimental results demonstrated that both mucus and PBS contributed to reduced friction coefficients compared to low hydration conditions. However, no statistically significant differences were observed between the mucin-containing samples at varying concentrations and pH levels and the PBS control. This indicates that under the current test setup, the lubricating performance of PBS and mucus solutions was comparable.

Based on the friction trends and the soft, hydrated contact environment mimicking the human intestine, it is hypothesized that hydration lubrication likely plays a dominant role, potentially supplemented by boundary and fluid-film effects. However, this interpretation should be approached with caution due to the absence of strong statistical support.

The study also highlights several limitations, particularly the challenge of accurately replicating the full complexity of intestinal juice, including factors such as enzyme content, microbiota, and dynamic flow secretion. Future research should incorporate a broader range of biological fluids and rheological properties to better differentiate the contributions of specific mucus components.
Despite the absence of statistically significant differences, the methodology proved robust and sensitive enough to capture friction results across conditions. These findings support its continued application in subsequent evaluations of capsule design and tissue interaction under variable test environments.

Chapter 6

Friction tests: Capsule properties

6.1 Introduction

Figure 1.1 highlights the key factors influencing the tribological behaviour of a capsule robot moving through the small intestine. Key determinants include the size, shape, and surface texture of the capsule, as these impact the contact area and pressure distribution against the intestinal walls. The velocity of the capsule and the normal load applied to the intestine during movement also play a significant role, as these can affect tissue deformation and the resulting frictional forces. The properties of the intestinal tissue, such as elasticity, viscosity, and surface morphology, further contribute to the interaction dynamics. The secretion of non-Newtonian mucus by the intestinal lining forms a lubricating layer, which can either enhance or diminish friction depending on the capsule's speed and orientation. Understanding these factors is essential for optimizing capsule robot design and ensuring safe, efficient navigation through the intestinal tract. The effects of mucus, tissue mechanical properties, and morphology have been studied previously (chapter 3 and 5), and this chapter will focus on the effects of capsule robot properties.

The frictional properties are characterized at the simulated endoscope-intestine interface under varying capsule lengths, diameters, normal loads, sliding speeds, and orientations during operation. Using the methodology outlined previously, the results are analysed and discussed providing a general understanding of the friction behaviour of capsule robots under these conditions and the findings were aimed to reduce the likelihood of capsule retention issues. Furthermore, based on these results, ridge designs of the capsule shell along with surface roughness were developed and assessed to address slippage problems in some active capsule robots and to mitigate the issue of capsules moving too quickly to completely image the entire small intestine. As a

result, the optimal ridge design was identified, providing valuable recommendations for the future development of capsule robots.

6.2 General friction results between the small intestinal tissue and capsule endoscopy

6.2.1 Introduction and Method

In experiments examining the friction performance between various capsule properties and the small intestine, a benchmark group was typically used with the capsule measuring 28 mm in length and 12 mm in diameter. The experimental conditions were standardized, with speed and normal load set at 5 mm/s and 0.5 N, respectively, without targeting variables such as load and speed, as explained in the previous study (section 4.4). Additionally, the mucus preparation used a mucin concentration of 5 mg/ml, adjusted to a pH of 7.5, ensuring complete dissolution of the mucin powder and preventing any impact on the experimental results. This approach allows for the collection of substantial data under consistent conditions, with tissue diversity as the only variable. The tissue used was subject to the same preparation and thawing process as described earlier (section 5.2.1). A total of 6 porcine small intestines were used. From each intestine, two adjacent segments were extracted from the middle region, resulting in 12 tissue samples. Each sample was then tested at three distinct locations, left, middle, and right as shown in Figure 4.13, along the tissue surface, yielding three independent measurements per sample. Overall, 36 tests were conducted, and the resulting data serves to analyse the basic friction behaviour of the capsule as it moves through different tissues, providing foundational friction data for medical operations during CE surgery.

6.2.2 Results

Figures 6.1 and 6.2 present the static and kinetic COF results obtained from all 36 tissue samples, along with the individual COF values recorded for each sample and each location, respectively. Both static and kinetic COF datasets followed a normal distribution. The statistics tables for the results were provided in Appendix G.

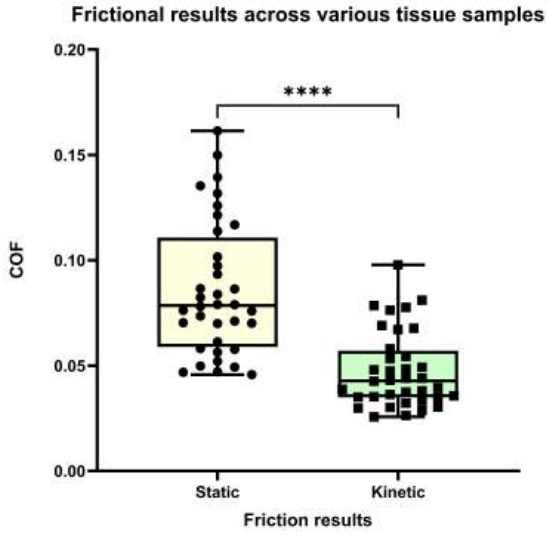

Figure 6.1: The static and kinetic COF results from 36 friction tests conducted using an identical experimental protocol.

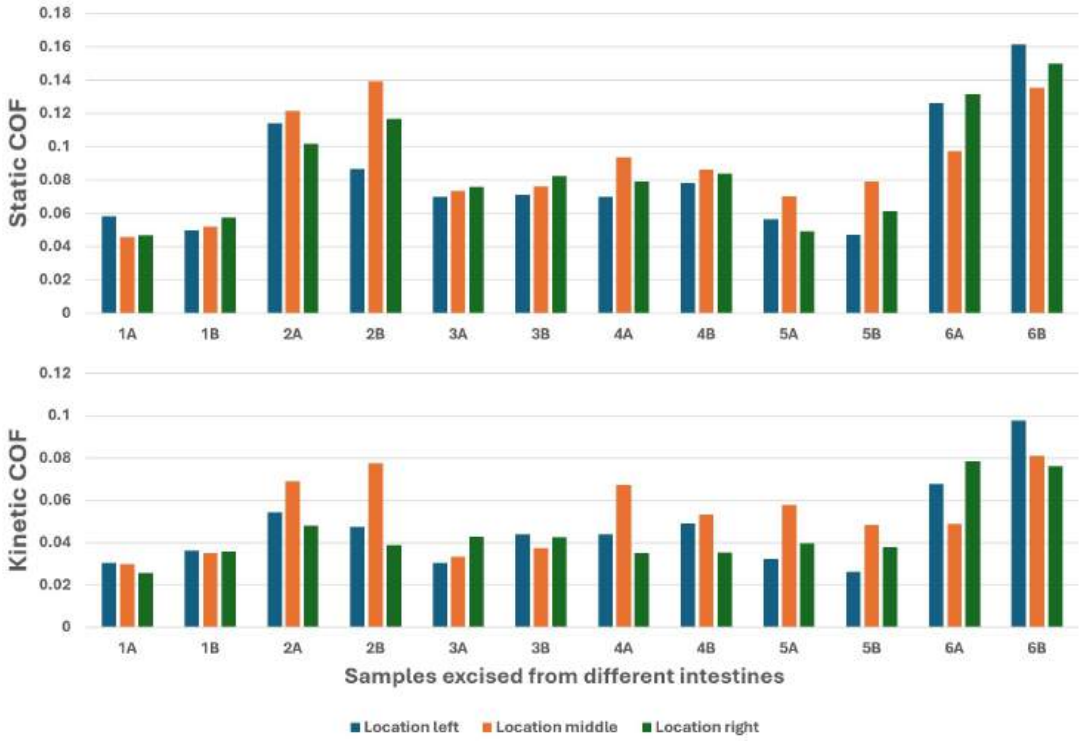

Figure 6.2: The static (top) and kinetic (bottom) COF results of each sample. The numbers represent different intestines, while the labels A and B denote two adjacent samples taken from the same intestine.

Statistical analysis of static and kinetic friction measurements revealed a significant difference between the two. Static COF values exhibited greater variability and higher average values compared to kinetic COF. Across the 36 tests, the static COF had a range of 0.1156, a standard deviation of 0.032, and a mean of 0.086. In contrast, the kinetic COF showed less variability, with a range of 0.07214, a standard deviation of 0.018, and a mean of 0.048. To identify which sample group pairs exhibited statistically significant differences, a post-hoc analysis was conducted using Tukey's multiple comparisons test. Among the 66 possible pairwise comparisons, 39 (approximately 40%) showed statistically significant differences in static COF, whereas only 9 comparisons (around 14%) were significant for kinetic COF, indicating a higher stability of kinetic measurements. Notably, no significant differences were observed between samples taken from adjacent regions of the same intestinal segment, whereas significant differences were found between samples from different segments (e.g., 1A vs. 5A), highlighting the regional variability of different intestines.

The variation trends between friction force and COF showed a high degree of consistency (Figure 6.3). The observed oscillations in the curves may be attributed to stick-slip movement, as they exhibit a pattern similar to stick-slip behaviour. Unlike smoother and thicker tissues such as human forearm skin, human finger, or porcine esophagus, the small intestine exhibited a distinct stick-slip behaviour. This difference was attributed to the unique biomechanical and structural properties of the small intestine, including its soft, viscoelastic tissue, thin walls, and unique biological structures such as circular folds, which dynamically interacted with the capsule during sliding [49, 135, 136]. However, other potential reasons could also explain these oscillations, suggesting that the probe was continuously slipping rather than exhibiting stick-slip behaviour. A detailed analysis of this friction behaviour is provided in the discussion.

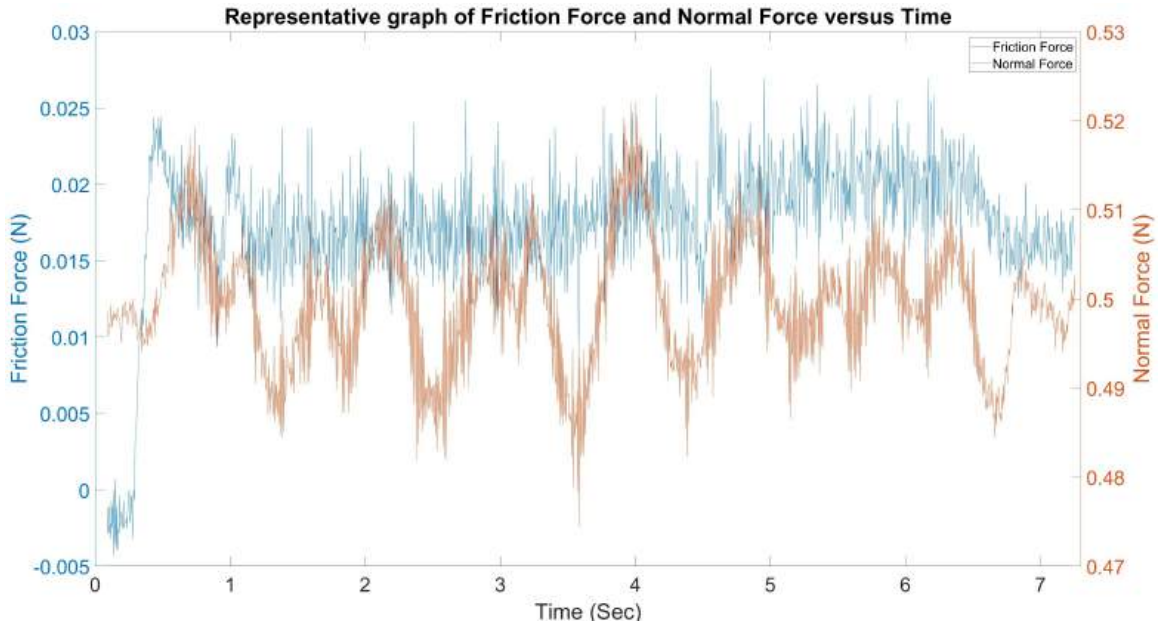

(a)

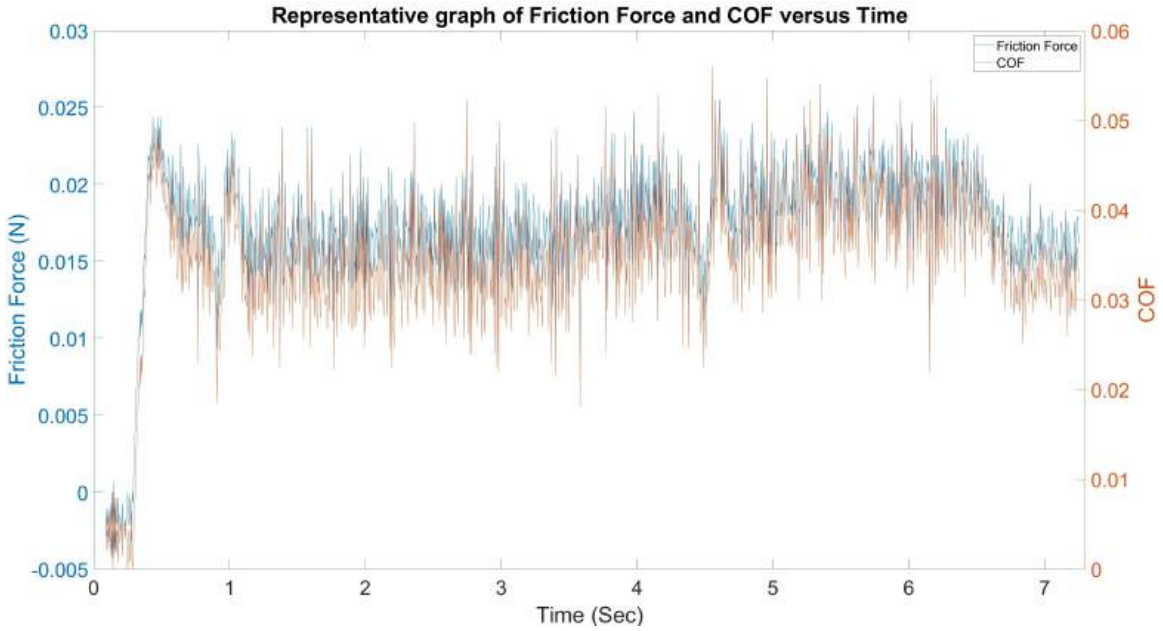

(b)

Figure 6.3: (a) Typical variation of friction force and normal force versus time of one unidirectional sliding cycle. (b) Typical variation of friction force and COF versus time of one unidirectional sliding cycle. One example out of 36 tests which was chosen to be the typical representation of the results.

6.2.3 Discussion

This study presents the general COF data for both static and kinetic friction conditions across various samples by using an identical test protocol. The distribution of the data points highlighted the biological variability of the porcine small intestinal tissues, which correlates with the surface texture and roughness measurements presented in section 3.4. Variations were observed both between different intestines and across different locations within a single sample. Based on the analysis of 36 friction tests, the statistical results revealed that adjacent regions from the same intestinal segment exhibited a certain degree of consistency in frictional properties, whereas samples from different intestines might show substantial variability. It should be noted, however, that this conclusion may not be definitive, as the sample size might be insufficient to draw statistically robust conclusions. A larger dataset would be necessary to validate the observed trends and further minimize the influence of biological variability. In later different friction scenarios tests, to minimize the effects of tissue variation, the samples used in the experiments were excised from adjacent parts of the intestines.

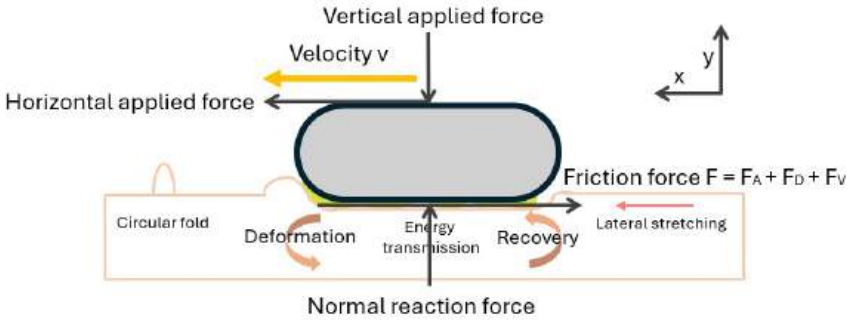

Figure 6.4: A simplified force analysis diagram of analysing the friction force of a capsule robot sliding on the small intestinal tissue.

To facilitate a clearer analysis of the frictional forces acting on the capsule, a simplified force diagram was created, as shown in Figure 6.4. The combination of forces as shown, will produce a moment on the capsule which will be resisted by the system holding the capsule in place. In this model, the direction of the friction force is assumed to be parallel and opposite to the capsule's motion. While this assumption simplifies the analysis, it is important to note that actual conditions are more complex, tissue deformation introduces resistance along the conformed intestinal

counter-face, which cannot be fully captured in a two-dimensional diagram. Based on previous research characterizing frictional resistance between an object and soft tissue, the total friction force (F) acting on a capsule can be expressed as the sum of interfacial adhesion resistance (F_{A}), tissue deformation resistance (F_{D}), and viscous resistance (F_{V}) [43, 49, 137].

$$F = F_{\mathrm{A}} + F_{\mathrm{D}} + F_{\mathrm{V}} \tag{6.1}$$

The adhesion resistance F_{A} involves the energy dissipated when intermittent junctions, formed between the sliding surfaces, break due to short-range molecular forces such as Van Der Waals interactions. This process underpins the adhesion-based friction model. In this model, the interfacial frictional force is calculated as the product of the interfacial shear strength τ and the real contact area A:

$$F_{\mathrm{a}} = \tau \cdot A \tag{6.2}$$

The parameter A represents the real contact area over which short-range attractive and repulsive forces act. For two topographically rough surfaces, this area may be considerably smaller than the apparent contact area.

The deformation resistance F_{D} generally arises from the partial recovery of energy dissipated due to subsurface viscoelastic deformation beneath the leading edge of the capsule robot (including compression and the build-up pile of tissue), in-plane contribution due to viscoelastic stretching in the lateral direction and the obstacle resistance caused by the circular folds.

Viscous friction during sliding F_{V}, also known as fluid drag, represents the resistance of the mucus during shear (not the static resistance, which arises from adhesive bonds), is influenced by the rheological properties of the mucus within the contact area and can be described by the following expression:

$$F_v = \delta \cdot v \tag{6.3}$$

where δ represents the apparent viscosity coefficient and v is the relative velocity. From the results of previous mucus chapter, the viscosity of mucus used in this study was relative small, so this part of resistance would be ignored.

According to the friction graph and curves, static friction resistance was generally greater than kinetic friction resistance for small intestinal tissues. Several mechanisms account for this difference based on above analysis on friction:

- Microscopic interlocking. In the stationary state, microscopic asperities on both the tissue surface (e.g., villi and microvilli) and the capsule robot mesh together, become interlocked. Overcoming these interlocks demands a higher initiation force. Once relative sliding begins, these interlocks break and reform less strongly and completely due to reduced time for engagement, thereby lowering resistance.

- Adhesion forces. Intermolecular attractions such as Van der Waals interactions and hydrogen bonding, are more pronounced during static contact because the interface has time to consolidate. During motion, the shorter contact duration diminishes these adhesive contributions. Moreover, localized viscoelastic deformation of the intestinal wall enlarges the real contact area while stationary, thereby further heightening static friction.

- Tissue deformation. At the onset of motion, the capsule initially moves together with the intestinal tissue in a stick phase, during which lateral stretching of the tissue occurs. This stretching generates a resistive force, contributing to increase static friction. Once sliding begins, the deformed tissue relaxes and tends to return to its original shape, leading to a reduction in contact area and deformation. As a result, kinetic friction decreases accordingly.

- Lubrication by mucus. Mucus present at the interface is less effective when the surfaces are static. Sliding action promotes the influx of lubricant into the interface, promoting hydration lubrication and other lubrication regimes as introduced in Chapter 5 and further lowering kinetic friction.

Collectively, the greater initial interlocking and adhesion force, deformation, viscoelastic relaxation dynamics, and motion-enhanced lubrication explain why static friction consistently surpasses kinetic friction for small intestinal tissue.

This relationship between static and kinetic friction revealed the compound characteristics of friction behaviours. Experimental videos and vertical displacement data of the probe were reviewed, but challenges remain in determining whether the motion was stick-slip or another type of movement (since it might just be continuous sliding

rather stick-slip). Therefore, instead of firmly stating that the stick-slip phenomenon is causing the fluctuations in the normal load and friction curves, it would be more appropriate to analyse the various possibilities that could explain the observed results. Possible factors contributing to these observations include the varying properties of the tissue, such as stiffness and thickness, with normal force fluctuations potentially resulting from traversing a bumpy surface with tissue folds that influence friction outcomes. Additionally, the noise-like pattern could be attributed to potential machine measurement errors (e.g., data measurement accuracy caused noise) or adjustments made by the machine load control function, to maintain a constant load force of 0.5 N, leading to slight automatic modifications of parameters.

It is also possible that the friction results suggest stick-slip behaviour, given the consistently higher static than kinetic coefficients of friction. Under the stick-slip hypothesis, two distinct types of stick-slip behaviour are considered possible.The first type of stick-slip arises from the interaction between the circular folds (villi and microvilli) and irregularities of the intestinal inner surface with the texture of the capsule shell. This interaction causes a micro-interlocking effect, where the capsule temporarily sticks to the surface due to local frictional forces. When the horizontal force exceeds the resistance from these interlocking forces, the capsule briefly detaches and slides forward, initiating a cycle of sticking and slipping. These localized, cyclic stick-slip interactions result in continuous minor fluctuations on the friction force curve.

In contrast, the second type of stick-slip behaviour is characterized by tissue deformation during sliding. When the capsule makes initial contact with the intestinal wall, it causes localized tissue indentation due to the applied pressure. As the capsule advances, it pushes and deforms the viscoelastic intestinal tissue, leading to a gradual build-up of tissue in front of the capsule. This deformation increases the resistance force until a critical threshold is reached. At that point, the deformed tissue detaches from the capsule, allowing it to move forward. The extent of sticking is influenced by the tissue's ability to deform and accumulate in response to the advancing capsule. This process is further affected by variations in tissue thickness and the presence of resistance structures, such as intestinal folds. This type of stick-slip contributes to the up-and-down pattern observed in the normal load curves, although the relatively minor magnitude of these variations (approximately 0.02 N) means they do not pro-

duce distinct features on the friction force curve.

Overall, these two types of stick-slip may collectively contribute to the observed force fluctuations. This could be due to a complex interplay between the capsule's surface characteristics, intestinal microstructures, and the viscoelastic properties of the tissue. The first type of stick-slip appears to be driven by surface-level interactions involving fine anatomical structures and local frictional forces, whereas the second type may involve larger-scale tissue deformation and resistance accumulation. Although the overall COF between the capsule and the intestinal tissue is low, the dynamic interaction between frictional forces, normal forces, and tissue mechanics is likely to play a role in generating the oscillatory patterns. High friction spikes during a potential stick phase could lead to temporary stalling of the capsule, which might result in irregular motion and incomplete coverage during diagnostics. Conversely, sudden slips may cause jerky movements that have the potential to compromise capsule stability and degrade imaging clarity. Fluctuations in the normal force, possibly resulting from the soft and dynamically changing intestinal environment, may further influence the threshold for static friction, thereby contributing to the variability in motion. While further investigation is needed to fully confirm these mechanisms, identifying and mitigating such behaviours could be important for improving capsule endoscopy performance. Future capsule designs may benefit from features that reduce stick-slip effects, such as low-friction surface coatings or active propulsion systems to regulate motion, potentially ensuring smoother transit and enhancing diagnostic accuracy.

6.3 Effect of capsule size on friction

6.3.1 Introduction and Method

The relationship between capsule size and friction was analysed to examine how variations in diameter and length affect tribological behaviour. Larger capsules may have a larger contact area with lower compression pressure, and these two factors have opposing effects on friction. The overall frictional effect will be evaluated through test results, offering insights for optimizing capsule shell design.

The capsule prototype was manufactured according to the dimensions listed in the table based on the commercial CE products (Table 2.1) and shown in Figure

6.5. As with previous tests, the same protocol was followed, with speed, normal load, and sliding distance set at 5 mm/s, 0.5 N, and 30 mm, respectively. The mucus was prepared at a concentration of 5 mg/mL, with the pH adjusted to 7.5, and 10 mL was used for each test. For each capsule prototype, a minimum of 3 samples, at least 9 tests were tested. The results were analysed using the same statistical methods outlined in Section 5.2.4.

Diameter D (mm)	Total length L (mm)
10	28
11	28
12	28
13	28
12	26
12	28
12	30
12	32

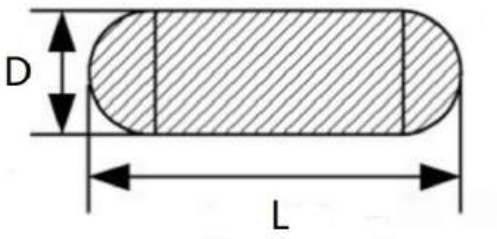

(a)

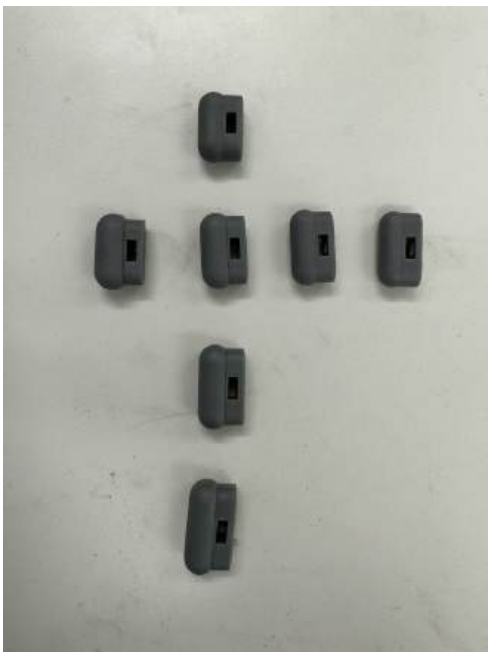

(b)

Figure 6.5: (a) The diagram and table show the dimensions of capsules. (b) Manufactured 3D-printed capsule prototypes with different dimensions.

6.3.2 Results

Figure 6.6 presents the COF results for capsules with the same diameter but varying lengths, as well as for capsules with the same length but varying diameters sliding against the intestinal tissues. The test results indicated no significant differences in COF values by changing the capsule diameters or the lengths, indicating that the capsule size change may have a minimal effect on friction behaviour when sliding on tissue samples. While no clear pattern emerged across the different test groups based on capsule length, a noticeable trend was observed that capsules with larger diameters tended to have lower COF values, might be particularly relevant due to

better load distribution across the contact area.

The power analysis table provides key statistical insights into the effects of capsule diameter and length on both static and kinetic friction coefficients that power of tests were low to verify the true difference between groups and more test sets were needed. For capsule diameter, the power for static friction is 0.38, whereas the power for kinetic friction is slightly lower at 0.28. To achieve a statistical power of 0.8, the total sample sizes required are 92 for static friction and 124 for kinetic friction. For a higher power level of 0.95, the sample sizes increase to 140 and 188, respectively. In the case of capsule total length, the power for static friction is 0.27, which is very similar to the results for capsule diameter. To reach a power of 0.8, a sample size of 124 is needed, while a power of 0.95 requires 192 samples. For kinetic friction, however, the power is significantly higher at 0.55, indicating a better ability to detect significant differences with the current data. The sample size required for a power of 0.8 is reduced to 60, and for a power of 0.95, it increases slightly to 92.

Power Analysis	Capsule Diameter D (mm)		Capsule Total length L (mm)	
	Static	Kinetic	Static	Kinetic
Power	0.38	0.28	0.27	0.55
Total sample size for power 0.8	92	124	124	60
Total sample size for power 0.95	140	188	192	92

Table 6.1: Power analysis results of capsule size tests.

6.3.3 Discussion

Generally previous studies showed that friction resistance increased with capsule diameter and length [36–38, 40], and one study reported similar results where capsule size had no significant effect on friction force [45]. In contrast, the results shown in figures reveals no statistically significant difference when varying these parameters. Due to the limitations of the current experimental setup and available techniques, measuring the contact area and its changes was not possible. Therefore, the following analysis explores the potential reasons for this phenomenon. Two important points should be noted in comparison with previous studies. First, those studies did not include statistical analysis to confirm whether the observed differences between groups were significant. Second, their test setups lacked mucus coverage during testing, which could have influenced the results. According to the previous section of friction force analysis, applying the same loading force to a larger surface area may result in a

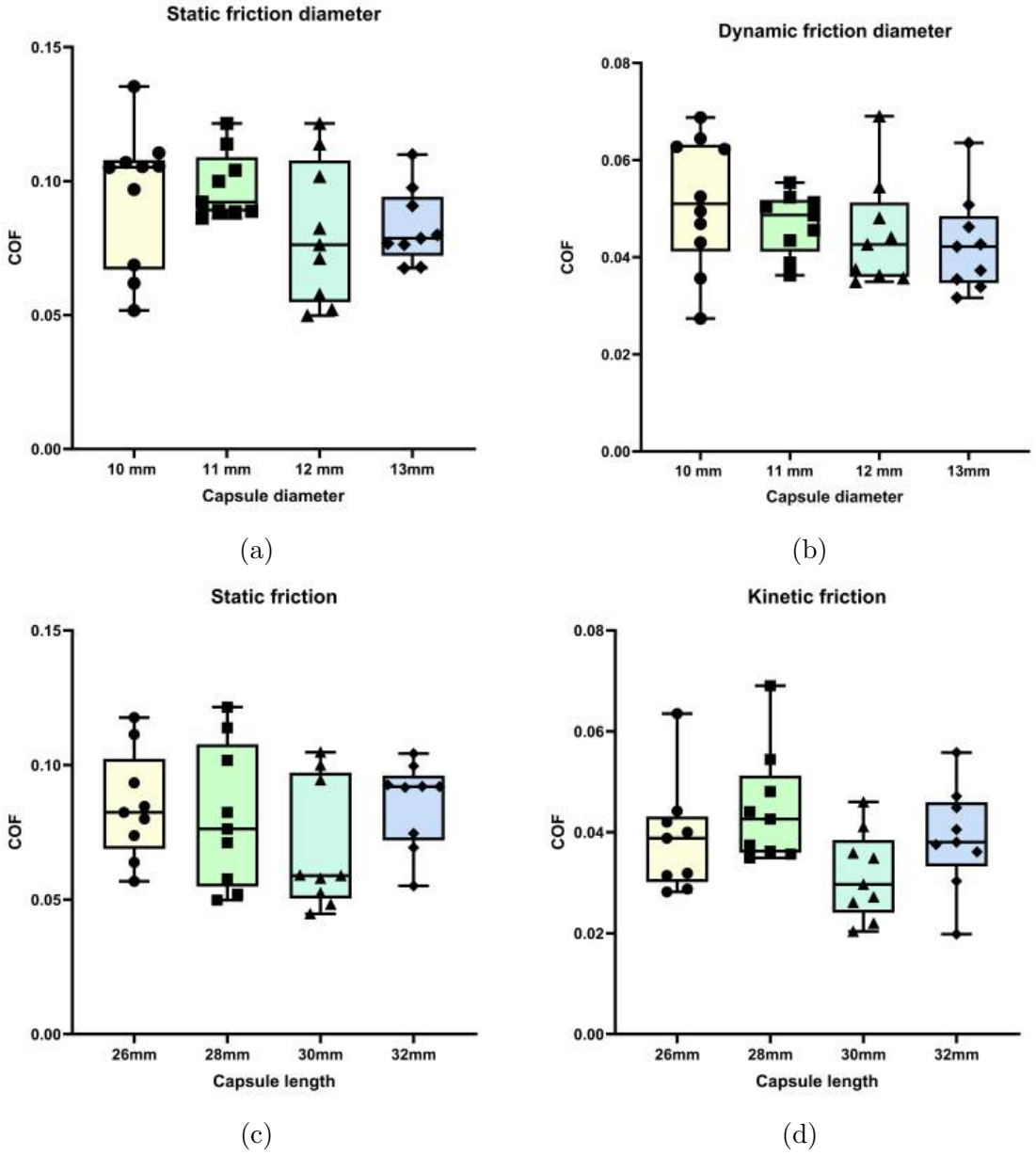

Figure 6.6: Friction results: Static and kinetic COF for different capsule diameters (a),(b) and different total lengths (c),(d).

larger contact area with lower contact pressure, leading to smaller tissue deformation. Since adhesion force is proportional to the contact area, a larger contact area would result in more molecular bonds forming and rupturing, increasing resistance. On the other hand, smaller deformation with small pressure may indicate lower resistance when the tissue folds up in front of the capsule robot. In this conjecture, these two effects counterbalances each other, and since their magnitudes are similar, changing the capsule size does not lead to a significant difference in friction. It is also possible

that the real contact area remains relatively unchanged across the different sizes, resulting in no clear difference in the friction results. Furthermore, the range of capsule sizes chosen may have been too limited for a distinct difference to occur. Overall, the results from the power analysis highlight the challenges in achieving adequate statistical power for detecting significant differences for changing both capsule diameter and capsule length. The low power values suggest that the current sample sizes are insufficient to confidently identify trends or relationships. This is further supported by the relatively large sample sizes needed to achieve a higher power shown in Table 6.1, particularly for static friction.

The practical significance of analysing the effect of capsule size on the COF lies in its potential to provide guidance on size limits of the future shell design, allowing for greater internal volume in the capsule robot. This would accommodate more functional modules, enabling the performance of a broader range of medical tasks. If the current conclusion is accurate, this suggests that slight increases in the size of the capsule robot, potentially required for embedding additional systems, should be acceptable and have no influence on increasing the retention risks.

6.4 Effect of capsule orientation on friction

6.4.1 Introduction and Method

The aim of studying the effect of different capsule orientations is to simulate scenarios where the capsule is rotated in various orientations (not aligned with the horizontal axis of the small intestine) or encounters bends within the intestine while moving. Changes in the capsule's alignment would alter the contact area and pressure distribution, such as tilting when interacting with circular folds, which in turn may affect the COF. However, this research topic has received limited attention in previous studies. Therefore, tests were conducted using the same experimental protocol, with the capsule orientation changed to 0°, 30°, 60°, and 90° to the direction of motion of the UMT probe to examine the differences in detail (Figure 6.7).

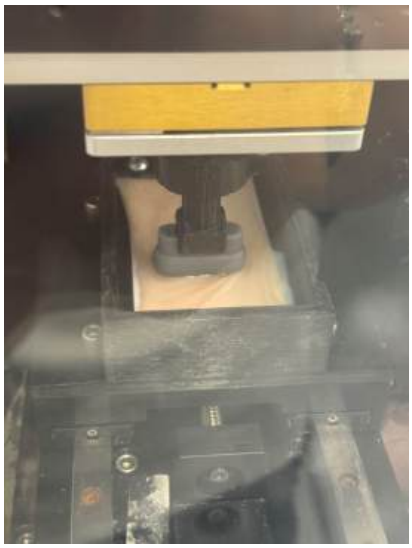

Figure 6.7: Capsule sliding in a 90° orientation to direction of motion.

6.4.2 Results

The orientation of the capsule relative to the horizontal axis of intestinal tissue surface significantly influenced the COF during movement, as shown in Figure 6.8. For static friction (Figure 6.8a), the COF increased with the travel orientation angle. At 0° (aligned orientation), the COF was lowest, with a median value of approximately 0.06. As the orientation angle increased to 30° and 60°, the COF gradually rose, showing noticeable variability. At 90° (perpendicular orientation), the COF reached its highest values, with a median of around 0.091, representing a 52% increase. Significant differences were observed between 0° and 60° ($p < 0.01$) and between 0° and 90° ($p < 0.001$). For kinetic friction (Figure 6.8b), a similar increasing trend was observed. The COF at 0° was the lowest, with a median of around 0.04. As the angle increased to 30°, 60°, and 90°, the COF rose significantly, with the highest value at 90° (median of around 0.073), representing a 82.5% increase. Statistical analysis revealed significant differences between 0° and 30°, 30° and 90° ($p < 0.01$), and between 0° and 90° ($p < 0.0001$). Overall, these results indicate that both static and kinetic friction coefficients increase with the travel orientation angle of the capsule.

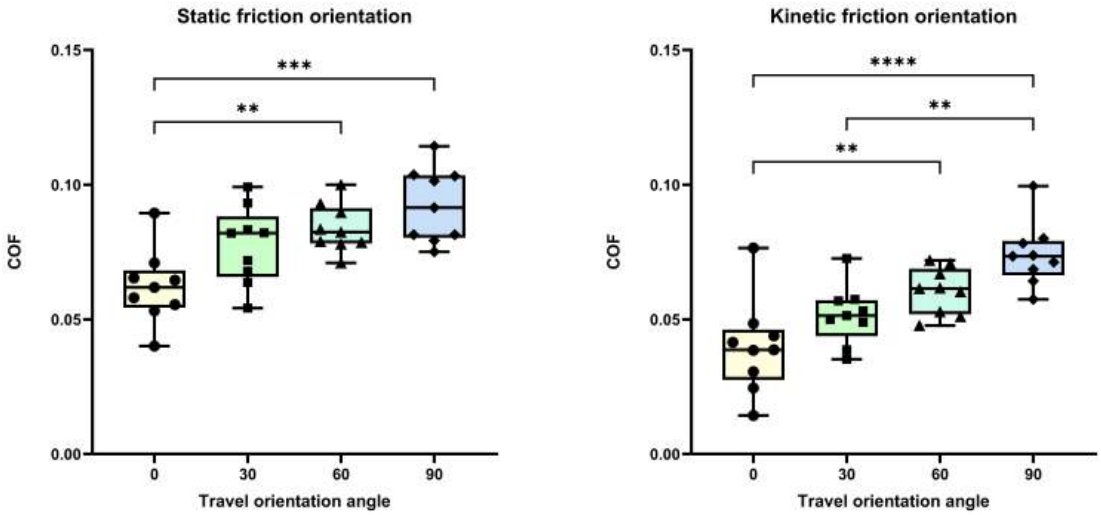

(a) (b)

Figure 6.8: (a) Test results of static COF versus capsule orientation. (b) Test results of kinetic COF versus capsule orientation.

6.4.3 Discussion

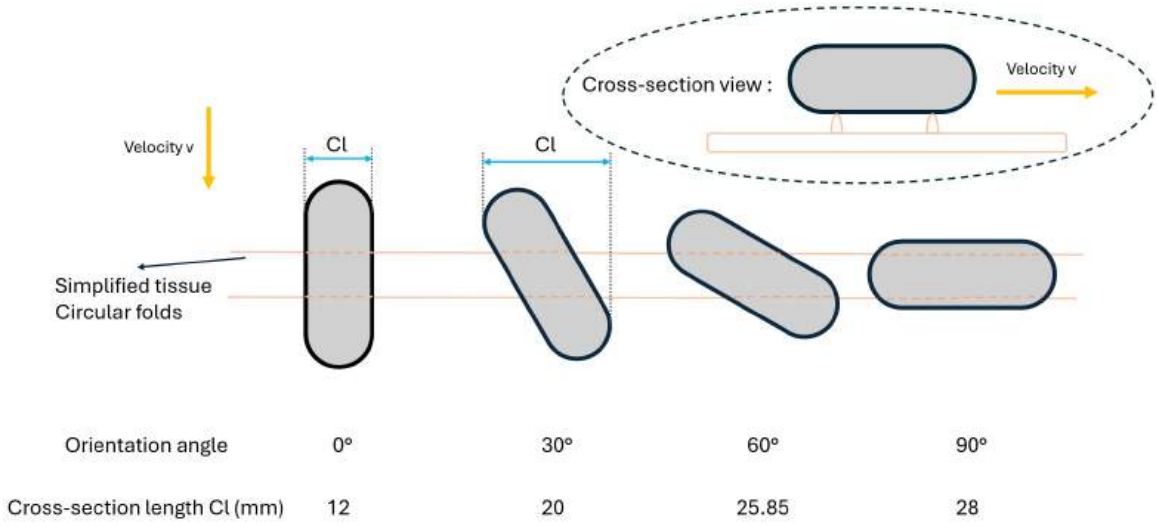

Figure 6.9: Schematic diagram of the capsule sliding between circular folds.

The observed increase in COF with larger capsule orientation angles can be explained by changes in adhesion friction and deformation friction. When the capsule orientation deviates from 0° (aligned with the horizontal axis), its contact mechanics with the soft tissue are altered, leading to increased frictional forces.

Figure 6.9 presents a simplified scenario in which the capsule is shown "bridging" two circular folds for illustrative purposes. In reality, the anatomical condition is likely to be more complex with additional folds and structural surface variations; however, the basic mechanical interpretation may still apply. At 0°, the capsule appears to maintain better alignment with the soft tissue. As the orientation angle increases to 30°, 60°, and 90°, the cross-sectional length (Cl) across the folds becomes larger, as indicated by the extended dashed lines. In this simplified model, the overall real contact area may remain relatively constant with changes in orientation; however, the degree of deformation is likely influenced by these angular changes.

Deformation-related friction is possibly associated with the viscoelastic response of the soft tissue under compressive and shear loading during capsule motion. At higher orientation angles, the measured Cl values increased, suggesting that the capsule may have engaged with a greater number of circular folds, encountered more pronounced surface irregularities and also was causing more tissue accumulation against the moving direction. The viscoelastic properties of the tissue could have contributed to increased resistance in these cases. When a larger portion of the capsule interacts with the folds, more substantial tissue deformation may occur in the direction of movement. This process, involving local compression and displacement of tissue structures, could potentially lead to higher frictional resistance as the capsule advances.

In addition, the circular folds in the small intestine are generally oriented parallel to the longitudinal axis of motion, as depicted in Figure 3.17. At 0°, the capsule is likely to glide more smoothly along the folds with minimal mechanical interference. As the orientation angle increases, the capsule appears to encounter these folds at a more oblique or perpendicular angle, which may result in increased resistance and localized mechanical stresses. At 90°, the capsule's trajectory is nearly orthogonal to the fold direction, a condition that could promote both greater adhesion friction (due to enhanced contact area) and deformation friction (due to greater tissue displacement). This may help explain the higher coefficients of friction observed at this angle.

These observations suggest the possibility that greater capsule orientation angles may increase the likelihood of the capsule becoming temporarily stuck or slowed within the intestinal lumen due to elevated frictional forces. This highlights the potential importance of maintaining near-optimal orientation during capsule endoscopy

to promote smooth movement and reduce resistance. This phenomenon should be taken into consideration during device development, as implementing corresponding design or control measures may help mitigate the risk of capsule retention. Furthermore, the findings in this section raise the possibility that using a capsule with a larger diameter—such as those used in studies on size effects—might produce more pronounced differences in friction and tissue interaction.

6.5 Effect of capsule sliding speed and load force on friction

6.5.1 Introduction and Method

The effect of varying load and sliding speed on frictional behaviour was evaluated to simulate the diverse real-world conditions of capsule movement. Considering the different movements of intestinal peristalsis and peristaltic rush, could cover range from 1-2 cm/min to 2.4 cm/s [125]. Based on the load ranges observed in various commercial products and other CE prototypes in the literature, a load range of 0.1 to 1.5 N was chosen [36, 41, 42, 45, 101, 138]. Thus, the same experimental protocol as before was used, with sliding speeds of 1, 5, 10, and 15 mm/s tested at a normal load of 0.5 N for testing the sliding velocity effect on friction. Additionally, normal loads of 0.1, 0.5, 1, and 1.5 N were tested at a sliding speed of 5 mm/s for testing the normal force effect on friction.

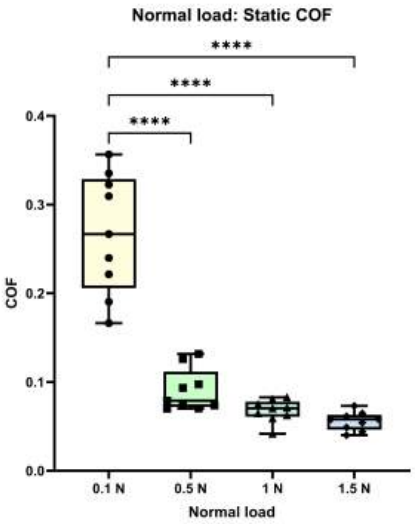

(a)

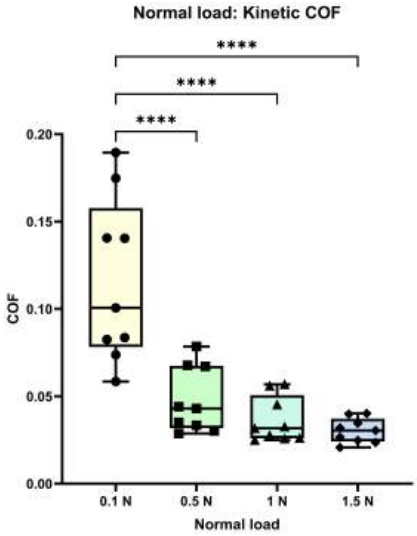

(b)

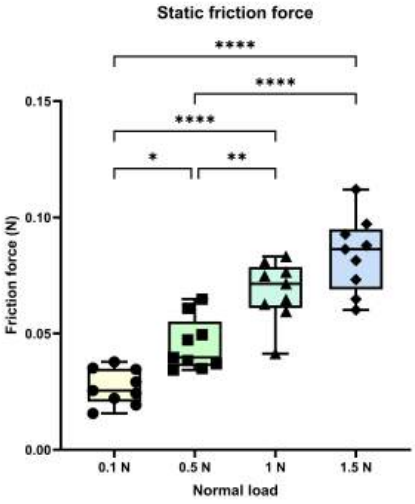

(c)

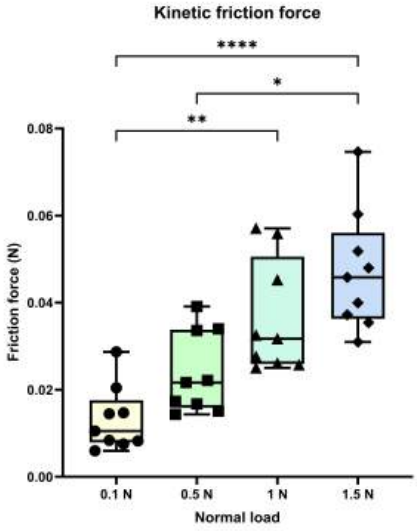

(d)

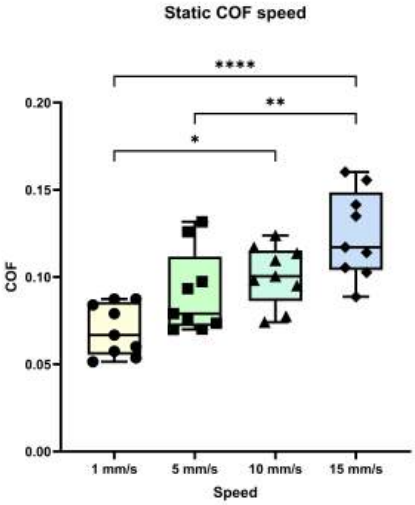

(e)

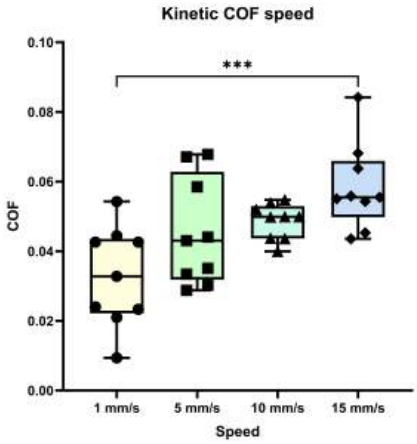

(f)

Figure 6.10: The static and kinetic COF results for varying capsule velocities and normal loads are shown in graphs (a), (b), (e), and (f). The static and kinetic friction force results are illustrated in graphs (c) and (d).

6.5.2 Results

Figure 6.10 presented COF and friction force results of varying normal load and sliding speed on the frictional behaviour of the capsule. For the effect of normal load on frictional behaviour, the results showed a clear trend (like an exponential decay) that kinetic COF decreased significantly as the load increased. At a load of 0.1 N, the static COF was the highest, with a median value reaching approximately 0.27. However, as the load increased to 0.5 N, 1 N, and 1.5 N, the static COF decreased sharply and stabilizes at values close to around 0.6. Statistical analysis revealed highly significant differences ($p < 0.0001$) between the COF at 0.1 N and all higher loads. A similar trend was observed for the kinetic COF, which decreased from 0.1 at 0.1 N to approximately 0.03 at higher loads. This consistent decrease suggests that increasing the normal load reduces both static and kinetic COF.

While the COF decreased, the friction force increased proportionally with the normal load. For static friction forces, the values increased from approximately 0.026 N at 0.1 N load to 0.095 N at 1.5 N load, representing a 265% increase. A similar proportional increase was observed in kinetic friction forces, where the force rose from around 0.011 N at 0.1 N load to 0.046 N at 1.5 N load, representing a 318% increase. This indicates that although the COF reduced, the total friction force still increased almost linearly with the applied load. Significant differences of friction forces generally were observed between the high normal loads and the low normal loads.

For the effect of sliding speed, the results showed that the COF increased with increasing speed. The static COF exhibited a significant rise from approximately 0.067 at 1 mm/s to values close to 0.12 at 15 mm/s, representing a 79% increase. Statistical analysis revealed significant differences ($p < 0.05$) between the speeds, particularly between 1 mm/s and the higher speeds of 10 mm/s and 15 mm/s. Similarly, the kinetic COF also increased with speed, although the trend was less pronounced. At 1 mm/s, the kinetic COF was approximately 0.033, while at 15 mm/s, it reached values around 0.055, representing a 67% increase. Statistical analysis confirmed significant differences ($p < 0.001$) between 1 mm/s and 15 mm/s.

6.5.3 Discussion

The results demonstrate that both normal load and sliding speed significantly influence the frictional behaviour of the capsule, which can be explained by considering the roles of adhesion friction and deformation friction.

Regarding the effect of load, the observed decrease in the COF with increasing load follows a trend similar to that seen in previous studies [36, 37, 49]. Typically, soft tissues, being deformable, would experience an increase in real contact area under higher loads. However, in this case, the real contact area might actually be decreased. A key explanation for this behaviour lies in the microstructural features of the tissue surface. The intestinal tissue surface is covered with numerous villi and microvilli, which are capable of retaining water, mucus, and other liquids, thereby maintaining a lubricated and hydrophilic surface. When a higher normal load was applied, more mucus or water was squeezed out from these structures, leading to the formation of a stronger fluid film and creating a localized hydrodynamic lift. This fluid layer effectively separated the capsule robot from the tissue, resulting in a smaller real contact area and also the shear resistance (as the uneven tissue surface was over compressed and became smoother), reduced adhesion friction, and better lubrication of the interface. Moreover, the friction inside living intestines, may be even lower than experimental results, as the secretory fluids in living tissue are more abundant, further enhancing the lubrication effect. In terms of deformation friction, increasing the load caused greater viscoelastic deformation of the soft tissue. The soft tissue compressed more under higher normal loads, increasing the energy dissipated during deformation and the total friction force. However, the lubrication effect appeared to play a dominant role, ultimately contributing to a reduction in the overall COF.

For the effect of sliding speed, the COF increased with speed due to changes in both adhesion and deformation friction mechanisms. At higher speeds, the capsule interacted with the tissue surface for a shorter period, reducing the ability of molecular bonds to form and break. This was accompanied by a decrease in relaxation time and recovery, which ultimately resulted in higher shear resistance at the interface, increasing the COF.

A similar effect occurred in the tissue, amplifying the deformation friction. As discussed in the mechanical properties chapter (3.3.4), intestinal tissues exhibit time-dependent behaviour. A higher speed corresponds to a higher loading rate, meaning

the tissue responded more elastically, resulting in larger stress and a reduced ability to resist rapid deformation (larger build-up would occur in front of the capsule) which caused greater resistance. Additionally, the stress relaxation in the intestine was limited during the capsule's passage. The time for the tissue to recover its original shape or redistribute the stress was constrained, which further contributes to the increased frictional resistance.

The above findings can be summarized as when a capsule moves at a higher speed with a larger normal load, the resulting increase in frictional force could raise the risk of capsule retention problems. This is particularly relevant in clinical settings. For instance, in patients with suspected intestinal obstruction or stenosis, multiple factors must be considered when using capsule endoscopy. Even if the coefficient of friction decreases, higher friction resistance may still lead to greater pressure between the capsule and the intestinal wall, increasing the risk of damage to the small intestine. Although no specific scratches were observed during the experiment, such issues could manifest differently in diseased tissue areas. Excessively fast travelling speeds, whether actively or passively driven, may contribute to the same problem. It can be envisioned that when the peristalsis of small intestine moves rapidly, the capsule is propelled forward with a large initial velocity, and resulting in higher frictional resistance. This leads to a movement pattern where the capsule initially moves very quickly but decelerates sharply, akin to the sudden starting and braking of a vehicle motion. Furthermore, the camera's frame rate is limited of current commercial products, an excessively high travelling speed in this movement pattern may prevent the capsule from capturing enough clear images of all areas of the small intestine, potentially compromising the quality of the examination and the accuracy of the diagnosis.

6.6 Effect of ridge design and surface roughness of capsule shell

6.6.1 Introduction

Building on the previous discussion about the risks of excessive capsule speed, this study proposed modifications to the capsule shell design. These changes included the addition of ridge-like protrusions and alterations to the surface roughness, aimed at enabling the capsule to resist peristaltic waves that could propel it too quickly

	Capsule type							
Parameters	Original smooth type	Standard ridge	Ridge height 1	Ridge height 2	Ridge width 1	Ridge width 2	Surface roughness 1	Surface roughness 2
Capsule length (mm)	28	28	28	28	28	28	28	28
Capsule diamter (mm)	12	12	12	12	12	12	12	12
Ridge design height (mm)	None	0.5	0.75	1	0.5	0.5	0.5	0.5
Ridge design width (mm)	None	0.5	0.5	0.5	0.75	1	0.5	0.5
Average Surface roughness (μm)		8.5					12.6	14.42

Table 6.2: Capsule types used to compare various ridge designs and surface roughness designs

through certain sections of the small intestine. Additionally, prior research indicated that many active-type capsules struggled with inadequate speed control in the small intestine [59]. This issue arose from insufficient traction between the capsule's limbs and the smooth inner walls of the small intestine, leading to difficulties in movement. At this point, using the same methods from previous experiments, both types of novel capsules were tested to verify the impact of the two designs on friction through a comparison of the COF results.

6.6.2 Method

The idea of adding the ridge designs onto the capsule shell was inspired from the edge effect onto friction force of the capsule based on previous studies [45, 52]. It is found that a capsule with a less streamlined shape (such as a cylindrical form) encounters greater resistance during movement. To enhance this resistance, three ring-shaped, ridge-like protrusions were added to the capsule (dimension: diameter 12mm and length 28mm) (Figure 6.11, Table 6.2). The standard design features a semicircular shape with a radius of 0.5 mm. To investigate the effect of ridge height and width on friction and identify the optimal design, while keeping the other condition unchanged, modified designs with the ridge height and width changed to 0.75mm and 1mm, respectively, were also manufactured for experimental comparison. Notably, the fillet radius where the ridges meet the capsule surface was set to 0.25 mm, and the centreline positions of all three ridges across different designs were kept consistent to ensure experimental uniformity. Additionally, to explore the impact of surface roughness on friction, different roughness levels were achieved by adjusting the layer thickness of the 3D printing setting. Three standard capsules with average surface roughness values (not included the ridge, only the surface roughness of the main shell) of 8.5 µm, 12.6 µm, and 14.42 µm, as measured by Alicona scanning, were produced for comparison. The friction experiments followed the same protocol as previously, with a sliding speed of 5 mm/s and a normal load of 0.5 N and a visual inspection was conducted before and after the experiment to observe the tissue damage.

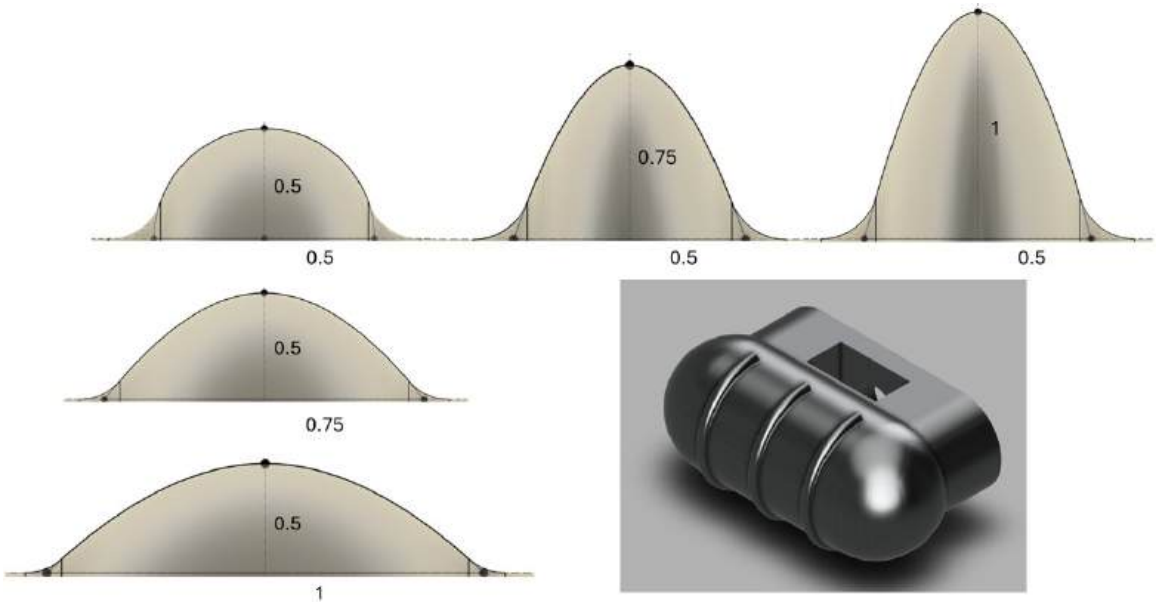

Figure 6.11: A schematic diagram presents the ridge designs, which vary in height and width.

6.6.3 Results

Figure 6.12 shows the typical friction curves for a sliding cycle of the capsule with the standard ridge design. It is evident that the capsule experienced significant stick-slip behaviour, as indicated by the larger fluctuations in both normal and friction forces compared to previous friction curves (Figure 4.12, 6.3) of smooth capsules. Additionally, the entire friction force curve displays a wave-like pattern of low-frequency stick-slip events, with some minor fluctuations, rather than a noise-like response. This might imply that deformation friction may dominate the overall frictional behaviour.

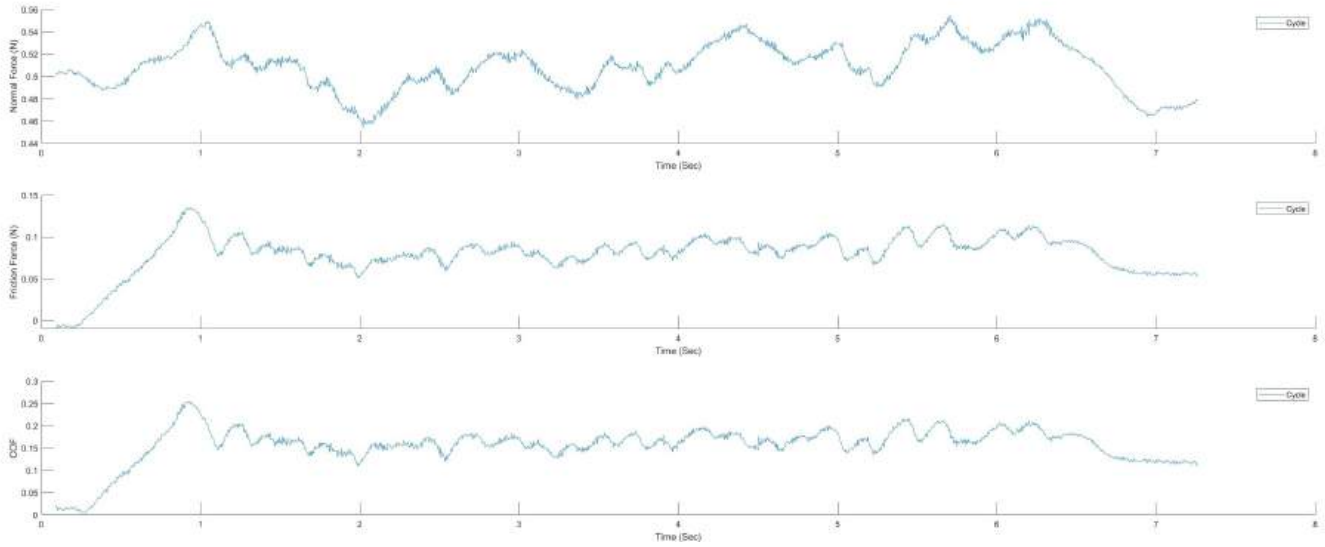

Figure 6.12: Typical friction force, normal force and COF curves of one sliding cycle of a capsule with the standard ridge design.

Figure 6.13 reveals the impact of ridge design and surface roughness on the COF for static and kinetic friction was evaluated. The results show clear differences depending on ridge height, ridge width, and surface roughness. The COF increased significantly as the ridge height increased for both static and kinetic friction. For static friction (Figure 6.13a), the COF for the original capsule design was approximately 0.084. When the ridge design height was increased to 0.5 mm, 0.75 mm, and 1 mm, the static COF progressively rose to approximately 0.25, 0.42, and 0.43, respectively. Statistical analysis showed highly significant differences ($p < 0.0001$) between the original smooth design and all ridge-modified capsules. For kinetic friction (Figure 6.13b), a similar trend was observed. The COF for the original smooth design remained low at around 0.04, while the COF increased to values of 0.15–0.31 as the ridge height increased. This indicates that larger ridge heights increased the resistance encountered during motion.

For the effect of ridge width on COF, it was distinct that the ridge designs exhibiting higher friction resistance as the COF for the ridge-modified designs was significantly larger, and statistical analysis revealed significant differences ($p < 0.0001$) between the smooth capsule and ridge-modified designs (Figure 6.13c). However, a trend was observed where increasing the ridge width led to a slight reduction in COF (0.25, 0.24, and 0.21), although this trend was not statistically significant. For kinetic friction (Figure 6.13d), a similar trend was observed. The capsule with the standard design showed the highest kinetic COF, while the wider ridge designs reduced the COF to approximately 0.14.

Results showed that various surface roughness had an unclear impact on both static and kinetic friction as no significant difference was observed. For static COF (Figure 6.13e), capsules with roughness levels of 8.5 µm, 12.6 µm, and 14.42 µm showed an increasing trend in COF. The static COF increased from approximately 0.25 at 8.5 µm to around 0.27-0.28 for higher roughness levels. For kinetic COF (Figure 6.13f), surface roughness also caused a slight increase from around 0.15 to 0.17.

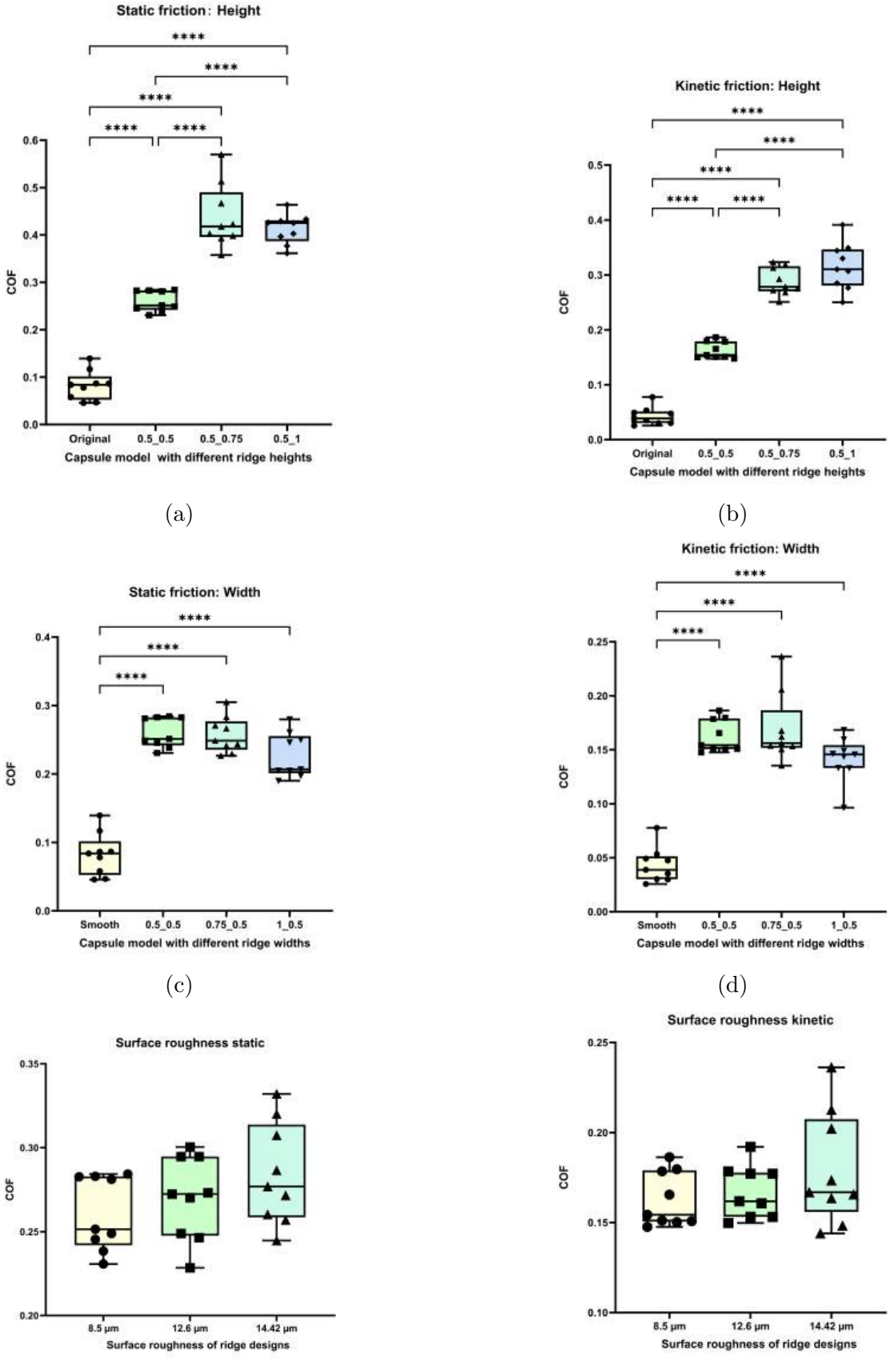

Figure 6.13: The static and kinetic COF results for varying capsule velocities and normal loads are shown in graphs (a), (b), (e), and (f). The static and kinetic friction force results are illustrated in graphs (c) and (d).

6.6.4 Discussion

The results demonstrate that both the ridge design (height and width) can significantly affect the frictional behaviour of the capsule. This can be explained through the mechanisms of the interaction between the capsule robot with ridges and intestinal tissue, as illustrated in Figure 6.14.

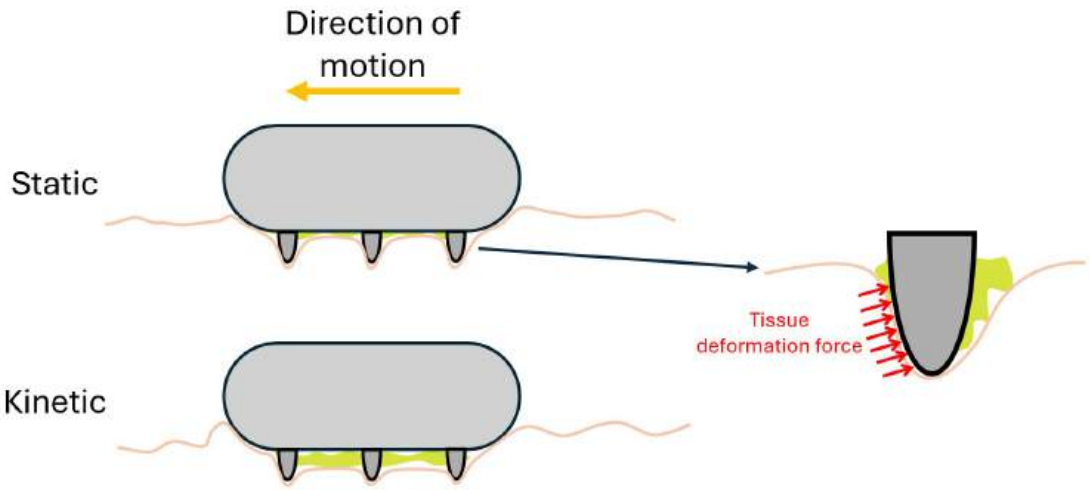

Figure 6.14: A schematic diagram illustrates the interaction between the capsule with ridges and the intestine.

The stick-slip phenomenon is essentially a cyclic transition process involving static and kinetic friction. Initially, the capsule applies a load onto the intestine, causing the capsule to press firmly against the tissue, resulting in significant deformation (deeper penetration) and high static resistance. When the horizontal applied force exceeds the tissue's tensile and shear strength, the capsule abruptly begins to slide, with the ridge penetration depth being smaller, leading to a drop in friction force. During the sliding phase, the tissue folds in front of the ridge, and its tension gradually increases. Once the accumulated tissue resistance exceeds the horizontal applied force, relative motion stops, and the system returns to the stick phase. This cycle repeats, producing the observed friction curves. Notably, the tissue buildup in front of each ridge is uneven. According to the direction of motion, it can be assumed that the ridge at the front experiences the most accumulation, followed by the middle ridge, and the rear ridge experiences the least. As a result, the relaxation and overcoming of each ridge's resistance do not occur simultaneously, leading to varying amplitudes. The deformation resistance in the ridge design is much higher than in the smooth capsule, causing an extended tissue accumulation response and more pronounced fluctuations.

This imbalance results in the wave-like pattern observed in the friction force curves.

The effect of changing the height and width of the ridge design on friction can be further explained by considering the tissue's resistance pressure on the capsule. As the ridge height increased, the ridges penetrated more deeply into the soft tissue surface, causing localizes deformation around the ridges and increasing deformation friction. The contact pressure surfaces, generated greater compressive forces that required more energy for the tissue to deform and recover as the capsule moved. Additionally, with the addition of ridges, the real contact area between the capsule and the tissue surface are likely increased. Although the capsule surface between the ridges may not have been in full contact with the tissue during sliding, the ridge protrusions engaged more deeply, thereby enhancing the overall contact area. This larger real contact area increased the number of molecular junctions between the capsule and the tissue, which, in turn, raised the adhesion friction.

A comparison of the results for ridge height and width reveals that ridge height had a more significant effect on the COF compared to ridge width. As a result, the ridge design with a height of 1 mm and a width of 0.5 mm demonstrated the greatest frictional resistance among all the ridge designs tested. Taller ridges penetrated more deeply into the tissue, resulting in greater deformation friction and larger real contact areas. In contrast, wider ridges increased the contact area but distributed the load more evenly across the tissue surface, reducing tissue resistance and leading to a trend of decreasing COF. This phenomenon has implications for tissue damage associated with this type of ridge design. Although no clear scratch scars were observed, the pronounced pressure points against the tissue caused by the larger ridge height could have potentially damaged the tissue's surface layer, particularly in more vulnerable lesion areas. The increased ridge width might help reduce this risk by distributing the pressure more evenly. However, it is important to determine the specific frictional forces and COF required for practical applications to better understand the potential risks and benefits.

Higher surface roughness values of the capsule were expected to increase the microscopic real contact area between the capsule and the tissue. The rougher surface created additional peaks and valleys, allowing for more molecular interactions and raising adhesion friction. Furthermore, the peaks of the rough surface caused microdeformation of the soft tissue as they pressed into it, increasing deformation friction

during sliding. Although no statistical difference was observed between capsules with different surface roughness values, a trend was still observed, albeit to a lesser extent compared to the ridge design. This result suggests increasing the number of experiments to verify the experimental hypothesis.

Overall, modifying the ridge design and adjusting the surface roughness of the capsule shell appear feasible for slowing the travel speed of the capsule for better diagnosis accuracy, as these factors significantly influence friction resistance. However, the true performance must be validated through in vivo testing. Additionally, the outcomes should be assessed to determine whether the capsule experiences excessive friction, potentially causing it to become stuck in the small intestine, and whether it could damage the lesion, both of which would have undesirable consequences. In this context, further development and investigation into altered ridge height and width designs are necessary to obtain the feasible design that meets the clinical requirement.

6.7 Conclusions

The experimental methodology employed in this chapter successfully obtained stable and continuous friction data, indicating that it was capable of generating meaningful results and providing a reliable basis for further exploring the frictional characteristics between capsule robots and small intestinal tissues.

Summary of frictional behaviour which is likely due to one or more of the following mechanisms, possibly combined:

- The static friction coefficient of small intestinal tissues is generally higher than the kinetic friction coefficient, which results from the combined effects of adhesion, deformation of the tissue surface microstructure, and mucus lubrication.
- Several factors such as machine measurement errors could contribute to the observed stick-slip-like phenomenon in the friction curves. A hypothesis of two potential types of stick-slip mechanisms during capsule movement were considered. Minor, continuous noise-like fluctuations are likely caused by the interface shear strength, while larger, more pronounced up-and-down fluctuations are attributed to tissue deformation. These considered effects require further verification.

Effects of parameter changes:

- Capsule Size: Altering the diameter and length of the capsule within a small range has minimal impact on the friction coefficient; however, additional datasets are required to draw a definitive conclusion. Based on conclusions regarding capsule orientations, increasing the capsule size beyond certain limits would definitely result in significantly higher friction. These conclusions require further verification.

- Capsule Orientation: The greater the deviation of the capsule orientation from the horizontal axis, the higher the friction coefficient. When the orientation is 90°, the static and kinetic friction coefficients increase caused by greater deformation resistance from intestine.

- Sliding Speed and Load: An increase in the normal load leads to a decrease in the friction coefficient but an increase in the frictional force; an increase in the sliding speed results in an increase in the friction coefficient.

- Ridge Design and Surface Roughness: The ridge design significantly affects friction, with an increase in height leading to an increase in the friction coefficient, while the effect of width is relatively small; the impact of surface roughness on the friction coefficient is not obvious and present no statistical difference, but there is a tendency for it to increase. Although friction coefficients are observed larger caused by ridge designs, further in vivo verification tests are essential to comprehensively validate the feasibility of these designs.

Significance for future CE development:
Understanding these frictional characteristics and parameter effects is crucial for optimizing capsule design. For instance, selecting the appropriate size, controlling small movement orientation angle, and adjusting low speed and load from the robot object moving through a tubular intestine can reduce the risk of capsule retention. Additionally, the design of appropriate ridge structures on the outer shell of capsule robots can significantly enhance frictional resistance. Such modifications may help slow down capsule transit speed or improve traction for actively controlled capsule robots, thereby reducing the risk of slipping. The findings from this study suggest that a ridge height-to-width ratio of 2:1 offers the most effective performance. This insight contributes to the advancement of clinical applications by informing future surface design strategies for capsule-based robotic systems.

Chapter 7

Conclusions, Limitations, and Future Work

7.1 Conclusions with novel findings

This thesis systematically investigates the mechanical and frictional interactions between capsule endoscopy devices and intestinal tissue, and introduces several methodological and design advances:

1. Mechanical characterization of porcine intestinal tissue

A viscoelastic characterization of porcine small intestinal tissue was conducted via indentation tests at varying strain rates. The tissue exhibited a strain rate-dependent stiffening behaviour and reduced viscosity at higher rates. These findings were quantified through curve-fitting models, providing critical data to inform material selection for the substrate of the friction test platform.

2. Development of a friction testing platform

A novel and reproducible friction testing platform was designed to study capsule-tissue interactions under controlled experimental conditions. This setup, based on data from the mechanical characterization, allowed for controlled variation of capsule orientation, speed, and applied load. Its adaptability makes it a valuable tool for broader soft tissue–device research beyond capsule endoscopy.

3. Mucus and friction behaviour

The presence of both mucin solutions and PBS significantly reduced the friction coefficient compared to low-hydration conditions. However, no statistically significant

difference was observed between mucin-containing samples of varying concentrations or pH and the PBS control. This suggests that, under the current experimental setup, mucus does not offer superior lubrication performance over PBS, despite its biological relevance. Based on the lubrication mechanisms of soft biological interfaces and analysis of the experimental data, it is hypothesized that hydration lubrication is the predominant mechanism under soft, hydrated contact conditions, contributing to minimized frictional resistance. However, this hypothesis requires further validation using physiologically representative mucus. Although experiments using artificial mucus with varying mucin concentrations and pH levels revealed trends indicating that higher mucin concentrations and lower pH values may reduce frictional resistance, these differences were not statistically significant.

4. Capsule sliding behaviour and implications for their future development

The frictional experiments conducted in this study yielded several previously unreported insights that advance the understanding of mechanical interactions between capsule robots and intestinal tissues. The study hypothesizes the existence of two distinct stick-slip behaviours during capsule sliding: (1) micro-scale fluctuations, attributed to shear resistance at the interface level likely influenced by mucus dynamics and villi interactions, and (2) macro-scale fluctuations, caused by larger-scale tissue deformation as the capsule intermittently overcomes mechanical resistance. This dual-mode interpretation provides a more nuanced framework for understanding friction irregularities commonly observed in ex vivo experiments. The finding that increasing normal load reduced the friction coefficient suggests the possible presence of fluid drainage from the tissue under compression. As load increases, local interstitial fluid may be expelled, decreasing surface adhesion and enhancing the hydration lubrication and fluid-film lubrication potentially. The observed increase in friction coefficient with sliding speed highlights the coupled contributions of adhesion and deformation mechanisms, demonstrating that both the transient capsule-tissue interactions and the viscoelastic response of the intestinal tissue govern frictional resistance under dynamic conditions. Further understanding was developed in terms of the relationship between capsule orientation and friction magnitude. Specifically, an orientation with a maximized leading edge (90° between the capsule and intestine axial dimensions) leads to the highest friction coefficient due to increased tissue resistance and reduced alignment with natural intestinal folds. The ridge design exhibited a highly nonlinear

influence on friction, with ridge height being a dominant factor over width. In particular, a 2:1 height-to-width ratio was found to provide the most stable and elevated friction profile, likely due to enhanced mechanical interlocking with intestinal folds. This improved understanding of capsule sliding behaviour and the effect of dimension and surface profiles can aid the development of future capsule designs.

7.2 Limitations

Despite the contributions above, several limitations constrain the generalizability and realism of the results:

- **Tissue preparation constraints:** Intestinal tissues were tested in an open, flattened state, which omits natural hoop stresses and may affect friction results.
- **Mechanical testing accuracy:** Errors in tissue thickness measurement may have introduced inaccuracies in the calculated stress-strain relationships.
- **High sample variability and insufficient dataset:** Significant variability in the surface properties of intestinal tissue was observed between different samples. This variability introduces uncertainty and may contribute to the lack of statistical significance in the observed trends. Additionally, the limited dataset restricts the statistical power of the analysis, reducing the confidence in the conclusions drawn.
- **Ex vivo limitations:** The lack of blood flow, neural regulation, and peristaltic activity in ex vivo tissues limits physiological fidelity.
- **Simplified mucus model:** Artificial mucus lacked the complexity and variability of native intestinal secretions, including the presence of chyme and other biological residues. Therefore, the simplified test conditions may not fully capture the dynamic lubrication effects present in vivo.
- **Friction test limitations:** The real contact area and stick-slip behaviour were not directly observable, limiting full understanding of tribological mechanisms.
- **No trauma quantification:** Tissue damage from capsule sliding was not quantitatively assessed due to the absence of histological analysis.
- **Scope limited to healthy tissue:** Pathological tissue states such as ulcers, bleeding, or strictures were not included, reducing clinical relevance.

7.3 Future Work

To build on the current research, the following directions are recommended:

1. Improved mucus simulation

Future studies should incorporate:

- Intestinal fluids extracted from live animals or synthetic mucus formulations and chyme simulation that mimic native biochemistry.
- Higher mucin concentrations and a broader range of pH values.
- In situ imaging to visualize contact mechanics during sliding.

2. Consideration of pathological tissue states

Experiments should be expanded to include:

- Diseased tissues with different stiffness, thickness, and surface features.
- Simulated conditions such as bleeding and damaged mucosal layers.
- Evaluation of capsule performance in therapeutic tasks such as biopsy, drug delivery, and lesion marking.

3. Texture design and friction modulation

To further enhance capsule design, future research should explore:

- Bioinspired surface textures (e.g., gecko feet, shark skin, lotus leaf).
- Dynamic surface control via stimuli-responsive materials (e.g., magnetic, pneumatic, or pressure-sensitive actuation).
- Controllable friction zones for adapting to anatomical variations.
- Development of finite element analysis models of the intestine for virtual testing.

4. Trauma assessment methods

Further studies should incorporate histological and microscopic techniques to:

- Quantify tissue damage and classify trauma severity.
- Develop safety thresholds for capsule contact forces and velocities.

Appendices

Appendix A

15 cycles of preconditioning tests

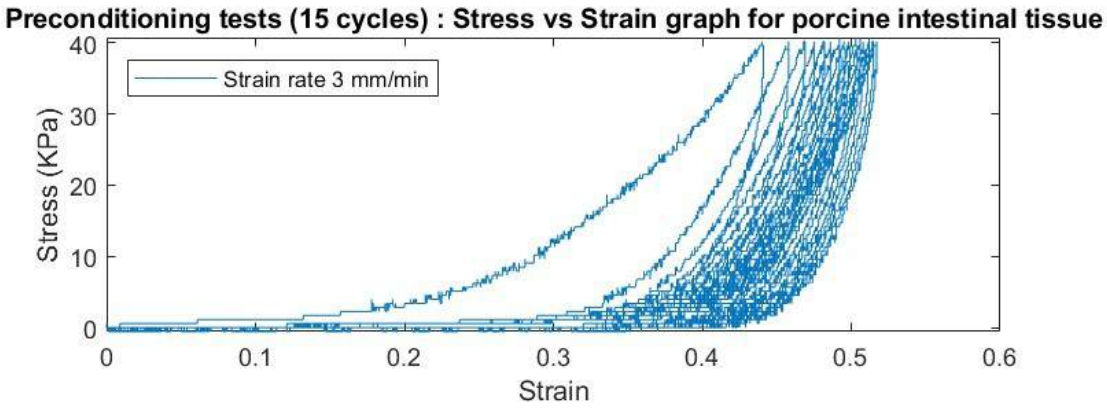

(a)

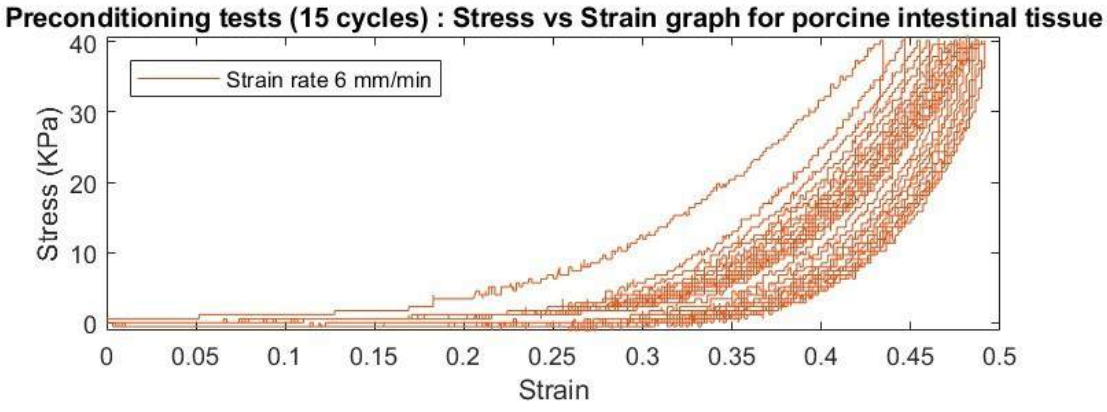

(b)

Figure A.1: Stress-train response of the 15 loading cycles of porcine intestinal tissue: (a) Loading speed of 3 mm/min; (b) Loading speed of 6 mm/min.

Appendix B

Original Stress vs Time graph of stress relaxation test for porcine and SynDaver synthetic tissue

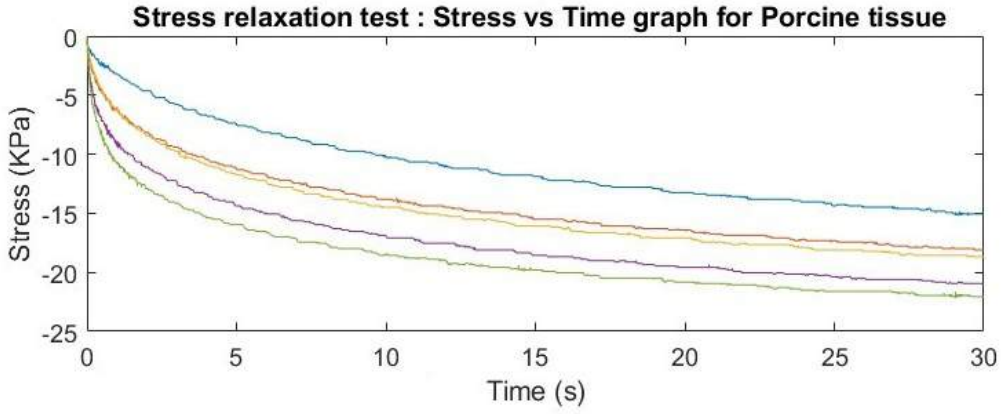

(a)

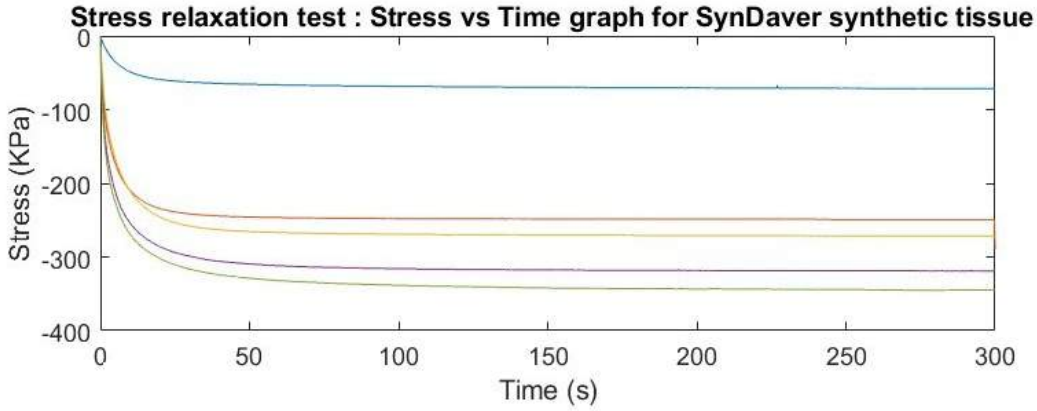

(b)

Figure B.1: Stress relaxation test: Stress vs Time graph for porcine and SynDaver intestinal tissue.

Appendix C

Tissue surface measurements

Sample No.	Length (mm)	Height (um)
1	2.096	692.029
2	1.421	1050
3	2.001	941.018
4	1.342	1234
5	2.210	843.536
6	2.455	438.624
7	1.957	300.964
8	1.560	281.414
9	2.223	490.597
10	2.195	631.451
11	1.540	823.491
12	2.755	710.394
Average	1.980	703.1
Standard deviation	435.7	294.335

Table C.1: Sample Measurements: Folds' Length and Height

Appendix D

Technical drawings of designed testbed components

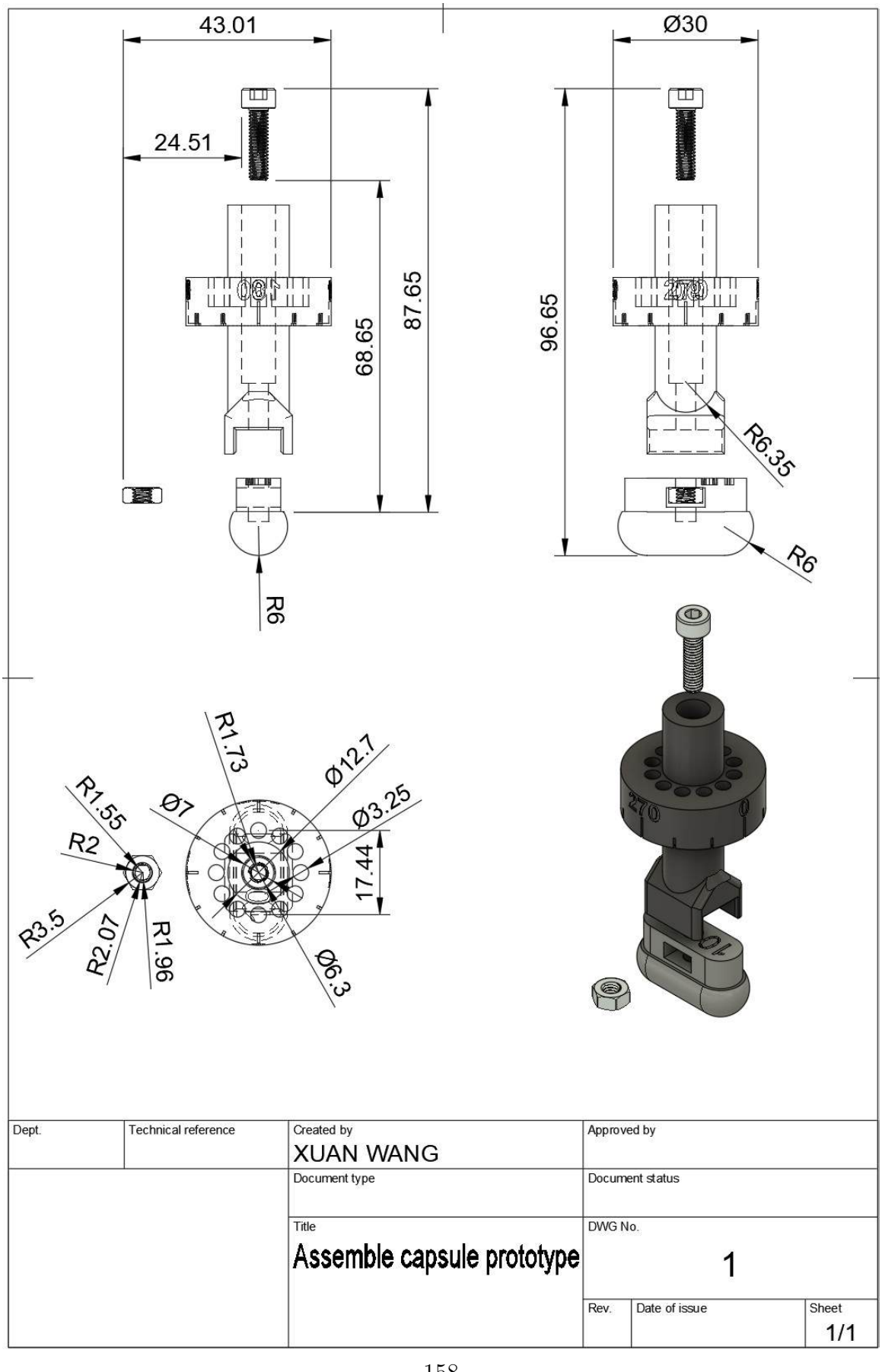

Figure D.1: Technical drawings of the angle holder with the detachable capsule

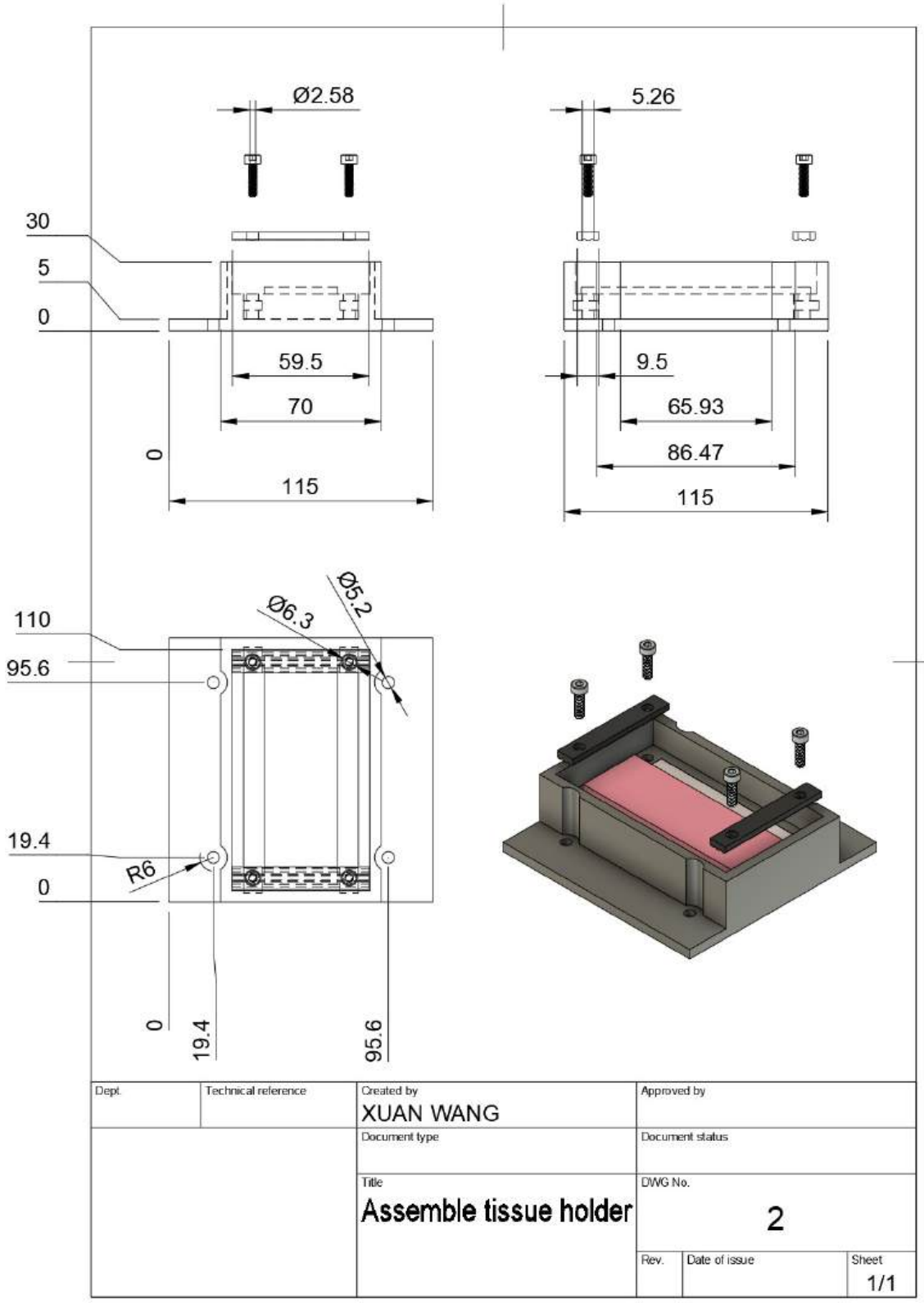

Figure D.2: Technical drawings of the tissue holder

Appendix E

Graphs of the first four cycles for normal load, friction force, and COF values of the consistency tests.

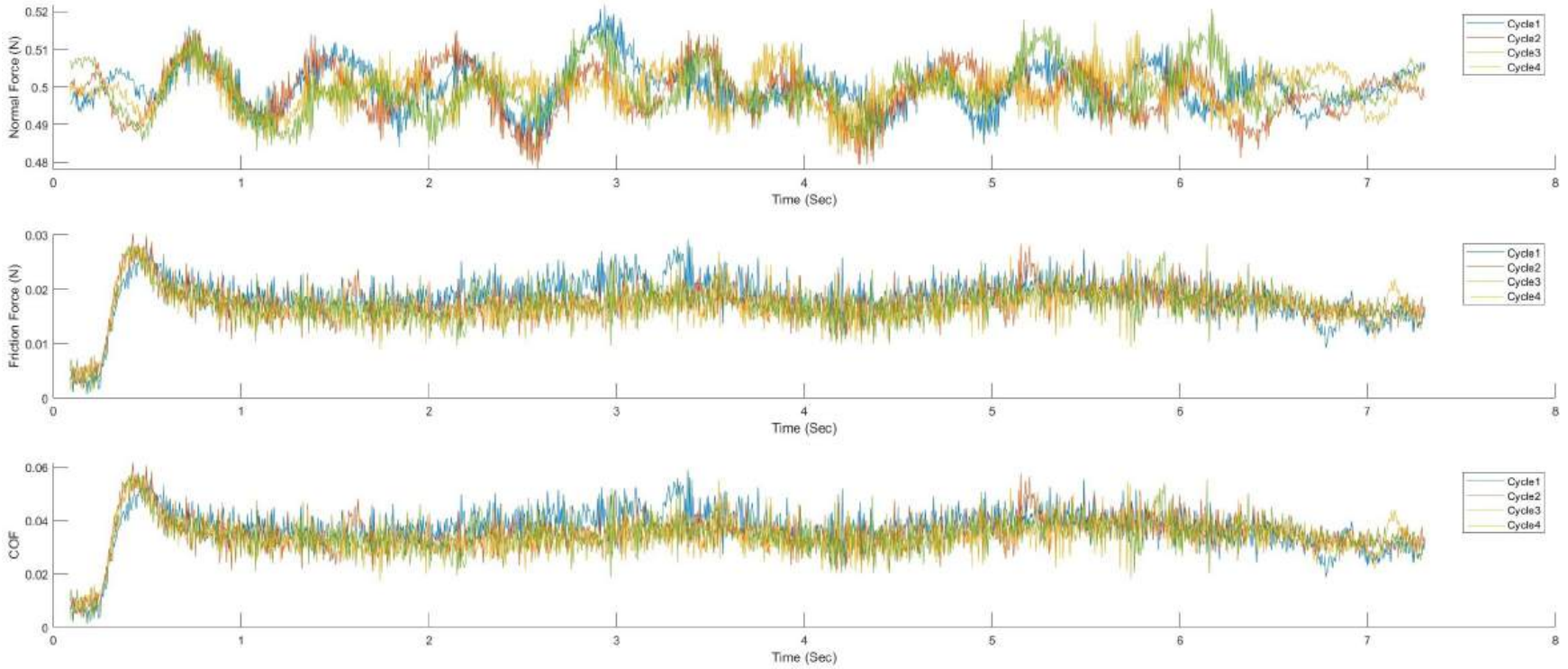

Figure E.1: From top to bottom, the sliding results of the first four cycles for normal load, friction force, and COF values are shown from the consistency tests.

Appendix F

Descriptive statistics tables of mucus test results

	PBS	1 mg/ml	5 mg/ml	10 mg/ml	15 mg/ml
Number of values	9	12	9	9	9
Minimum	0.04800	0.04286	0.04112	0.03014	0.04342
25% Percentile	0.05350	0.06146	0.05006	0.04224	0.04769
Median	0.07900	0.07713	0.06800	0.05607	0.05150
75% Percentile	0.09355	0.09803	0.08766	0.06853	0.07906
Maximum	0.1450	0.1449	0.1316	0.1222	0.1016
Range	0.09700	0.1020	0.09053	0.09202	0.05819
Mean	0.07978	0.08195	0.07253	0.05977	0.06214
Std. Deviation	0.03028	0.02728	0.02809	0.02678	0.02048
Std. Error of Mean	0.01009	0.007874	0.009362	0.008926	0.006827

Table F.1: Mucin concentration tests: Static friction

	PBS	1 mg/ml	5 mg/ml	10 mg/ml	15 mg/ml
Number of values	9	12	9	9	9
Minimum	0.02600	0.01261	0.02821	0.02732	0.009567
25% Percentile	0.03150	0.03236	0.03078	0.03168	0.02782
Median	0.05500	0.05475	0.04491	0.03614	0.03449
75% Percentile	0.08550	0.07660	0.07296	0.05244	0.04689
Maximum	0.1330	0.1363	0.1064	0.09530	0.05995
Range	0.1070	0.1237	0.07817	0.06798	0.05038
Mean	0.06311	0.05788	0.05325	0.04490	0.03592
Std. Deviation	0.03502	0.03362	0.02663	0.02095	0.01448
Std. Error of Mean	0.01167	0.009706	0.008876	0.006982	0.004826

Table F.2: Mucin concentration tests: Kinetic friction

	pH 3.71	pH 6.00	pH 7.50
Number of values	9	9	9
Minimum	0.06358	0.06126	0.06765
Maximum	0.09188	0.08959	0.08966
Range	0.02830	0.02833	0.02201
Mean	0.07376	0.07447	0.07843
Std. Deviation	0.01027	0.01153	0.007017
Std. Error of Mean	0.003422	0.003844	0.002339

Table F.3: Mucus pH tests: Static friction

	pH 3.71	pH 6.00	pH 7.50
Number of values	9	9	9
Minimum	0.03321	0.04257	0.03634
Maximum	0.05831	0.06301	0.06802
Range	0.02510	0.02045	0.03168
Mean	0.04764	0.05031	0.05086
Std. Deviation	0.008299	0.007663	0.009202
Std. Error of Mean	0.002766	0.002554	0.003067

Table F.4: Mucus pH tests: Kinetic friction

Appendix G

Descriptive statistics tables of capsule properties test results

	Static	Kinetic
Number of values	36	36
Minimum	0.04580	0.02567
25% Percentile	0.05892	0.03497
Median	0.07856	0.04283
75% Percentile	0.1108	0.05712
Maximum	0.1614	0.09781
Range	0.1156	0.07214
Mean	0.08599	0.04766
Std. Deviation	0.03172	0.01816
Std. Error of Mean	0.005286	0.003027

Table G.1: Static and kinetic COF results of all 36 tests.

Table G.2: Post-hoc tests results reveal which sample groups exhibited statistically significant differences in static COF.

Tukey's multiple comparisons test	Mean diff.	95.00% CI of diff.	Below threshold?	Summary	Adjusted P Value
1A vs. 1B	-0.002918	-0.04033 to 0.03449	No	ns	>0.9999
1A vs. 2A	-0.06209	-0.09949 to -0.02468	Yes	***	0.0002
1A vs. 2B	-0.06404	-0.1014 to -0.02663	Yes	***	0.0001
1A vs. 3A	-0.02289	-0.06030 to 0.01452	No	ns	0.5608
1A vs. 3B	-0.02633	-0.06374 to 0.01108	No	ns	0.3643
1A vs. 4A	-0.03060	-0.06801 to 0.006807	No	ns	0.1852
1A vs. 4B	-0.03255	-0.06996 to 0.004860	No	ns	0.1305
1A vs. 5A	-0.008446	-0.04586 to 0.02896	No	ns	0.9994
1A vs. 5B	-0.01222	-0.04963 to 0.02519	No	ns	0.9860
1A vs. 6A	-0.06811	-0.1055 to -0.03070	Yes	****	<0.0001
1A vs. 6B	-0.09866	-0.1361 to -0.06125	Yes	****	<0.0001
1B vs. 2A	-0.05917	-0.09658 to -0.02176	Yes	***	0.0004
1B vs. 2B	-0.06112	-0.09853 to -0.02371	Yes	***	0.0002
1B vs. 3A	-0.01997	-0.05738 to 0.01744	No	ns	0.7342
1B vs. 3B	-0.02342	-0.06083 to 0.01399	No	ns	0.5288
1B vs. 4A	-0.02768	-0.06509 to 0.009725	No	ns	0.2986
1B vs. 4B	-0.02963	-0.06704 to 0.007778	No	ns	0.2186
1B vs. 5A	-0.005528	-0.04294 to 0.03188	No	ns	>0.9999
1B vs. 5B	-0.009302	-0.04671 to 0.02811	No	ns	0.9985
1B vs. 6A	-0.06520	-0.1026 to -0.02779	Yes	****	<0.0001
1B vs. 6B	-0.09574	-0.1331 to -0.05833	Yes	****	<0.0001
2A vs. 2B	-0.001951	-0.03936 to 0.03546	No	ns	>0.9999
2A vs. 3A	0.03920	0.001790 to 0.07661	Yes	*	0.0343
2A vs. 3B	0.03575	-0.001658 to 0.07316	No	ns	0.0702
2A vs. 4A	0.03148	-0.005926 to 0.06889	No	ns	0.1586
2A vs. 4B	0.02954	-0.007874 to 0.06695	No	ns	0.2221
2A vs. 5A	0.05364	0.01623 to 0.09105	Yes	**	0.0013
2A vs. 5B	0.04987	0.01246 to 0.08728	Yes	**	0.0031
2A vs. 6A	-0.006029	-0.04344 to 0.03138	No	ns	>0.9999
2A vs. 6B	-0.03657	-0.07398 to 0.0008375	No	ns	0.0594
2B vs. 3A	0.04115	0.003740 to 0.07856	Yes	*	0.0225
2B vs. 3B	0.03770	0.0002929 to 0.07511	Yes	*	0.0470
2B vs. 4A	0.03343	-0.003976 to 0.07084	No	ns	0.1105
2B vs. 4B	0.03149	-0.005923 to 0.06890	No	ns	0.1585
2B vs. 5A	0.05559	0.01818 to 0.09300	Yes	***	0.0008
2B vs. 5B	0.05182	0.01441 to 0.08923	Yes	**	0.0020
2B vs. 6A	-0.004078	-0.04149 to 0.03333	No	ns	>0.9999
2B vs. 6B	-0.03462	-0.07203 to 0.002788	No	ns	0.0878
3A vs. 3B	-0.003447	-0.04086 to 0.03396	No	ns	>0.9999
3A vs. 4A	-0.007716	-0.04513 to 0.02969	No	ns	0.9997
3A vs. 4B	-0.009663	-0.04707 to 0.02775	No	ns	0.9979
3A vs. 5A	0.01444	-0.02297 to 0.05185	No	ns	0.9542
3A vs. 5B	0.01067	-0.02674 to 0.04808	No	ns	0.9952
3A vs. 6A	-0.04523	-0.08264 to -0.007818	Yes	**	0.0091
3A vs. 6B	-0.07577	-0.1132 to -0.03836	Yes	****	<0.0001
3B vs. 4A	-0.004269	-0.04168 to 0.03314	No	ns	>0.9999
3B vs. 4B	-0.006216	-0.04363 to 0.03119	No	ns	>0.9999
3B vs. 5A	0.01789	-0.01952 to 0.05530	No	ns	0.8404
3B vs. 5B	0.01411	-0.02330 to 0.05152	No	ns	0.9606
3B vs. 6A	-0.04178	-0.07919 to -0.004371	Yes	*	0.0196
3B vs. 6B	-0.07232	-0.1097 to -0.03491	Yes	****	<0.0001
4A vs. 4B	-0.001947	-0.03936 to 0.03546	No	ns	>0.9999
4A vs. 5A	0.02216	-0.01525 to 0.05957	No	ns	0.6051
4A vs. 5B	0.01838	-0.01903 to 0.05579	No	ns	0.8174
4A vs. 6A	-0.03751	-0.07492 to -0.0001022	Yes	*	0.0489
4A vs. 6B	-0.06806	-0.1055 to -0.03065	Yes	****	<0.0001
4B vs. 5A	0.02410	-0.01331 to 0.06151	No	ns	0.4879
4B vs. 5B	0.02033	-0.01708 to 0.05774	No	ns	0.7137
4B vs. 6A	-0.03556	-0.07297 to 0.001845	No	ns	0.0729
4B vs. 6B	-0.06611	-0.1035 to -0.02870	Yes	****	<0.0001
5A vs. 5B	-0.003774	-0.04118 to 0.03364	No	ns	>0.9999
5A vs. 6A	-0.05967	-0.09708 to -0.02226	Yes	***	0.0003
5A vs. 6B	-0.09021	-0.1276 to -0.05280	Yes	****	<0.0001
5B vs. 6A	-0.05589	-0.09330 to -0.01848	Yes	***	0.0008
5B vs. 6B	-0.08644	-0.1238 to -0.04903	Yes	****	<0.0001
6A vs. 6B	-0.03054	-0.06795 to 0.006866	No	ns	0.1872

Table G.3: Post-hoc tests results reveal which sample groups exhibited statistically significant differences in kinetic COF.

Tukey's multiple comparisons test	Mean diff.	95.00% CI of diff.	Below threshold?	Summary	Adjusted P Value
1A vs. 1B	-0.007006	-0.04111 to 0.02710	No	ns	0.9997
1A vs. 2A	-0.02857	-0.06267 to 0.005533	No	ns	0.1626
1A vs. 2B	-0.02602	-0.06013 to 0.008080	No	ns	0.2610
1A vs. 3A	-0.006940	-0.04104 to 0.02716	No	ns	0.9998
1A vs. 3B	-0.01277	-0.04688 to 0.02133	No	ns	0.9625
1A vs. 4A	-0.02012	-0.05422 to 0.01399	No	ns	0.6105
1A vs. 4B	-0.01730	-0.05140 to 0.01681	No	ns	0.7879
1A vs. 5A	-0.01464	-0.04875 to 0.01946	No	ns	0.9113
1A vs. 5B	-0.009002	-0.04311 to 0.02510	No	ns	0.9975
1A vs. 6A	-0.03641	-0.07051 to -0.002304	Yes	*	0.0293
1A vs. 6B	-0.05643	-0.09053 to -0.02233	Yes	***	0.0002
1B vs. 2A	-0.02156	-0.05567 to 0.01254	No	ns	0.5145
1B vs. 2B	-0.01902	-0.05312 to 0.01509	No	ns	0.6829
1B vs. 3A	6.667e-005	-0.03404 to 0.03417	No	ns	>0.9999
1B vs. 3B	-0.005766	-0.03987 to 0.02834	No	ns	>0.9999
1B vs. 4A	-0.01311	-0.04721 to 0.02099	No	ns	0.9554
1B vs. 4B	-0.01029	-0.04439 to 0.02381	No	ns	0.9924
1B vs. 5A	-0.007635	-0.04174 to 0.02647	No	ns	0.9994
1B vs. 5B	-0.001995	-0.03610 to 0.03211	No	ns	>0.9999
1B vs. 6A	-0.02940	-0.06351 to 0.004702	No	ns	0.1379
1B vs. 6B	-0.04943	-0.08353 to -0.01532	Yes	**	0.0011
2A vs. 2B	0.002547	-0.03156 to 0.03665	No	ns	>0.9999
2A vs. 3A	0.02163	-0.01247 to 0.05573	No	ns	0.5102
2A vs. 3B	0.01580	-0.01831 to 0.04990	No	ns	0.8646
2A vs. 4A	0.008454	-0.02565 to 0.04256	No	ns	0.9986
2A vs. 4B	0.01128	-0.02283 to 0.04538	No	ns	0.9846
2A vs. 5A	0.01393	-0.02017 to 0.04803	No	ns	0.9343
2A vs. 5B	0.01957	-0.01453 to 0.05367	No	ns	0.6468
2A vs. 6A	-0.007837	-0.04194 to 0.02627	No	ns	0.9993
2A vs. 6B	-0.02786	-0.06196 to 0.006243	No	ns	0.1866
2B vs. 3A	0.01908	-0.01502 to 0.05319	No	ns	0.6785
2B vs. 3B	0.01325	-0.02085 to 0.04735	No	ns	0.9522
2B vs. 4A	0.005906	-0.02820 to 0.04001	No	ns	>0.9999
2B vs. 4B	0.008728	-0.02538 to 0.04283	No	ns	0.9981
2B vs. 5A	0.01138	-0.02272 to 0.04549	No	ns	0.9835
2B vs. 5B	0.01702	-0.01708 to 0.05113	No	ns	0.8032
2B vs. 6A	-0.01038	-0.04449 to 0.02372	No	ns	0.9919
2B vs. 6B	-0.03041	-0.06451 to 0.003696	No	ns	0.1122
3A vs. 3B	-0.005833	-0.03994 to 0.02827	No	ns	>0.9999
3A vs. 4A	-0.01318	-0.04728 to 0.02093	No	ns	0.9539
3A vs. 4B	-0.01036	-0.04446 to 0.02375	No	ns	0.9920
3A vs. 5A	-0.007702	-0.04181 to 0.02640	No	ns	0.9994
3A vs. 5B	-0.002062	-0.03617 to 0.03204	No	ns	>0.9999
3A vs. 6A	-0.02947	-0.06357 to 0.004635	No	ns	0.1360
3A vs. 6B	-0.04949	-0.08360 to -0.01539	Yes	**	0.0011
3B vs. 4A	-0.007345	-0.04145 to 0.02676	No	ns	0.9996
3B vs. 4B	-0.004523	-0.03863 to 0.02958	No	ns	>0.9999
3B vs. 5A	-0.001869	-0.03597 to 0.03223	No	ns	>0.9999
3B vs. 5B	0.003771	-0.03033 to 0.03787	No	ns	>0.9999
3B vs. 6A	-0.02364	-0.05774 to 0.01047	No	ns	0.3856
3B vs. 6B	-0.04366	-0.07776 to -0.009555	Yes	**	0.0049
4A vs. 4B	0.002821	-0.03128 to 0.03692	No	ns	>0.9999
4A vs. 5A	0.005476	-0.02863 to 0.03958	No	ns	>0.9999
4A vs. 5B	0.01112	-0.02299 to 0.04522	No	ns	0.9862
4A vs. 6A	-0.01629	-0.05039 to 0.01781	No	ns	0.8413
4A vs. 6B	-0.03631	-0.07042 to -0.002210	Yes	*	0.0299
4B vs. 5A	0.002654	-0.03145 to 0.03676	No	ns	>0.9999
4B vs. 5B	0.008294	-0.02581 to 0.04240	No	ns	0.9988
4B vs. 6A	-0.01911	-0.05322 to 0.01499	No	ns	0.6767
4B vs. 6B	-0.03914	-0.07324 to -0.005032	Yes	*	0.0152
5A vs. 5B	0.005640	-0.02846 to 0.03974	No	ns	>0.9999
5A vs. 6A	-0.02177	-0.05587 to 0.01234	No	ns	0.5014
5A vs. 6B	-0.04179	-0.07589 to -0.007686	Yes	**	0.0079
5B vs. 6A	-0.02741	-0.06151 to 0.006697	No	ns	0.2033
5B vs. 6B	-0.04743	-0.08153 to -0.01333	Yes	**	0.0019
6A vs. 6B	-0.02002	-0.05413 to 0.01408	No	ns	0.6168

Bibliography

[1] A. D. Sperber, S. I. Bangdiwala, D. A. Drossman, U. C. Ghoshal, M. Simren, J. Tack, W. E. Whitehead, D. L. Dumitrascu, X. Fang, S. Fukudo, J. Kellow, E. Okeke, E. M. Quigley, M. Schmulson, P. Whorwell, T. Archampong, P. Adibi, V. Andresen, M. A. Benninga, B. Bonaz, S. Bor, L. B. Fernandez, S. C. Choi, E. S. Corazziari, C. Francisconi, A. Hani, L. Lazebnik, Y. Y. Lee, A. Mulak, M. M. Rahman, J. Santos, M. Setshedi, A. F. Syam, S. Vanner, R. K. Wong, A. Lopez-Colombo, V. Costa, R. Dickman, M. Kanazawa, A. H. Keshteli, R. Khatun, I. Maleki, P. Poitras, N. Pratap, O. Stefanyuk, S. Thomson, J. Zeevenhooven, and O. S. Palsson, "Worldwide Prevalence and Burden of Functional Gastrointestinal Disorders, Results of Rome Foundation Global Study," *Gastroenterology*, vol. 160, no. 1, pp. 99–114, 2021.

[2] J. Hu, X. Wang, and S. Sun, "Comparison between the widely used magnetically controlled capsule gastroscopy and conventional gastroscopy: a meta-analysis," *Minim. Invasive Ther. Allied Technol.*, vol. 31, no. 4, pp. 496–504, 2022.

[3] G. Ciuti, R. Caliò, D. Camboni, L. Neri, F. Bianchi, A. Arezzo, A. Koulaouzidis, S. Schostek, D. Stoyanov, C. M. Oddo, B. Magnani, A. Menciassi, M. Morino, M. O. Schurr, and P. Dario, "Frontiers of robotic endoscopic capsules: a review," *J. Micro-Bio Robot.*, vol. 11, no. 1-4, pp. 1–18, 2016.

[4] Z. Liao, R. Gao, C. Xu, and Z. S. Li, "Indications and detection, completion, and retention rates of small-bowel capsule endoscopy: a systematic review," *Gastrointest. Endosc.*, vol. 71, no. 2, pp. 280–286, 2010.

[5] H. Chen, Z. Zhang, M. Zhang, D. Wang, M. Jia, and B. Feng, "Capsule endoscopy with retention of 4 years: A case report," *Int. J. Surg. Case Rep.*, vol. 95, 2022.

[6] M. Rezapour, C. Amadi, and L. B. Gerson, "Retention associated with video capsule endoscopy: systematic review and meta-analysis," *Gastrointest. Endosc.*, vol. 85, no. 6, pp. 1157–1168, 2017.

[7] S. F. Pasha, M. Pennazio, E. Rondonotti, D. Wolf, M. R. Buras, J. G. Albert, S. A. Cohen, J. Cotter, G. D'Haens, R. Eliakim, D. T. Rubin, and J. A. Leighton, "Capsule Retention in Crohn's Disease: A Meta-analysis," *Inflamm. Bowel Dis.*, vol. 26, no. 1, pp. 33–42, 2020.

[8] L. Xin, Z. Liao, Y. Du, Y. Jiang, and Z. Li, "Retained capsule endoscopy causing intestinal obstruction - Endoscopic retrieval by retrograde single-balloon enteroscopy," *J. Interv. Gastroenterol.*, vol. 2, no. 1, p. 15, 2012.

[9] P. K. Sasmal, P. C. Das, O. Tantia, N. Patle, S. Khanna, and B. Sen, "Acute Small Intestinal Obstruction—An Unusual Complication of Capsule Endoscopy," *Indian J. Surg.*, vol. 77, no. Suppl 1, pp. 21–23, 2015.

[10] W. G. Kwack and Y. J. Lim, "Current Status and Research into Overcoming Limitations of Capsule Endoscopy," *Clin. Endosc.*, vol. 49, no. 1, pp. 8–15, 2016.

[11] F. P. Bowden and D. Tabor, *The Friction and Lubrication of Solids*. Oxford University Press, reprint ed., 2001.

[12] S. Derler and L. C. Gerhardt, "Tribology of Skin: Review and Analysis of Experimental Results for the Friction Coefficient of Human Skin," *Tribol. Lett.*, vol. 45, no. 1, pp. 1–27, 2011.

[13] M. Barquins and D. Maugis, "Tackiness of elastomers," *J. Adhes.*, vol. 13, no. 1, pp. 53–65, 1981.

[14] V. J. Schömig, B. T. Käsdorf, C. Scholz, K. Bidmon, O. Lieleg, and S. Berensmeier, "An optimized purification process for porcine gastric mucin with preservation of its native functional properties," *RSC Adv.*, vol. 6, no. 50, pp. 44932–44943, 2016.

[15] B. J. Hamrock, S. R. Schmid, and B. O. Jacobson, "Fundamentals of Fluid Film Lubrication," *Fundam. Fluid Film Lubr.*, 2004.

[16] J. W. Robinson, Y. Zhou, P. Bhattacharya, R. Erck, J. Qu, J. T. Bays, and L. Cosimbescu, "Probing the molecular design of hyper-branched aryl polyesters towards lubricant applications," *Sci. Rep.*, vol. 6, 2016.

[17] K. L. Johnson, K. Kendall, and A. D. Roberts, "Surface energy and the contact of elastic solids," *Proc. R. Soc. London. A. Math. Phys. Sci.*, vol. 324, no. 1558, pp. 301–313, 1971.

[18] B. Derjaguin, V. Muller, and Y. Toporov, "Effect of contact deformations on the adhesion of particles," *J. Colloid Interface Sci.*, vol. 53, no. 2, pp. 314–326, 1975.

[19] B. N. Persson, "Theory of rubber friction and contact mechanics," *J. Chem. Phys.*, vol. 115, no. 8, pp. 3840–3861, 2001.

[20] S. Stupkiewicz, J. Lengiewicz, P. Sadowski, and S. Kucharski, "Finite deformation effects in soft elastohydrodynamic lubrication problems," *Tribol. Int.*, vol. 93, pp. 511–522, 2016.

[21] G. Iddan, G. Meron, A. Glukhovsky, and P. Swain, "Wireless capsule endoscopy," *Nature*, vol. 405, no. 6785, pp. 417–418, 2000.

[22] R. Eliakim, A. Suissa, K. Yassin, D. Katz, and D. Fischer, "Wireless capsule video endoscopy compared to barium follow-through and computerised tomography in patients with suspected Crohn's disease - Final report," *Dig. Liver Dis.*, vol. 36, no. 8, pp. 519–522, 2004.

[23] G. Pan and L. Wang, "Swallowable wireless capsule endoscopy: Progress and technical challenges," *Gastroenterol. Res. Pract.*, vol. 2012, 2012.

[24] H. Nuutinen, K. L. Kolho, P. Salminen, R. Rintala, J. Koskenpato, A. Koivusalo, T. Sipponen, and M. Färkkilä, "Capsule endoscopy in pediatric patients: technique and results in our first 100 consecutive children," *Scand. J. Gastroenterol.*, vol. 46, no. 9, pp. 1138–1143, 2011.

[25] G. Di Nardo, C. Calabrese, R. Conti Nibali, A. De Matteis, E. Casciani, L. Martemucci, G. Pagliaro, and N. Pagano, "Enteroscopy in children," *United Eur. Gastroenterol. J.*, vol. 6, no. 7, p. 961, 2018.

[26] G. Blanco-Velasco, O. V. Hernández-Mondragón, O. M. Solórzano-Pineda, L. F. García-Contreras, C. Martínez-Camacho, and E. Murcio-Pérez, "Which model of small bowel capsule endoscopy has a better diagnostic yield? A systematic review and meta-analysis," *Acta Gastroenterol. Belg.*, vol. 85, no. 3, pp. 509–517, 2022.

[27] H. sheng Lai, X. ke Wang, J. qun Cai, X. mei Zhao, Z. long Han, J. Zhang, Z. yu Chen, Z. zhao Lin, P. hong Zhou, B. Hu, A. min Li, and S. de Liu, "Standing-type magnetically guided capsule endoscopy versus gastroscopy for gastric examination: multicenter blinded comparative trial," *Dig. Endosc.*, vol. 32, no. 4, p. 557, 2019.

[28] W. Chen, J. Sui, and C. Wang, "Magnetically Actuated Capsule Robots: A Review," *IEEE Access*, vol. 10, pp. 88398–88420, 2022.

[29] G. Kósa, P. Jakab, G. Székely, and N. Hata, "MRI driven magnetic microswimmers," *Biomed. Microdevices*, vol. 14, no. 1, pp. 165–178, 2012.

[30] F. Munoz, G. Alici, H. Zhou, W. Li, and M. Sitti, "Analysis of Magnetic Interaction in Remotely Controlled Magnetic Devices and its Application to a Capsule Robot for Drug Delivery," *IEEE/ASME Trans. Mechatronics*, vol. 23, no. 1, pp. 298–310, 2018.

[31] P. R. Slawinski, K. L. Obstein, and P. Valdastri, "Emerging Issues and Future Developments in Capsule Endoscopy," *Tech. Gastrointest. Endosc.*, vol. 17, no. 1, p. 40, 2015.

[32] R. Sidhu, D. S. Sanders, A. J. Morris, and M. E. McAlindon, "Guidelines on small bowel enteroscopy and capsule endoscopy in adults," *Gut*, vol. 57, no. 1, pp. 125–136, 2008.

[33] B. Guo, E. Ley, J. Tian, J. Zhang, Y. Liu, and S. Prasad, "Experimental and numerical studies of intestinal frictions for propulsive force optimisation of a vibro-impact capsule system," *Nonlinear Dyn.*, vol. 101, no. 1, pp. 65–83, 2020.

[34] F. Li, S. R. Gurudu, G. De Petris, V. K. Sharma, A. D. Shiff, R. I. Heigh, D. E. Fleischer, J. Post, P. Erickson, and J. A. Leighton, "Retention of the capsule endoscope: a single-center experience of 1000 capsule endoscopy procedures," *Gastrointest. Endosc.*, vol. 68, no. 1, pp. 174–180, 2008.

[35] P. Collins, "Video-capsule endoscopy – current and future role," *Med. (United Kingdom)*, vol. 52, no. 5, pp. 317–319, 2024.

[36] N. K. Baek, I. H. Sung, and D. E. Kim, "Frictional resistance characteristics of a capsule inside the intestine for microendoscope design," *Proc. Inst. Mech. Eng. Part H J. Eng. Med.*, vol. 218, no. 3, pp. 193–201, 2004.

[37] X. Wang and M. Q. Meng, "An experimental study of resistant properties of the small intestine for an active capsule endoscope," *Proc. Inst. Mech. Eng. Part H J. Eng. Med.*, vol. 224, no. 1, pp. 107–118, 2010.

[38] J. S. Kim, I. H. Sung, Y. T. Kim, E. Y. Kwon, D. E. Kim, and Y. H. Jang, "Experimental investigation of frictional and viscoelastic properties of intestine for microendoscope application," *Tribol. Lett.*, vol. 22, no. 2, pp. 143–149, 2006.

[39] S. H. Woo, T. W. Kim, Z. Mohy-Ud-Din, I. Y. Park, and J. H. Cho, "Small intestinal model for electrically propelled capsule endoscopy," *Biomed. Eng. Online*, vol. 10, pp. 1–20, 2011.

[40] B. Guo, Y. Liu, and S. Prasad, "Modelling of capsule–intestine contact for a self-propelled capsule robot via experimental and numerical investigation," *Nonlinear Dyn.*, vol. 98, no. 4, pp. 3155–3167, 2019.

[41] Z. Wang, X. Ye, and M. Zhou, "Frictional resistance model of capsule endoscope in the intestine," *Tribol. Lett.*, vol. 51, no. 3, pp. 409–418, 2013.

[42] C. Zhang, H. Liu, and H. Li, "Experimental investigation of intestinal frictional resistance in the starting process of the capsule robot," *Tribol. Int.*, vol. 70, pp. 11–17, 2014.

[43] C. Zhang, H. Liu, and H. Li, "Modeling of frictional resistance of a capsule robot moving in the intestine at a constant velocity," *Tribol. Lett.*, vol. 53, no. 1, pp. 71–78, 2014.

[44] C. Zhang and H. Liu, "Analytical Friction Model of the Capsule Robot in the Small Intestine," *Tribol. Lett.*, vol. 64, no. 3, pp. 1–11, 2016.

[45] L. J. Sliker, G. Ciuti, M. E. Rentschler, and A. Menciassi, "Frictional resistance model for tissue-capsule endoscope sliding contact in the gastrointestinal tract," *Tribol. Int.*, vol. 102, pp. 472–484, 2016.

[46] X. Wang, J. A. Schoen, and M. E. Rentschler, "A quantitative comparison of soft tissue compressive viscoelastic model accuracy," *J. Mech. Behav. Biomed. Mater.*, vol. 20, pp. 126–136, 2013.

[47] Y. Yan, B. Guo, J. Tian, J. Zhang, B. Zhang, E. Ley, Y. Liu, and S. Prasad, "Evaluating the resistant force of an endoscopic capsule self-propelling in the small intestine," *Arch. Appl. Mech.*, vol. 92, no. 12, pp. 3861–3875, 2022.

[48] Y. Yan, B. Zhang, Y. Liu, and S. Prasad, "Dynamics of a vibro-impact self-propelled capsule encountering a circular fold in the small intestine," *Meccanica*, vol. 58, no. 2-3, pp. 451–472, 2023.

[49] C. X. Lin, Q. Y. Yu, J. Wang, W. Ji, W. Li, and Z. R. Zhou, "Friction behavior between endoscopy and esophageal internal surface," *Wear*, vol. 376-377, pp. 272–280, 2017.

[50] H. Park, S. Park, E. Yoon, B. Kim, J. Park, and S. Park, "Paddling based microrobot for capsule endoscopes," *Proc. - IEEE Int. Conf. Robot. Autom.*, no. April, pp. 3377–3382, 2007.

[51] B. Kim, S. Park, and J. O. Park, "Microrobots for a capsule endoscope," *IEEE/ASME Int. Conf. Adv. Intell. Mechatronics, AIM*, pp. 729–734, 2009.

[52] J. Kwon, S. Park, J. Park, and B. Kim, "Evaluation of the critical stroke of an earthworm-like robot for capsule endoscopes," *Proc. Inst. Mech. Eng. Part H J. Eng. Med.*, vol. 221, no. 4, pp. 397–405, 2007.

[53] J. Gao and G. Yan, "Locomotion Analysis of an Inchworm-Like Capsule Robot in the Intestinal Tract," *IEEE Trans. Biomed. Eng.*, vol. 63, no. 2, pp. 300–310, 2016.

[54] J. Gao, G. Yan, Z. Wang, F. Xu, W. Wang, P. Jiang, and D. Liu, "Locomotion enhancement of an inchworm-like capsule robot using long contact devices," *Int. J. Med. Robot. Comput. Assist. Surg.*, vol. 13, no. 2, 2017.

[55] Y. T. Kim and D. E. Kim, "Novel propelling mechanisms based on frictional interaction for endoscope robot," *Tribol. Trans.*, vol. 53, no. 2, pp. 203–211, 2010.

[56] M. N. Huda, P. Liu, C. Saha, and H. Yu, "Modelling and Motion Analysis of a Pill-Sized Hybrid Capsule Robot," *J. Intell. Robot. Syst. 2020 1003*, vol. 100, no. 3, pp. 753–764, 2020.

[57] F. Zhang, D. Ye, and S. Song, "Design of a Legged and Clamper-Based Capsule Robot With Active Locomotion Function," *J. Med. Device.*, vol. 15, no. 1, 2021.

[58] J. Gao, Z. Zhang, and G. Yan, "Locomotion Analysis of a Clamper-Based Capsule Robot in a Compliant Tube," *IEEE/ASME Trans. Mechatronics*, vol. 26, no. 1, pp. 55–65, 2021.

[59] W. Wang, G. Yan, D. Han, Y. Meng, and P. Pu, "Design and testing of a novel gastrointestinal microrobot," *Biomed. Microdevices*, vol. 22, no. 4, pp. 1–11, 2020.

[60] K. Ota, S. Nouda, T. Takeuchi, M. Iguchi, Y. Kojima, T. Kuramoto, T. Inoue, Y. Shindo, K. Uesugi, Y. Fujito, H. Nishihara, N. Ohtsuka, and K. Higuchi, "What Kind of Capsule Endoscope Is Suitable for a Controllable Self-Propelling Capsule Endoscope? Experimental Study Using a Porcine Stomach Model for Clinical Application (with Videos)," *PLoS One*, vol. 10, no. 10, 2015.

[61] G. La Spina, C. Stefanini, A. Menciassi, and P. Dario, "A novel technological process for fabricating micro-tips for biomimetic adhesion," *J. Micromechanics Microengineering*, vol. 15, no. 8, pp. 1576–1587, 2005.

[62] P. Glass, E. Cheung, and M. Sitti, "A legged anchoring mechanism for capsule endoscopes using micropatterned adhesives," *IEEE Trans. Biomed. Eng.*, vol. 55, no. 12, pp. 2759–2767, 2008.

[63] E. Buselli, V. Pensabene, P. Castrataro, P. Valdastri, A. Menciassi, and P. Dario, "Evaluation of friction enhancement through soft polymer micropatterns in active capsule endoscopy," *Meas. Sci. Technol.*, vol. 21, no. 10, 2010.

[64] Y. T. Kim and D. E. Kim, "Biotribological investigation of a multi-tube foot for traction generation in a medical microrobot," *Proc. Inst. Mech. Eng. Part H J. Eng. Med.*, vol. 223, no. 6, pp. 677–686, 2009.

[65] J. Min, Y. Yang, Z. Wu, and W. Gao, "Robotics in the Gut," *Adv. Ther.*, vol. 3, no. 4, 2020.

[66] A. Koulaouzidis, D. K. Iakovidis, A. Karargyris, and E. Rondonotti, "Wireless endoscopy in 2020: Will it still be a capsule?," *World J. Gastroenterol.*, vol. 21, no. 17, pp. 5119–5130, 2015.

[67] A. M. Singeap, C. Stanciu, and A. Trifan, "Capsule endoscopy: The road ahead," *World J. Gastroenterol.*, vol. 22, no. 1, pp. 369–378, 2016.

[68] S. E. Mills, *Histology for Pathologists*. Lippincott Williams Wilkins, 5th ed., 2019.

[69] K. T. von Trotha, N. Butz, J. Grommes, M. Binnebösel, N. Charalambakis, G. Mühlenbruch, V. Schumpelick, U. Klinge, U. P. Neumann, A. Prescher, and C. J. Krones, "Vascular anatomy of the small intestine—a comparative anatomic study on humans and pigs," *Int. J. Colorectal Dis.*, vol. 30, no. 5, pp. 683–690, 2015.

[70] H. Sung, "Degradation potential of biological tissues fixed with various fixatives: An in vitro study," *J. Biomed. Mater. Res.*, vol. 35, no. 2, pp. 147–155, 1997.

[71] A. Vass, "Beyond the grave – understanding human decomposition," *Microbiol. Today*, vol. 28, no. 28, pp. 190–192, 2001.

[72] T. Yao, J. Cao, X. Fan, and D. Zhu, *Physiology*, vol. 1. Beijing: People's Medical Publishing House, 1 ed., 2005.

[73] F. H. Martini and E. F. Bartholomew, *Fundamentals of Anatomy and Physiology*. Benjamin-Cummings Pub Co, 7th ed., 2005.

[74] C. G. Cronin, E. Delappe, D. G. Lohan, C. Roche, and J. M. Murphy, "Normal small bowel wall characteristics on MR enterography," *Eur. J. Radiol.*, vol. 75, no. 2, pp. 207–211, 2010.

[75] A. S. Kinany, *Introduction to human physiology*. Dar Wael Publishing and Distribution, 2016.

[76] M. E. Johansson, H. Sjövall, and G. C. Hansson, "The gastrointestinal mucus system in health and disease," *Nat. Rev. Gastroenterol. Hepatol.*, vol. 10, no. 6, pp. 352–361, 2013.

[77] V Fiorenza, YS Yee, and AM Zfass., "Small intestinal motility: normal and abnormal function," *Am J Gastroenterol*, vol. 82, no. 11, pp. 1111–1114, 1987.

[78] Y. Yang and K. Ge, *Encyclopedia of nutriyion science*. People's Medical Publishing House, 2 ed., 2024.

[79] J. WorsØe, L. Fynne, T. Gregersen, V. Schlageter, L. A. Christensen, J. F. Dahlerup, N. J. Rijkhoff, S. Laurberg, and K. Krogh, "Gastric transit and small intestinal transit time and motility assessed by a magnet tracking system," *BMC Gastroenterol.*, vol. 11, 2011.

[80] H. Elsa, *Impact of chronic renal failure and uremia on intestinal motility and permeability*. PhD thesis, Université de Lyon, 2017.

[81] M. A. Hayat, "Pancreatic Carcinoma: An Introduction," *Handb. Immunohistochem. Situ Hybrid. Hum. Carcinomas*, vol. 3, pp. 279–304, 2005.

[82] R. Bansil and B. S. Turner, "Mucin structure, aggregation, physiological functions and biomedical applications," *Curr. Opin. Colloid Interface Sci.*, vol. 11, no. 2-3, pp. 164–170, 2006.

[83] M. E. Johansson, D. Ambort, T. Pelaseyed, A. Schütte, J. K. Gustafsson, A. Ermund, D. B. Subramani, J. M. Holmén-Larsson, K. A. Thomsson, J. H. Bergström, S. Van Der Post, A. M. Rodriguez-Piñeiro, H. Sjövall, M. Bäckström, and G. C. Hansson, "Composition and functional role of the mucus layers in the intestine," *Cell. Mol. Life Sci.*, vol. 68, no. 22, pp. 3635–3641, 2011.

[84] S. K. Lai, Y. Y. Wang, D. Wirtz, and J. Hanes, "Micro- and macrorheology of mucus," *Adv. Drug Deliv. Rev.*, vol. 61, no. 2, pp. 86–100, 2009.

[85] C. Atuma, V. Strugala, A. Allen, and L. Holm, "The adherent gastrointestinal mucus gel layer: Thickness and physical state in vivo," *Am. J. Physiol. - Gastrointest. Liver Physiol.*, vol. 280, no. 5, pp. 922–929, 2001.

[86] A. M. C. Roskott, V. B. Nieuwenhuijs, G. Dijkstra, L. G. Koudstaal, H. G. Leuvenink, and R. J. Ploeg, "Small bowel preservation for intestinal transplantation: A review," *Transpl. Int.*, vol. 24, no. 2, pp. 107–131, 2011.

[87] Y. Chen, J. Shi, T. C. Xia, R. Xu, X. He, and Y. Xia, "Preservation Solutions for Kidney Transplantation: History, Advances and Mechanisms," *Cell Transplant.*, vol. 28, no. 12, pp. 1472–1489, 2019.

[88] A. Petrenko, M. Carnevale, A. Somov, J. Osorio, J. Rodríguez, E. Guibert, B. Fuller, and F. Froghi, "Organ Preservation into the 2020s: The Era of Dynamic Intervention," *Transfus. Med. Hemotherapy*, vol. 46, no. 3, pp. 151–172, 2019.

[89] G. Singh and A. Chanda, "Mechanical properties of whole-body soft human tissues: A review," *Biomed. Mater.*, vol. 16, no. 6, 2021.

[90] G. A. Holzapfel, "Biomechanics of Soft Tissue," in *Handb. Mater. Behav. Model.*, Austria: Graz University of Technology, 2000.

[91] R. J. Minns, P. D. Soden, and D. S. Jackson, "The role of the fibrous components and ground substance in the mechanical properties of biological tissues: A preliminary investigation," *J. Biomech.*, vol. 6, no. 2, pp. 153–165, 1973.

[92] A. B. Lyle, J. T. Luftig, and M. E. Rentschler, "A tribological investigation of the small bowel lumen surface," *Tribol. Int.*, vol. 62, pp. 171–176, 2013.

[93] Allison B. Lyle, *Evaluation of small bowel lumen friction forces for applications in in vivo robotic capsule endoscopy.* PhD thesis, University of Colorado at Boulder, 2012.

[94] V. I. Egorov, I. V. Schastlivtsev, E. V. Prut, A. O. Baranov, and R. A. Turusov, "Mechanical properties of the human gastrointestinal tract," *J. Biomech.*, vol. 35, no. 10, pp. 1417–1425, 2002.

[95] M. Scholze, S. Safavi, K. C. Li, B. Ondruschka, M. Werner, J. Zwirner, and N. Hammer, "Standardized tensile testing of soft tissue using a 3D printed clamping system," *HardwareX*, vol. 8, 2020.

[96] B. Innocenti, J.-C. Larrieu, P. Lambert, and S. Pianigiani, "Automatic characterization of soft tissues material properties during mechanical tests," *Muscles Ligaments Tendons J.*, vol. 7, no. 4, pp. 529–537, 2017.

[97] B. Johnson, S. Campbell, and N. Campbell-Kyureghyan, "Biomechanical properties of abdominal organs under tension with special reference to increasing strain rate," *J. Biomech.*, vol. 109, 2020.

[98] M. Griffin, Y. Premakumar, A. Seifalian, P. E. Butler, and M. Szarko, "Biomechanical characterization of human soft tissues using indentation and tensile testing," *J. Vis. Exp.*, vol. 2016, no. 118, 2016.

[99] Z. Ehteshami, *Characterising the Mechanical Properties of Large Intestine*. PhD thesis, University of Leeds, 2015.

[100] S. Mohammadi, S. Aflaki, and P. Hajikarimi, "Two dimensional creep analysis of a linear cracked viscoelastic medium using the extended finite element method," in *Eur. Congr. Comput. Methods Appl. Sci. Eng.*, (Austria), 2012.

[101] Y. Huang, L. Liang, R. Hu, P. Tang, Z. Guo, Y. Liu, and G. Hu, "Frictional resistance model for a capsule and an intestine with different central axes based on the intestinal nonlinear constitutive relationship," *Tribol. Int.*, vol. 173, p. 107603, 2022.

[102] J. Park, A. Shin, S. Jafari, and J. L. Demer, "Material properties and effect of preconditioning of human sclera, optic nerve, and optic nerve sheath," *Biomech. Model. Mechanobiol.*, vol. 20, no. 4, pp. 1353–1363, 2021.

[103] M. Ebrahimi, A. Mohammadi, A. Ristaniemi, L. Stenroth, and R. K. Korhonen, "The effect of different preconditioning protocols on repeatability of bovine ACL stress-relaxation response in tension," *J. Mech. Behav. Biomed. Mater.*, vol. 90, pp. 493–501, 2019.

[104] Z. Liu, K. Yeung, and Z. Liu, "The Preconditioning and Stress Relaxation of Skin Tissue," *J. Biomed. Pharm. Eng.*, vol. 2, pp. 22–28, 2008.

[105] S. Cheng, E. C. Clarke, and L. E. Bilston, "The effects of preconditioning strain on measured tissue properties," *J. Biomech.*, vol. 42, no. 9, pp. 1360–1362, 2009.

[106] G. Bianco, A. M. Levy, R. Grytz, and M. A. Fazio, "Effect of different preconditioning protocols on the viscoelastic inflation response of the posterior sclera[1] G. Bianco, A. M. Levy, R. Grytz, and M. A. Fazio, "Effect of different preconditioning protocols on the viscoelastic inflation response of the ," *Acta Biomater.*, vol. 128, pp. 332–345, 2021.

[107] K. G. Byrnes, D. Walsh, L. G. Walsh, D. M. Coffey, M. F. Ullah, R. Mirapeix, J. Hikspoors, W. Lamers, Y. Wu, X. Q. Zhang, S. X. Zhang, P. Brama, C. P. Dunne, I. S. O'Brien, C. B. Peirce, M. J. Shelly, T. G. Scanlon, M. E. Luther, H. D. Brady, P. Dockery, K. W. McDermott, and J. C. Coffey, "The development and structure of the mesentery," *Commun. Biol. 2021 41*, vol. 4, no. 1, pp. 1–10, 2021.

[108] E. O. Carew, A. Garg, J. E. Barber, and I. Vesely, "Stress relaxation preconditioning of porcine aortic valves," *Ann. Biomed. Eng.*, vol. 32, no. 4, pp. 563–572, 2004.

[109] D. Remache, M. Caliez, M. Gratton, and S. Dos Santos, "The effects of cyclic tensile and stress-relaxation tests on porcine skin," *J. Mech. Behav. Biomed. Mater.*, vol. 77, pp. 242–249, 2018.

[110] D. Huang, L. Foster, M. Stone, D. Kulber, and M. F. Metzger, "Biomechanical Properties of Knee Medial Collateral Ligament Compared to Palmaris Longus for Ulnar Collateral Ligament Reconstruction," *Ann. Biomed. Eng.*, vol. 51, no. 8, pp. 1795–1801, 2023.

[111] S. Sattari, C. A. Mariano, and M. Eskandari, "Biaxial mechanical properties of the bronchial tree: Characterization of elasticity, extensibility, and energetics, including the effect of strain rate and preconditioning," *Acta Biomater.*, vol. 155, pp. 410–422, 2023.

[112] A. K. Ameer, M. O. Mousa, W. Y. Ali, A. M. Samy, and A. H. El-Abd, "Influence of Counterface Materials on the Tribological Behavior of Dental Polymethyl Methacrylate Reinforced by Single-Walled Carbon Nanotubes (SWCNT)," *SVU-International J. Eng. Sci. Appl.*, vol. 3, no. 2, pp. 68–79, 2022.

[113] L. Barducci, J. C. Norton, S. Sarker, S. Mohammed, R. Jones, P. Valdastri, and B. S. Terry, "Fundamentals of the gut for capsule engineers," *Prog. Biomed. Eng.*, vol. 2, no. 4, 2020.

[114] P. Fleckenstein, "Migrating electrical spike activity in the fasting human small intestine," *Am. J. Dig. Dis.*, vol. 23, no. 9, pp. 769–775, 1978.

[115] H. Vu, T. Echigo, R. Sagawa, K. Yagi, M. Shiba, K. Higuchi, T. Arakawa, and Y. Yagi, "Detection of contractions in adaptive transit time of the small bowel from wireless capsule endoscopy videos," *Comput. Biol. Med.*, vol. 39, no. 1, pp. 16–26, 2009.

[116] S. L. Woo, M. A. Gomez, and W. H. Akeson, "The Time and History-Dependent Viscoelastic Properties of the Canine Medial Collateral Ligament," *J. Biomech. Eng.*, vol. 103, no. 4, pp. 293–298, 1981.

[117] S. Meghezi, F. Couet, P. Chevallier, and D. Mantovani, "Effects of a pseudo-physiological environment on the elastic and viscoelastic properties of collagen gels," *Int. J. Biomater.*, 2012.

[118] J. M. Mattice, A. G. Lau, M. L. Oyen, and R. W. Kent, "Spherical indentation load-relaxation of soft biological tissues," *J. Mater. Res.*, vol. 21, no. 8, pp. 2003–2010, 2006.

[119] M. L. Oyen, T. A. Shean, D. G. Strange, and M. Galli, "Size effects in indentation of hydrated biological tissues," *J. Mater. Res.*, vol. 27, no. 1, pp. 245–255, 2012.

[120] A. Chegenizadeh, M. Keramatikerman, and H. Nikraz, "Effect of loading strain rate on creep and stress-relaxation characteristics of sandy silt," *Results Eng.*, vol. 7, 2020.

[121] K. K. Dwivedi, P. Lakhani, S. Kumar, and N. Kumar, "The Effect of Strain Rate on the Stress Relaxation of the Pig Dermis: A Hyper-Viscoelastic Approach," *J. Biomech. Eng.*, vol. 142, no. 9, 2020.

[122] S. Meghezi, F. Couet, P. Chevallier, and D. Mantovani, "Effects of a pseudo-physiological environment on the elastic and viscoelastic properties of collagen gels," *Int. J. Biomater.*, 2012.

[123] J. Lin, Y. Shi, Y. Men, X. Wang, J. Ye, and C. Zhang, "Mechanical roles in formation of oriented collagen fibers," *Tissue Eng. - Part B Rev.*, vol. 26, no. 2, pp. 116–128, 2020.

[124] B. A. Roeder, K. Kokini, J. E. Sturgis, J. P. Robinson, and S. L. Voytik-Harbin, "Tensile mechanical properties of three-dimensional type I collagen extracellular matrices with varied microstructure," *J. Biomech. Eng.*, vol. 124, no. 2, pp. 214–222, 2002.

[125] M. D. Sinnott, P. W. Cleary, and S. M. Harrison, "Peristaltic transport of a particulate suspension in the small intestine," *Appl. Math. Model.*, vol. 44, pp. 143–159, 2017.

[126] M. A. Atalla, J. Nieuwenhuis, A. Martin, X. Wang, A. Canden, M. Carre, R. Lewis, M. Wiertlewski, and A. Sakes, "Ultrasonically-lubricated catheters:

Miniaturization and ex-vivo tissue validation," in *Proceedings of the 16th Hamlyn Symposium on Medical Robotics 2024*, pp. 19–20, The Hamlyn Centre Imperial College London, 2024.

[127] J. Chen, X. Liu, Y. Hu, X. Chen, and S. Tan, "Cryopreservation of tissues and organs: present, bottlenecks, and future," *Front. Vet. Sci.*, vol. 10, 2023.

[128] D. F. Evans, G. Pye, R. Bramley, A. G. Clark, T. J. Dyson, and J. D. Hardcastle, "Measurement of gastrointestinal pH profiles in normal ambulant human subjects," *Gut*, vol. 29, no. 8, pp. 1035–1041, 1988.

[129] H. Kang, "Sample size determination and power analysis using the G*Power software," *J. Educ. Eval. Health Prof.*, vol. 18, 2021.

[130] J. M. Coles, D. P. Chang, and S. Zauscher, "Molecular mechanisms of aqueous boundary lubrication by mucinous glycoproteins," *Curr. Opin. Colloid Interface Sci.*, vol. 15, no. 6, pp. 406–416, 2010.

[131] S. Jahn and J. Klein, "Hydration Lubrication: The Macromolecular Domain," *Macromolecules*, vol. 48, no. 15, pp. 5059–5075, 2015.

[132] H. L. Bui, Y. H. Su, C. J. Yang, C. J. Huang, and J. Y. Lai, "Mucoadhesive, antioxidant, and lubricant catechol-functionalized poly(phosphobetaine) as biomaterial nanotherapeutics for treating ocular dryness," *J. Nanobiotechnology*, vol. 22, no. 1, 2024.

[133] W. Lin and J. Klein, "Hydration Lubrication in Biomedical Applications: From Cartilage to Hydrogels," *Accounts Mater. Res.*, vol. 3, no. 2, pp. 213–223, 2022.

[134] R. A. Cone, "Barrier properties of mucus," *Adv. Drug Deliv. Rev.*, vol. 61, no. 2, pp. 75–85, 2009.

[135] M. Kwiatkowska, S. E. Franklin, C. P. Hendriks, and K. Kwiatkowski, "Friction and deformation behaviour of human skin," *Wear*, vol. 267, no. 5-8, pp. 1264–1273, 2009.

[136] S. Derler and G. M. Rotaru, "Stick–slip phenomena in the friction of human skin," *Wear*, vol. 301, no. 1-2, pp. 324–329, 2013.

[137] M. J. Adams, B. J. Briscoe, and S. A. Johnson, "Friction and lubrication of human skin," *Tribol. Lett.*, vol. 26, no. 3, pp. 239–253, 2007.

[138] J. S. Kim, I. H. Sung, Y. T. Kim, D. E. Kim, and Y. H. Jang, "Analytical model development for the prediction of the frictional resistance of a capsule endoscope inside an intestine," *Proc. Inst. Mech. Eng. Part H J. Eng. Med.*, vol. 221, no. 8, pp. 837–845, 2007.